Lasertreatment of Al-Cu materials

Laserbearbeitung von Al-Cu-Werkstoffen

Master's thesis of
Simon Kümmel

Examiner: Prof. Dr. Johannes Roth
Co-Examiner: Prof. Dr. Christian Holm

Institute for Functional Matter and Quantum Technologies
University of Stuttgart
Germany
July 19, 2023

Contents

Acronyms

bcc Basis-centered cubic

CG Conjugate Gradient

DFPT Density Functional Perturbation Theory

DFT Density Functional Theory

DOS Density of States

fcc Face-centered cubic

GGA Generalised Gradient Approximation

GP Guinier-Preston

HLRS Hochleistungsrechenzentrum Stuttgart

LDA Local Density Approximation

MD Molecular Dynamics

PBC Periodic boundary condition

PBE Perdew-Burke-Ernzerhof

sc Simple cubic

TTM Two-Temperature Model

VASP Vienna Ab initio Simulation Package

Chapter 1

Introduction

New manufacturing techniques like additive manufacturing and in particular 3D laser printing are the latest trends that might make manufacturing components with low-production numbers a lot cheaper than conventional subtractive manufacturing like cutting, drilling or grinding. At the same time, they allow for far more complex structures to be crafted, such as bent ducts in a solid part that could not be achieved with a conventional drill.
All this seems very profitable for the aerospace industry where alloys based on aluminium are very common. In particular, aluminium alloys with a small copper percentage have been used in aeroplanes for about a century now, one of the most well-known being *Duralumin*. Using alloys instead of pure metals allows for fine-tuning properties like hardness, thermal conductivity or corrosion resistance. But not only is the production of parts made from these alloys with 3D laser printing a promising method, the laser treatment of alloys might be able to delay fatiquing of components which could greatly increase the lifetime of the parts.
In order to improve these techniques, we have to expand our knowledge about how metals and alloys behave under laser irradiation. Computer simulations allow such insights into the properties and material dynamics of all kinds of materials whereas analytical calculations can only be done on simple and idealised systems. While there are many approaches to modelling materials, such as density functional theory, molecular dynamics or fluid simulations, we choose the first one because it allows us to gain insight into quantum mechanical processes. Also, some results can be used for molecular dynamics simulations that reach time and length scales that are close to real-world experiments. In the past, there have been few similar investigations, however they were mostly focussed on semiconductors and silicon in particular. In this work, we therefore want to extend our understanding of laser excited materials to metals and alloys and compare them to the semiconductor silicon.

We start by going over the theoretical fundamentals of the calculations performed using density functional theory and how it can be extended for practically all materials. We also discuss properties that can be used to describe solids even at different degrees of excitation. Next, we explain how the calculations were performed and how computation time can be used most effectively and efficiently.

We then first search for appropriate parameters for the calculations that are capable of producing reliable data. Then, we validate our methods by calculating ground state properties of aluminium, copper and their alloys and compare them to other theoretical and experimental investigations done by other groups. Afterwards, we finally calculate electron temperature-dependent properties of solids to get more insights into how metals and alloys behave under laser irradiation.

Chapter 2

Theoretical background

This work focusses on the examination of metals and alloys under laser irradiation using density functional theory. We therefore start by giving an overview of the processes in matter under laser irradiation and how we can model them. Then, we explain the basic concepts of density functional theory, discuss how we can couple these calculations to molecular dynamics simulations and how we can incorporate laser excitation.
Since we want to investigate properties of solids under laser irradiation, we describe the properties of solids that can and will be used to characterise materials under laser irradiation, i.e. the elastic constants, phonon spectra and the density of states.

2.1 Laser processes

During laser irradiation of a solid, the electrons are excited to an excited state almost immediately while the atoms remain in their initial positions. Electron-phonon coupling then causes energy to be transferred from the electrons to the atoms. In this context, it makes sense to introduce separate temperatures for the atoms T_l and the electrons T_c. Models that incorporate these two temperatures belong to the class of Two-Temperature Models (TTMs). If the material is not excited or long after the laser irradiation, the two temperatures are identical. The time evolution of both temperatures before, during and after laser irradiation is summarised in figure 2.1. Theoretic models have been developed to treat electron-phonon coupling and the TTM. In this work, however, we focus on static properties of materials obtained using density functional theory. This method still gives a lot of insights in the behaviour of laser-excited materials while not having to work with an overly complicated model. Using Density Functional Theory (DFT), it is also possible to treat the excitations in a statistical way by occupying the states only partially. While this approach seems primitive compared to purely analytical methods, it has proven to yield results that capture an extend of properties that most analytical methods can't, especially in large and dynamic systems [1, 2]. The details on how DFT calculations can mimic excitations are presented later.

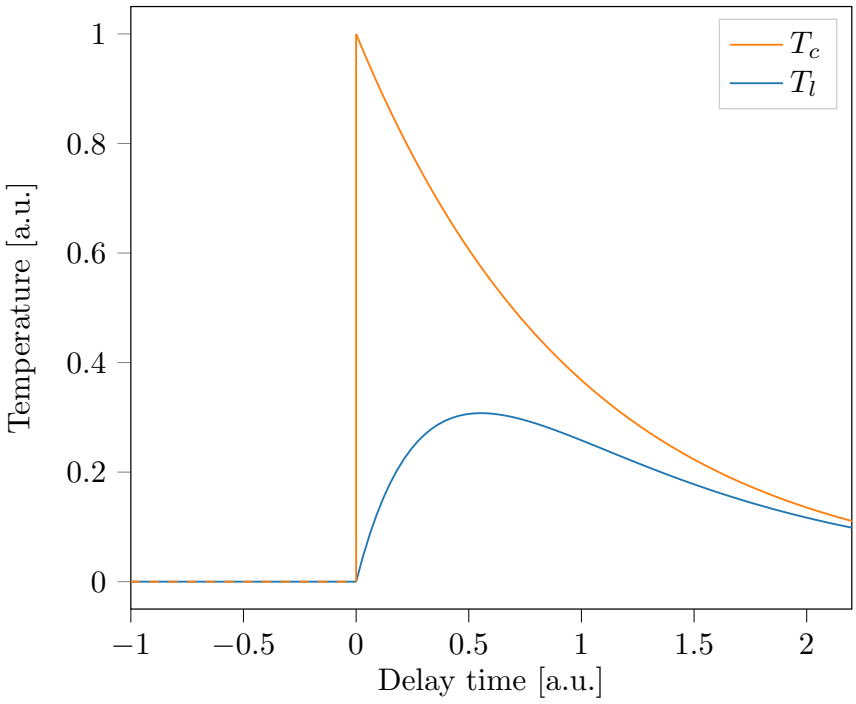

Figure 2.1: Time evolution of the lattice temperature T_l and the electron temperature T_c after laser irradiation of a solid.

2.2 DFT

2.2.1 Introduction to Density Functional Theory

Solving Schrödinger's equation is the key to insights into the quantum mechanical nature of any material. It is a difficult task to solve this equation which is why different computer-based methods have been introduced, also since analytical approaches are very limited. Hohenberg and Kohn realised that we can solve Schrödinger's equation exactly even if we don't use the single-particle wave functions directly but instead the electron density [3]

$$n(\vec{r}) = \sum_{i=1}^{N} |\Psi_i(\vec{r})|^2 \tag{2.1}$$

which consists of the single-particle wave functions Ψ_i of particle i. This expression leads to the total energy functional in appropriate units ($m_e = 1$, $\hbar = 1$)

$$\begin{aligned} E[n(\vec{r})] &= T[n(\vec{r})] + U[n(\vec{r})] + V[n(\vec{r})] \\ &= \frac{1}{2}\int \mathrm{d}\vec{r}\,\vec{\nabla}\Psi^*(\vec{r})\vec{\nabla}\Psi(\vec{r}) + \frac{1}{2}\int \mathrm{d}\vec{r}\,\mathrm{d}\vec{r}\prime\, \frac{n(\vec{r})n(\vec{r}\prime)}{|\vec{r}-\vec{r}\prime|} + \int \mathrm{d}\vec{r}\, v(\vec{r})n(\vec{r}), \end{aligned} \tag{2.2}$$

where $T[n(\vec{r})]$ is the kinetic energy functional, $U[n(\vec{r})]$ is the Coulomb interaction of the electrons and $V[n(\vec{r})]$ is the energy functional due to an external potential $v(\vec{r})$, i.e. the

specific system.
The reason why this approach can solve the Schrödinger equation is summarised in the first Hohenberg-Kohn theorem which states that the external field contribution is a unique functional of the electron density [3]. A detailed proof of this theorem is given in appendix A. The second Hohenberg-Kohn theorem states that the ground state energy can be found for the exact electron density which is trivial using the Rayleigh-Ritz principle [4].
We can go one step further and split the total energy functional (2.2) into different parts.

$$F[n(\vec{r})] = T[n(\vec{r})] + U[n(\vec{r})] \tag{2.3}$$

is then the universal functional that contains no contribution from the system that enters through the external potential $v(\vec{r})$. In (2.3), the Coulomb contribution, which can be calculated, can then be split from the rest, resulting in

$$F[n(\vec{r})] = \frac{1}{2}\int \mathrm{d}\vec{r}\,\mathrm{d}\vec{r\prime}\,\frac{n(\vec{r})n(\vec{r\prime})}{|\vec{r}-\vec{r\prime}|} + G[n(\vec{r})]. \tag{2.4}$$

$G[n(\vec{r})]$ then contains the kinetic contributions, as well as exchange and correlation effects that no other part in (2.2) takes into account. These exchange and correlation effects are summarised in the exchange-correlation functional E^{XC} that will be discussed in more detail later.
By varying the electron density, we arrive at the Kohn-Sham equations [5]

$$\left[-\frac{1}{2}\vec{\nabla}^2 + \int \mathrm{d}\vec{r\prime}\,\frac{n(\vec{r\prime})}{|\vec{r}-\vec{r\prime}|} + v(\vec{r}) + \frac{\delta E^{\mathrm{XC}}}{\delta n(\vec{r})}\right]\tilde{\Psi}_i(\vec{r}) = \epsilon_i\tilde{\Psi}_i(\vec{r}) \tag{2.5}$$

with the Lagrange multiplier ϵ_i and an approximate electron density

$$n(\vec{r}) = \sum_{i=1}^{N}\left|\tilde{\Psi}_i(\vec{r})\right|^2 \tag{2.6}$$

computed from the Kohn-Sham orbitals $\tilde{\Psi}_i(\vec{r})$ which have no physical meaning. Starting with some $n(\vec{r})$, the Schrödinger equation (2.5) is constructed and solved to find the Ψ_i from which then a new density can be calculated. This process is repeated until a convergence criterion is reached, i.e. self-consistency is achieved.

This formalism is equivalent to Schrödinger's equation and it is important to note that until here, no approximations have been made. However, the exchange-correlation functional E^{XC} is not known in general. Hohenberg and Kohn were able to reproduce the Thomas-Fermi equation for an electron gas with slowly varying density. They also suggested a gradient expansion of $G[n(\vec{r})]$ for a more general description. Both approaches to approximate E^{XC} are described in the next section.

It should be mentioned that the DFT code Vienna Ab initio Simulation Package (VASP) that will be used in this work is only considering the valence electrons, as opposed to all-electron codes like Wien2K [6]. This method is called the frozen-core approximation [7] and is justified for the excitations here since the non-valence electrons are much more tightly bond, as can be seen in the ionization energies.
We should also note that the concept of DFT can be extended in many ways. Since DFT is based on Schrödinger's equation which is non-relativistic, we don't include spin-orbit coupling in this theory. However, DFT can be extended to also include relativistic effects. Also, perturbations to a system can be taken into account within Density Functional Perturbation Theory (DFPT). Since DFPT is only used for the calculation of the phonon spectra in this work, we don't go into detail here. A great overview of the topic can be found in [8]. We also derive the first-order correction within DFPT in appendix C.

2.2.2 Approximations for exchange-correlation

Local Density Approximation
The Local Density Approximation (LDA) assumes that the exchange-correlation functional only depends on the local electron density according to

$$E_{\mathrm{LDA}}^{\mathrm{XC}} = \int \mathrm{d}\vec{r}\, n(\vec{r}) \epsilon^{\mathrm{XC}}[n(\vec{r})]. \tag{2.7}$$

It is local in space and doesn't take correlation effects into account. For a homogeneous electron gas, an exact expression can be derived.
Since electrons in metals mostly behave like a homogeneous electron gas, this approximation is observed to reproduce properties of metals well.

Generalised Gradient Approximation
To allow the exchange-correlation functional to represent more of a non-local behaviour, the Generalised Gradient Approximation (GGA) also includes the dependency on the gradient of the local electron density

$$E_{\mathrm{LDA}}^{\mathrm{XC}} = \int \mathrm{d}\vec{r}\, n(\vec{r}) \epsilon^{\mathrm{XC}}\Big[n(\vec{r}), \vec{\nabla} n(\vec{r})\Big]. \tag{2.8}$$

similar to a Taylor expansion of a function. This technically doesn't make the functional non-local but rather semi-local. To improve the accuracy of E^{XC}, higher orders can be included - at the cost of efficiency. Since it's only semi-local, GGAs cannot take long-range interaction into account, such as van der Waals forces. Such interaction usually require different approaches. A great overview can be found in [9].
One of the most commonly used formulations of GGAs is the Perdew-Burke-Ernzerhof (PBE) functional [10]. It has proven to be reliable and very accurate in most situations while still being computationally cheap considering the increase in accuracy and flexibility compared to LDA. Since van der Waals interactions play a minor role in metals and alloys, we can safely use PBE in this work.

2.2.3 DFT methods with molecular dynamics

DFT calculations as we introduced them require that we provide a structure to calculate and optimise the wave functions to minimise the energy. In some cases, we also want to include dynamics in our systems. This might be of interest if the exact structure is not known prior and we want to find the ground state structure or if one wants to study phase transitions on a quantum mechanical level. In these and other cases, DFT calculations have to be coupled to Molecular Dynamics (MD) calculations.
In order to couple a DFT calculation to an MD simulation, one has to calculate the forces from the electronic configuration of the DFT calculation in order to update the atomic positions. Starting from the energy in Dirac notation

$$E_\lambda = \langle \Psi_\lambda | \, H_\lambda \, | \Psi_\lambda \rangle \,, \tag{2.9}$$

we find its derivative with respect to some parameter λ

$$\begin{aligned}
\frac{\partial E_\lambda}{\partial \lambda} =& \left\langle \frac{\partial \Psi_\lambda}{\partial \lambda} \middle| H_\lambda \middle| \Psi_\lambda \right\rangle + \left\langle \Psi_\lambda \middle| \frac{\partial H_\lambda}{\partial \lambda} \middle| \Psi_\lambda \right\rangle + \left\langle \Psi_\lambda \middle| H_\lambda \middle| \frac{\partial \Psi_\lambda}{\partial \lambda} \right\rangle \\
=& E_\lambda \left(\left\langle \frac{\partial \Psi_\lambda}{\partial \lambda} \middle| \Psi_\lambda \right\rangle + \left\langle \Psi_\lambda \middle| \frac{\partial \Psi_\lambda}{\partial \lambda} \right\rangle \right) + \left\langle \Psi_\lambda \middle| \frac{\partial H_\lambda}{\partial \lambda} \middle| \Psi_\lambda \right\rangle \\
=& E_\lambda \frac{\partial}{\partial \lambda} \langle \Psi_\lambda | \Psi_\lambda \rangle + \left\langle \Psi_\lambda \middle| \frac{\partial H_\lambda}{\partial \lambda} \middle| \Psi_\lambda \right\rangle \\
=& E_\lambda \frac{\partial (1)}{\partial \lambda} + \left\langle \Psi_\lambda \middle| \frac{\partial H_\lambda}{\partial \lambda} \middle| \Psi_\lambda \right\rangle = \left\langle \Psi_\lambda \middle| \frac{\partial H_\lambda}{\partial \lambda} \middle| \Psi_\lambda \right\rangle .
\end{aligned} \tag{2.10}$$

Now replacing the derivative with respect to λ with a spatial derivative, we end up with the so-called Hellmann-Feynman force [11, 12, 13].
Having found the forces, we can integrate the equations of motion of atom i

$$\vec{F_i} = m_i \ddot{\vec{r}_i} \tag{2.11}$$

using the usual techniques that we will not go into more detail because we use a slightly different approach to optimising structures. We use the so-called Conjugate Gradient (CG) algorithm [14, 15] which uses the local gradient of the energy surface to move the atoms. Usually, this method of optimising a structure is a lot faster compared to MD-DFT calculations since we are not bound to a fixed time step.
It is important to note that we we assuming that Ψ_λ in Equation 2.10 is the eigenfunction of the Hamiltonian H_λ from an infinite basis set. In reality, only finite basis sets can be used for DFT calculations. One then has to choose between having an error in the energies, known as Pulay stress [16], having to correct for the finite set by calculating the derivatives of the wave functions - which is computationally very costly - or increasing the basis set until the error is neglectibly small.

2.2.4 Finite-temperature DFT calculations

Pure DFT calculations are used for ground state calculations. However, only one year after its introduction, the concept was extended to finite-temperature calculations [17] by smearing out the occupancies of the states. This is useful since it allows us to calculate properties of excited materials in which the same happens. While it's technically an equilibrium distribution, the Fermi-Dirac distribution

$$f(E, T_c) = \frac{1}{\exp((E - \mu)/(\mathrm{k_B} T_c)) + 1} \tag{2.12}$$

is most commonly used to smear out the states due to its physical significance. In figure 2.2, it is shown for three different temperatures, i.e. smearings. The entropic contribution of the electron gas changes the total energy functional that is used in DFT calculations. A quick description of how the total energy functional is changed is given in appendix D.

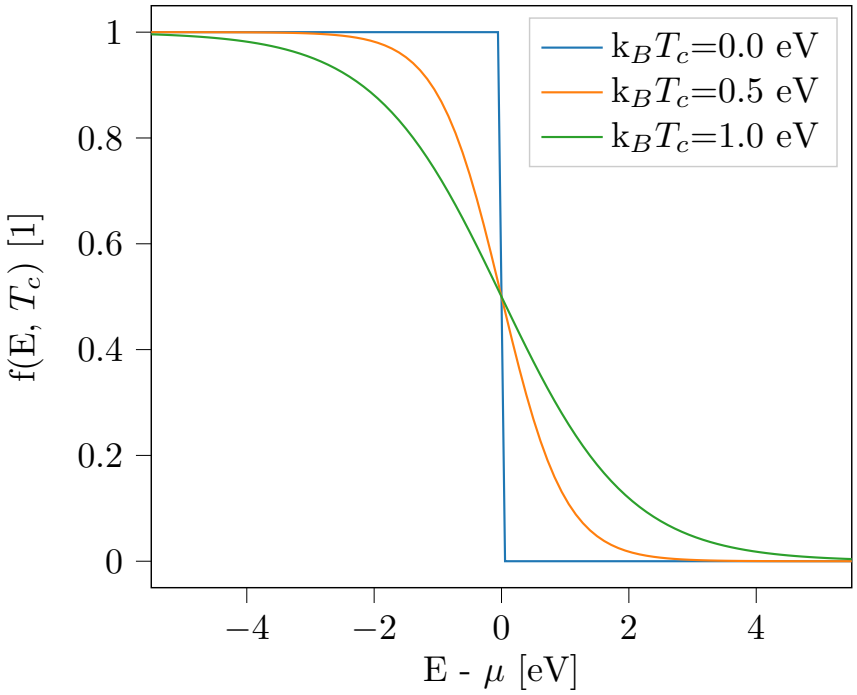

Figure 2.2: Fermi-Dirac distribution at three different temperatures.

2.3 Properties of solids

This chapter is devoted to properties that can be used to describe solids. The first set of properties are the elastic constants which give a general idea of the behaviour under deformations along different axes. Next, we describe phonon spectra which represent the lattice vibrations. Lastly, we describe the electron Density of States (DOS) which can be used as a tool for the theoretical description of thermodynamic properties of solids such as the internal or free energy, heat capacity and pressure.

2.3.1 Elastic constants

In this section, we quickly go over the basics of elastic constants and their meaning. Most information is taken from [18].
As long as Hooke's law holds, we assume that that the stress σ is proportional to the strain $\epsilon = \Delta L/L$ with L being the undeformed length or volume and ΔL being the quantity of the elastic transformation and thus with the elastic constant C

$$\sigma = C\epsilon = \frac{F}{A}. \tag{2.13}$$

The latter expression is an alternative definition of stress, i.e. the force F that acts on an area A. Until now, we didn't specify in which direction a material is deformed. We can extend the definition of stress to the stress tensor

$$\sigma = \begin{pmatrix} \sigma_{11} & \sigma_{12} & \sigma_{13} \\ \sigma_{21} & \sigma_{22} & \sigma_{23} \\ \sigma_{31} & \sigma_{22} & \sigma_{33} \end{pmatrix}. \tag{2.14}$$

With that and a similar extension of the strain in each possible direction, we can write (2.13) as

$$\sigma_{ij} = \sum_{k,l} C_{ijkl}\epsilon_{kl}. \tag{2.15}$$

This expression can be reduced to

$$\sigma_m = \sum_{n=1}^{6} C_{mn}\epsilon_n \tag{2.16}$$

using the Voigt notation [19]. In the case of cubic systems which are the most important ones for this work, this reduces to only C_{11}, C_{12} and C_{44}. From these, more properties of solids can be derived, such as the bulk modulus

$$B = \frac{C_{11} + 2C_{12}}{3}. \tag{2.17}$$

While C_{11} is related to the uniaxial stress and strain, C_{12} gives insight into the expansion in a perpendicular direction to a strain and C_{44} contains information about the shearing

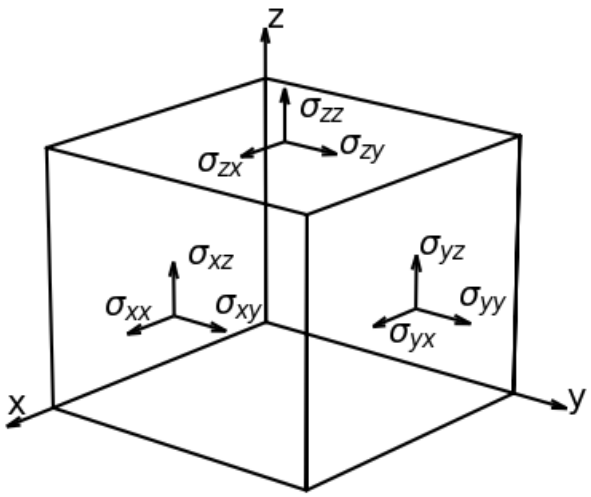

Figure 2.3: Visualisation of the components of the stress tensor in Voigt notation. The arrows indicate the stress components upon a general strain.

behaviour. Finally, the bulk modulus describes the change in volume under a uniform compression over the entire body. Technically, there are more elastic moduli that we can calculate from the elastic constants. Since we are not going to use any modulus that we haven't mentioned yet, we are not going to describe them. Details on these moduli can be found elsewhere, for example [18].
Born derived three stability criteria for cubic systems based on the elastic constants [20] which were extended to structures with other symmetries. An overview of these criteria can be found in [21]. In cubic systems, the criteria read

$$C_{11} - C_{12} > 0 \quad , \quad C_{11} + 2C_{12} > 0 \quad \text{and} \quad C_{44} > 0. \tag{2.18}$$

These criteria can be reformulated to

$$C_{11} > 0 \quad , \quad C_{11} > C_{12} \quad \text{and} \quad C_{44} > 0. \tag{2.19}$$

In the python module Elastic [22, 23, 24], a scheme that calculates the elastic constants C_{11}, C_{12} and C_{44} is already implemented. Here, a number of atom configurations are created that differ by a given percentage from the energetically most favourable one. Among the distorted ground state structure are systems with rescaled atom positions, as well as shearing of the simulation box. For each of these systems, stress and strain are calculated and combining results from each system, the elastic constants are obtained.

2.3.2 Phonons

Phonons are the quasiparticles of the lattice vibrations. In classical theory, they can be derived from the equation of motion of e.g. a one-dimensional chain of one or two types

of atoms. Details on the classical theory can be found in many textbooks, such as [18]. Here, we only note the most important results from classical theory. We differentiate between acoustical modes and optical modes. In acoustical modes, neighbouring atoms move in phase similar to how pressure waves propagate, thus the name. In optical modes, the atoms move out of phase. The name stems from the fact that due to the movement out of phase, dipole moments can be induced which can be excited by light in the visible range. Both optical and acoustical modes can be further divided into transversal and longitudinal modes depending on the direction of propagation with respect to the movement of the atoms. Generally, the frequencies of the longitudinal mode is higher than the optical mode which makes identifying the modes easier. In the three-dimensional case of a periodic system containing N atoms, there are $3N$ modes, three acoustical modes and $3N-3$ optical modes. That means that in a monoatomic system, there are only three acoustical modes and no optical modes.

For the derivation of phonons of a general many-body system and the basics on phonon calculations, we closely follow [25]. Let H be the Hamilton operator of a system of N interacting atoms. H thus has the form

$$H = \sum_{i=1}^{N} \frac{\vec{p}_i^{\,2}}{2m_i} + V(\vec{r}_1, ..., \vec{r}_N). \tag{2.20}$$

Assuming that there is an equilibrium position $\vec{r}_i^{\,(0)}$ of each atom i and that the atoms are moved out of their equilibrium positions by $\vec{u}_i$, the actual positions are given by

$$\vec{r}_i = \vec{r}_i^{\,(0)} + \vec{u}_i. \tag{2.21}$$

Next, we can expand the interaction potential around the equilibrium positions as

$$\begin{aligned} V(\vec{r}_1, ..., \vec{r}_N) =& V\left(\vec{r}_1^{\,(0)}, ..., \vec{r}_N^{\,(0)}\right) + \sum_{i=1}^{N} \left.\frac{\partial V(\vec{r}_1, ..., \vec{r}_N)}{\partial \vec{r}_i}\right|_{\left(\vec{r}_1^{\,(0)}, ..., \vec{r}_N^{\,(0)}\right)} \left(\vec{r}_i - \vec{r}_i^{\,(0)}\right) \\ &+ \frac{1}{2} \sum_{i,j=1}^{N} \left.\frac{\partial^2 V(\vec{r}_1, ..., \vec{r}_N)}{\partial \vec{r}_i \partial \vec{r}_j}\right|_{\left(\vec{r}_1^{\,(0)}, ..., \vec{r}_N^{\,(0)}\right)} \left(\vec{r}_i - \vec{r}_i^{\,(0)}\right)\left(\vec{r}_j - \vec{r}_j^{\,(0)}\right) \\ &+ \mathcal{O}\left((\vec{r}_i - \vec{r}_j)^3\right) \\ \approx& V\left(\vec{r}_1^{\,(0)}, ..., \vec{r}_N^{\,(0)}\right) + \sum_{i=1}^{N} \left.\frac{\partial V(\vec{r}_1, ..., \vec{r}_N)}{\partial \vec{r}_i}\right|_{\left(\vec{r}_1^{\,(0)}, ..., \vec{r}_N^{\,(0)}\right)} u_{i;\alpha} \\ &+ \frac{1}{2} \sum_{i,j=1}^{N} \left.\frac{\partial^2 V(\vec{r}_1, ..., \vec{r}_N)}{\partial \vec{r}_i \partial \vec{r}_j}\right|_{\left(\vec{r}_1^{\,(0)}, ..., \vec{r}_N^{\,(0)}\right)} u_{i;\alpha} u_{j;\beta}. \end{aligned} \tag{2.22}$$

Only taking contributions up to the second order in u into account, we find the harmonic

approximation within which we can conveniently write

$$\begin{aligned} V(\vec{r}_1, ..., \vec{r}_N) \approx & V\left(\vec{R}^{(0)}\right) + \sum_{i;\alpha}^{N} \frac{\partial V(\vec{r}_1, ..., \vec{r}_N)}{\partial r_{i;\alpha}}\bigg|_{\vec{R}^{(0)}} u_{i;\alpha} \\ = & \frac{1}{2} \sum_{i,j;\alpha,\beta} \frac{\partial^2 V(\vec{r}_1, ..., \vec{r}_N)}{\partial r_{i;\alpha} \partial r_j; \beta}\bigg|_{\vec{R}^{(0)}} u_{i;\alpha} u_{j;\beta} \end{aligned} \tag{2.23}$$

where

$$\vec{R}^{(0)} = \left(\vec{r}_1^{(0)}, ..., \vec{r}_N^{(0)}\right) \tag{2.24}$$

and α and β run over the spacial dimensions. The term linear in u vanishes since the forces

$$\vec{F}_i = -\frac{\partial V(\vec{r}_1, ..., \vec{r}_N)}{\partial \vec{r}_i} \tag{2.25}$$

vanish in the equilibrium positions $\vec{r}_i^{(0)}$. Furthermore, we know that the matrix

$$\Phi_{i,j;\alpha,\beta} := \frac{\partial^2 V(\vec{r}_1, ..., \vec{r}_N)}{\partial r_{i;\alpha} \partial r_{j;\beta}}\bigg|_{\vec{R}^{(0)}} = -\frac{\partial F_{i;\alpha}(\vec{r}_1, ..., \vec{r}_N)}{\partial r_{j;\beta}}\bigg|_{\vec{R}^{(0)}} \tag{2.26}$$

contains all force constants. We can write the equation of motion for particle i with the mass m_i in the potential of all N atoms as

$$m_i \ddot{u}_{i;\alpha} = \Phi_{i,j;\alpha,\beta} u_{j;\beta}. \tag{2.27}$$

With a suiting ansatz, we can find the eigenvalue problem

$$\sum_{j;\beta} D_{i,j;\alpha,\beta}(\vec{q}) \epsilon_{j;\beta;\nu}(\vec{q}) = \omega_\nu^2(\vec{q}) \epsilon_{i;\alpha;\nu}(\vec{q}) \tag{2.28}$$

with

$$D_{i,j;\alpha,\beta}(\vec{q}) = \frac{1}{\sqrt{m_i m_j}} \Phi_{i,j;\alpha,\beta} \mathrm{e}^{i\vec{q}\cdot\left(\vec{R}_j - \vec{R}_i\right)}. \tag{2.29}$$

Therefore, we can find the phonon modes $\epsilon_{i;\alpha;\nu}(\vec{q})$ and their respective frequencies ω_ν at any given point in reciprocal space $\vec{q}$. One can identify the dynamical matrix $D_{i,j;\alpha,\beta}$ as the Fourier transform of the matrix containing all the force constants (2.26). As in classical theory of phonons, there are $3N$ modes, indicated by the dimension of the dynamical matrix.

We can relate phonon frequencies to bond strength. In the simple case of a 1D-chain with one or two types of atoms, an analytical calculations reveals that the phonon frequencies are proportional to the root of the force constants between neighbouring atoms. In general, with the help of the dynamical matrix, we find that the phonon frequencies increase with the force constants.

When doing DFT phonon calculations, all the force constants can in principle be obtained by displacing atoms in the finite difference method or from DFPT calculations. While both methods are mathematically equivalent, we choose to do the calculations with DFPT due to the elegance of this method and the reduced number of separate calculations that are needed compared to the method using displacements.
Either way, we calculate the phonon dispersion along some path connecting important points in reciprocal space. Suggested paths can be found using tools like *SeeK-path* [26] which in turn uses *spglib* [27]. Of course, one has to ensure that the proposed path is reasonable and one has to be careful when comparing phonon spectra with publications which might have chosen a different path.

2.3.3 Density of state

The DOS either describes the number of states that have an energy within a certain range $D(E)$ or the number of states within a given volume in reciprocal space.
The easiest approach to the concept of the DOS is to consider a free electron gas. The gas is described in more detail in appendix B. For the free electron gas, we find that the allowed states are equidistant in reciprocal space. Assuming that the states are L_i apart in direction i and the dimension of the system is n, we find that if cutting equally large bodies which only contain one state, each body has a volume of

$$V_r = \frac{(2\pi)^n}{\prod_{i=1}^{n} L_i}. \tag{2.30}$$

Also taking both spin direction into account, the density of the states are twice the inverse of V_b, i.e.

$$Z(k) = 2\frac{\prod_{i=1}^{n} L_i}{(2\pi)^n} = 2\frac{V}{(2\pi)^n}. \tag{2.31}$$

This is the DOS in k-space. Alternatively, the DOS can be stated in energy space from the conservation of states

$$Z(k)\,\mathrm{d}^3k = D(E)\,\mathrm{d}E\,. \tag{2.32}$$

This equation can be solved for a free electron gas in the volume Ω, the calculation is given in appendix B, in three dimensions resulting in the well-known square root-like shape

$$D(E) = \frac{\Omega}{2\pi^2}\left(\frac{2m}{\hbar^2}\right)^{3/2}\sqrt{E}. \tag{2.33}$$

This concept can of course also be applied to materials that cannot be described by the free electron gas, e.g. atoms with d-electrons like copper. Still, it can be used for more insight into the electronic configurations without the knowledge of exact wave functions.
Since the expression of the free electron DOS is fairly simple, it can be used in combination with the Sommerfeld model. The Sommerfeld model is a low-temperature approximations of thermodynamic properties from the DOS. In appendix B, we derive several of such thermodynamic properties within this approximation so that we can compare this theoretical approach to our DFT calculations.

Chapter 3

Computational details

At the beginning of this work, the calculations were performed on a dedicated machine at our institute. There, calculations could be run on up to 12 cores, however, less than that was actually used due to the limited memory available. We were limited to smaller systems containing around 30 atoms with calculation runtimes around one day for structural optimizations. Since we wanted and sometimes had to consider larger systems, especially for the alloys, we switched to the supercomputer Hawk at the Hochleistungsrechenzentrum Stuttgart (HLRS). Doing so allows us to perform calculations on thousands of cores. We limit ourselves to single-node jobs, i.e. a maximum of 128 cores.
For an efficient usage of expensive computational time, we first perform benchmark calculations to find the ideal number or range of cores to use for a single calculation. As with all computer-based calculations with several cores and compute nodes, one has to find a compromise between the computational load on a single core and the communication between the cores. We therefore performed a static electronic optimization of an aluminium system containing 108 atoms in an Face-centered cubic (fcc) structure using VASP on different numbers of cores in a reasonable range. We repeat this three times to get an estimate of the deviations among runs. The needed runtimes are shown in figure 3.1. The minimum runtime for the benchmark calculation lies at 55 cores. For most calculations, however, we only use 50 cores due to the enormous memory requirements and to have a larger buffer for avoiding *out of memory* situations where the calculations require more memory than is available. In figure 3.2, we also show the parallelisation speedup of the calculations with the increase in the number of cores. Unfortunately, the code doesn't scale very well with the number of cores and quickly deviates from the ideal parallelisation speedup.
For a more efficient use of the entire node, we perform two calculations simultaneously. We track the process IDs of each newly started VASP calculation and regularly check if they are still running. If we detect that one calculation has finished, i.e. the number of process IDs has reduced, we start a new calculation. At first glance, this might not look like it saves a lot of computational time. However, if we only started two calculations at the same time and wait for both having finished before we start the next pair, half of the node might not be used for some time if one of the calculations needs significantly more time than the other. Especially when performing a series of calculations at different electron

temperatures, we found that this method greatly accelerates the calculations and uses the available resources more efficiently.
For the calculations of the DOS, we increase the number of k-points significantly. Since we are limited in terms of memory for all the wave functions, we reduce the size of the system and reduce the number of cores reserved for the calculations to 70 while only using 50 of them. This helps to avoid *out of memory* situations even further.
The phonon calculations were done again on 50 cores, however not in parallel. This is due to the increased memory requirements since we used a 9x9x9 k-space grid and fairly large systems.

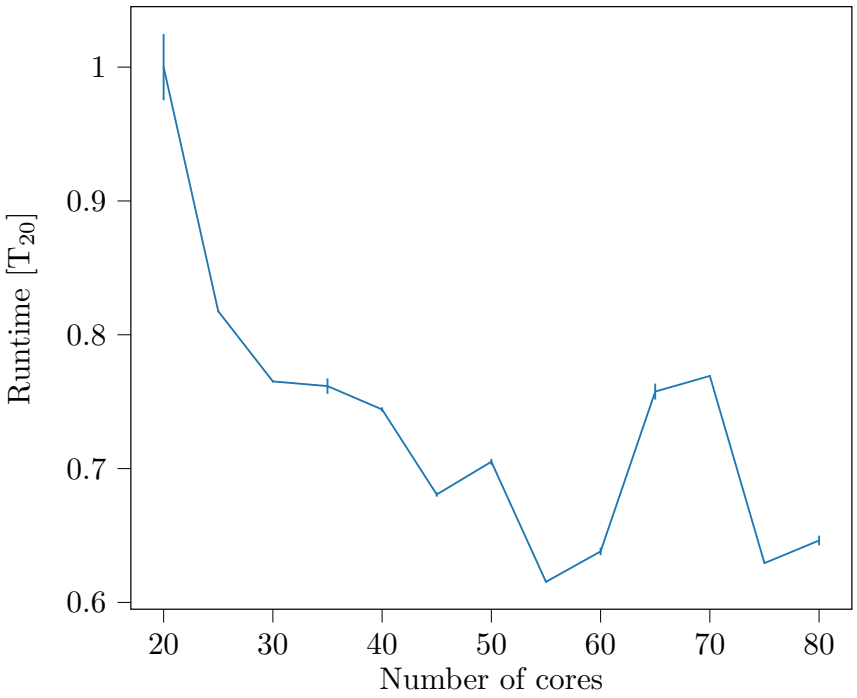

Figure 3.1: Runtimes of an electronic optimization using VASP on different numbers of cores.

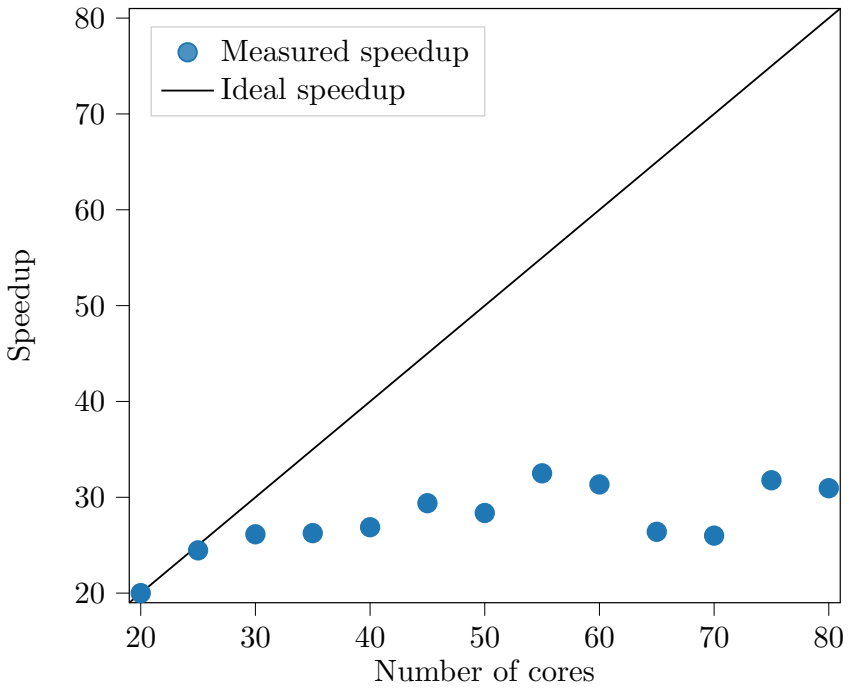

Figure 3.2: Speedup of an electronic optimization using VASP on different numbers of cores.

Chapter 4

DFT parameter analysis

Even though DFT calculations belong to the *ab initio* calculations, i.e. calculations that require no prior knowledge of the systems, several parameters can be tweaked in such calculations. In particular, the cutoff energy of the wave functions that will be taken into account, the density of the k-space grid, the convergence criterion of the electronic and atomic optimisation, as well as the system size have an effect on the quality of the results. In this chapter, we test each of these parameters and discuss their influence and which parameters will be chosen for the production of results.
All calculations for this parameter analysis were performed for pure aluminium and copper in an fcc structure consisting of 32 atoms, i.e. two unit cells in each direction. To ensure that the parameters are also appropriate for larger systems, we repeated some calculations for the larger system but will not show them here since the results were the same. Some calculations for the Al-Cu alloys were repeated with different sets of parameters but found the same convergence as for the pure metals. In order to avoid redundancy in this chapter, we only show the results on pure aluminium and copper. Since we didn't decide on an exchange-correlation functional at this point, we performed all calculations with both, LDA and PBE.

4.1 Cutoff energy

As the complete wave functions are assumed to be a superposition of plane waves, the kinetic energy of such waves can be arbitrarily high. Since wave functions with high energies are energetically unreasonable and thus barely contribute, only plane waves with a maximum energy

$$E_{\text{cut}} = \frac{\hbar^2 G_{\text{cut}}^2}{2m} \quad , \quad \left|\vec{k} + \vec{G}\right| < G_{\text{cut}} \tag{4.1}$$

or lower are taken into account. The DFT code VASP that is used in this work suggests an appropriate value but we found it worth investigating whether the energy actually converges when increasing the cutoff energy. The calculated energies per atom depending on the cutoff energy for each of the combinations of material and exchange-correlation

functional are shown in figure 4.1a and shifted for an easier presentation in figure 4.1b. From the latter plot, it can be seen more easily that a cutoff energy $E_{\text{cut}} = 500\,\text{eV}$ is a reasonable cutoff and will therefore be used in all following calculations. This value is much higher for both Al and Cu than suggested by VASP but since we expect more wave functions with higher energies to be relevant at higher electron temperatures, we will use this higher cutoff energy. Also, by using such a high cutoff energy, we also avoid Pulay stresses that arise due to the incompleteness of our basis set.

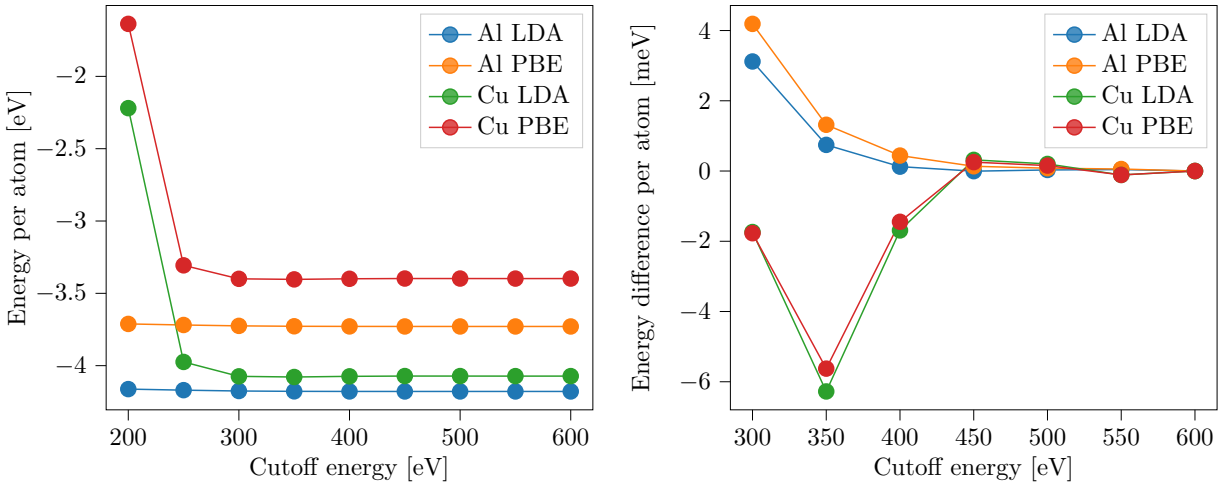

(a) (b)

Figure 4.1: Energy per atom depending on the cutoff energy used during VASP calculations of 32 Al or Cu atoms using LDA or PBE. In (a), the exact values are shown. In (b), the energies are shifted so that the energy per atom at the largest cutoff energy is the same in all plots.

4.2 K-space grid

Next, the density of the k-space grid has to be adjusted such that the energy converges. As can be seen in figure 4.2a and shifted for an easier presentation in figure 4.2b, the energy converges quickly when increasing the density of the k-space grid and only changes by a small amount starting at four points per dimension for each material and functional. To be safe, a 6x6x6 grid is chosen and convergence is checked regularly in case this choice isn't applicable for different structures or electron temperatures.

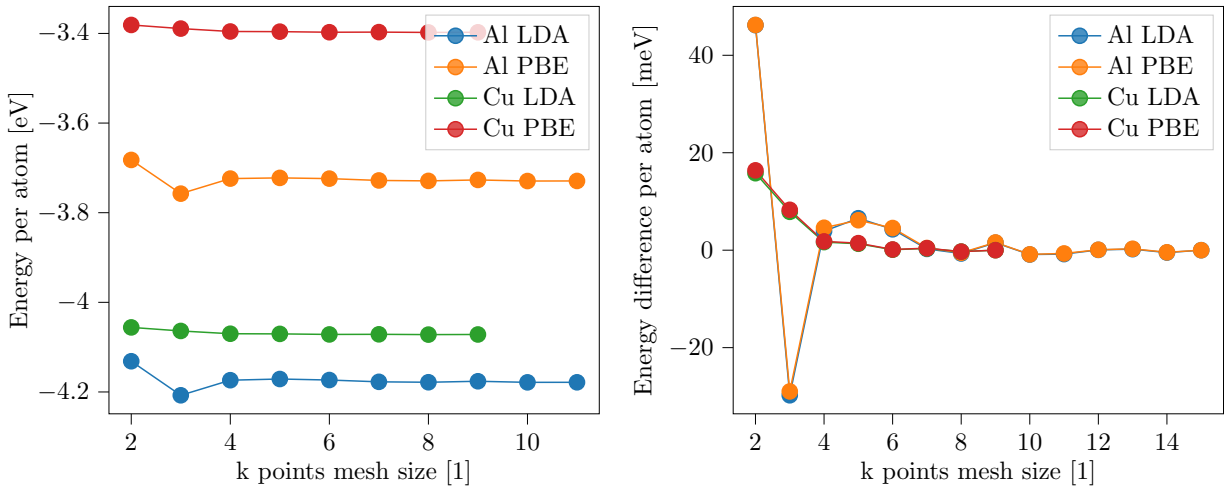

Figure 4.2: Energy per atom depending on the k-space grid size used during VASP calculations of 32 atoms in an fcc structure using LDA or PBE. In (a), the exact values are shown. In (b), the energies are shifted so that the energy per atom at the largest cutoff energy is the same in all plots.

4.3 Convergence criteria of DFT

Besides the cutoff energy and k-space grid, also the convergence criterion of our DFT calculation can be adjusted. In all calculations with the focus on structural information and thermodynamic properties of the structures, an accuracy $E_{\text{conv}} = 1 \cdot 10^{-4}\,\text{eV}$ is chosen. For the phonon spectra, we choose $E_{\text{conv}} = 1 \cdot 10^{-6}\,\text{eV}$ since phonon calculations rely on small differences in the energies.
Besides the energy convergence, it is checked regularly whether the structure is relaxed as well by ensuring that the forces are small. As a criterion, all forces have to be smaller than $1 \cdot 10^{-3}\,\text{eV/Å}$ for the structural optimisation. Since we fix the structures for the phonon calculations, this atomic convergence criterion is irrelevant for these calculation.

4.4 Number of MD steps

During the production runs, the atoms are allowed to change their positions according to a CG algorithm. In case, the atoms were in an originally unfavourable configuration, they can thus move towards an energetically more favourable configuration according to a CG algorithm. Benchmarking runs with 32 and 108 atoms in different configurations have shown that the maximum number of MD steps of 30 is generally sufficient but is checked regularly if a structural optimisation is performed starting with a structure that differs greatly from the relaxed structure.

4.5 System size

Of course, the number of atoms in the system has an effect on the accuracy of the physical quantities acquired by statistics. Benchmark calculations, however, revealed that due to Periodic boundary conditions (PBCs), the energies are only slightly influenced by the system size. As will be shown later, the elastic constants showed an improvement for a larger system compared to a smaller system.
Since phonon calculations rely on small energy differences, the system has to be chosen as large as possible, whereas for the calculations of the electron DOS, the quality of the DOS barely depends on the system size. Also, we can't choose the system size as large as we otherwise do due to the increased density of the k-space grid needed for DOS calculations.

Chapter 5

Analysis

This chapter is mainly divided into two parts. The first part consisting of section 5.1 and section 5.2 is dedicated to finding the ground state structures, their cohesive energies and the elastic constants of pure aluminium and copper, as well as their alloys. The second part consisting of section 5.3 and section 5.4 is dedicated to the change in properties occurring in excited materials. In section 5.3, we calculate the relaxed structures at different electron temperatures, several thermodynamic properties in the relaxed structures and the unexcited structures, electron temperature-dependent elastic constants and phonon spectra and the density of states of pure aluminium and copper and repeat the same in section 5.4 for the Al-Cu alloys.

5.1 Properties of non-excited Al and Cu

We start the analysis by doing ground state calculations on pure aluminium and copper. We first discuss two methods of finding the relaxed structure. Having found these structures, we can calculate the cohesive energy, as well as elastic constants and compare them to other investigations of the materials of interest.

5.1.1 Most favourable structures of Al and Cu

In order to find the relaxed structure, we have in principle two different approaches with different advantages and disadvantages. One is performing several DFT calculations on systems with different volumes and each with fixed atomic positions and fixed box volume. The minimum energy among these calculations yields the relaxed structure. We will call this method *static relaxation* because the structure remains static during each calculation. On the other hand, one can use some MD-DFT method, or in our case a CG algorithm with a simulation box that is allowed to change in volume and shape and atom positions that can change to relax the structure that we will call *dynymic relaxation*. While the latter seems like an easy choice, this relaxation method can take a long time or might not relax into the correct structure if the initial structure differs too much from the relaxed

structure. Furthermore, within the atomic convergence criterion of the dynamic relaxation, the dynamic relaxation could yield a much more precise relaxed structure given the same electronic convergence criterion. What's more is the fact that we can find the energetically most favourable structure for structures that are not as stable as the true ground state structure, for example the Basis-centered cubic (bcc) and Simple cubic (sc) structure in aluminium even though the fcc structure is the most stable one. The atomic relaxation could potentially lead to a phase transformation which in some cases is not wanted when starting in a structure that is not the ground state structure.
We test both methods on pure aluminium and copper systems, consisting of 32 atoms in an fcc structure, a bcc structure with 16 atoms and an sc structure with eight atoms, i.e. two unit cells in each direction for each structure. For the fcc structure, we also perform the structure relaxation for a system consisting of 108 atoms in the fcc structure to show the accuracy of the smaller systems compared to the larger ones.
In figure 5.1, the energies per atom are shown for these three structures depending on the lattice constant using an LDA or PBE functional since at this point, we haven't chosen the exchange-correlation functional that we want to use for the rest of the calculations yet. Each curve is accompanied by a flat-looking line which is obtained from a dynamic relaxation. In figure 5.2, the energy per atom is shown in the same way for Cu.
Especially for copper, we find that during a dynamic relaxation, the starting lattice constant must be very close to the energetically most favourable one. Therefore and in general, the starting configuration has to be chosen with care and plausibility has to be checked.

The lattice constants which lead to the minimum energy in Al and Cu for each structure and using the LDA and PBE exchange-correlation functional are listed in table 5.1. As can be seen, calculations with the LDA functional leads to slightly smaller lattice constants compared to calculations with the PBE functional. This overbinding of LDA functionals is well-known, as well as the fact that LDA generally produces lower energies as shown in figure 5.1. The larger systems yielded the exact same ground state lattice constant. The obtained lattice constants of aluminium and copper are comparable to the ones obtained from x-ray diffraction experiments 4.046 Å and 3.597 Å respectively [28].
Since the DFT calculations are performed at zero-temperature, some deviations from experimental results which usually are performed at room temperature, are expected. However, this technically incorrect temperature should only barely affect the calculated structures since even room temperature is a comparably low temperature. We assume that the shortcomings of the exchange-correlation functionals are much greater than the error introduced by different but low temperatures.

5.1.2 Cohesive energy of Al and Cu structures

The cohesive energy is the energy gained by atoms when forming structures that are energetically more favourable than unbound atoms. It can be obtained from ab initio calculations by calculating the energy of a single atom E_s and the bulk structure consisting

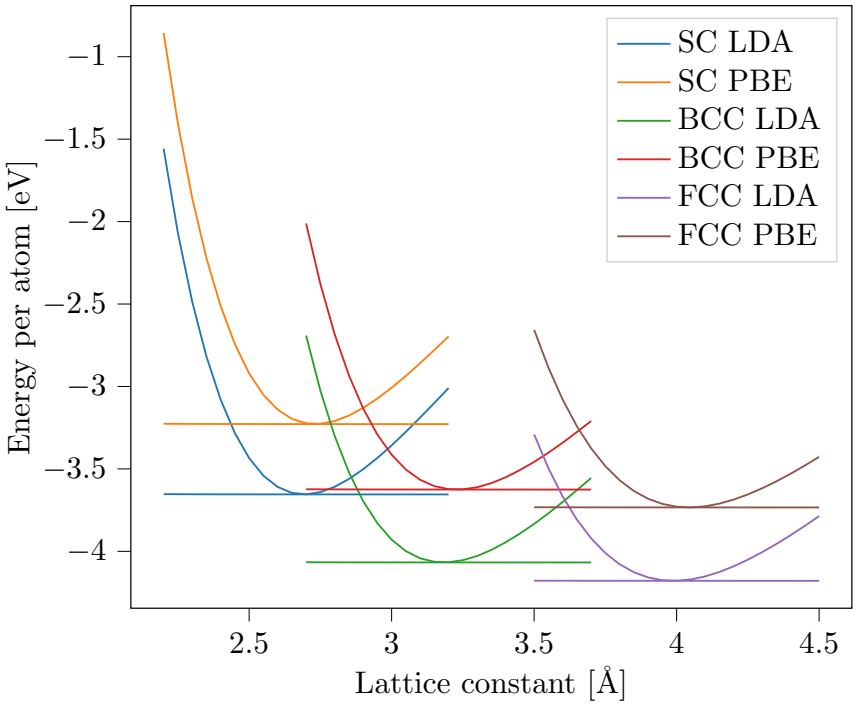

Figure 5.1: Energy per atom depending on the lattice constant used during VASP calculations of 32 Al atoms using LDA or PBE. Each curve is accompanied by a flat-looking line which is obtained from a structure with the given lattice constant but was allowed to move to the structure with the lowest energy by changing the shape and size of the simulation box.

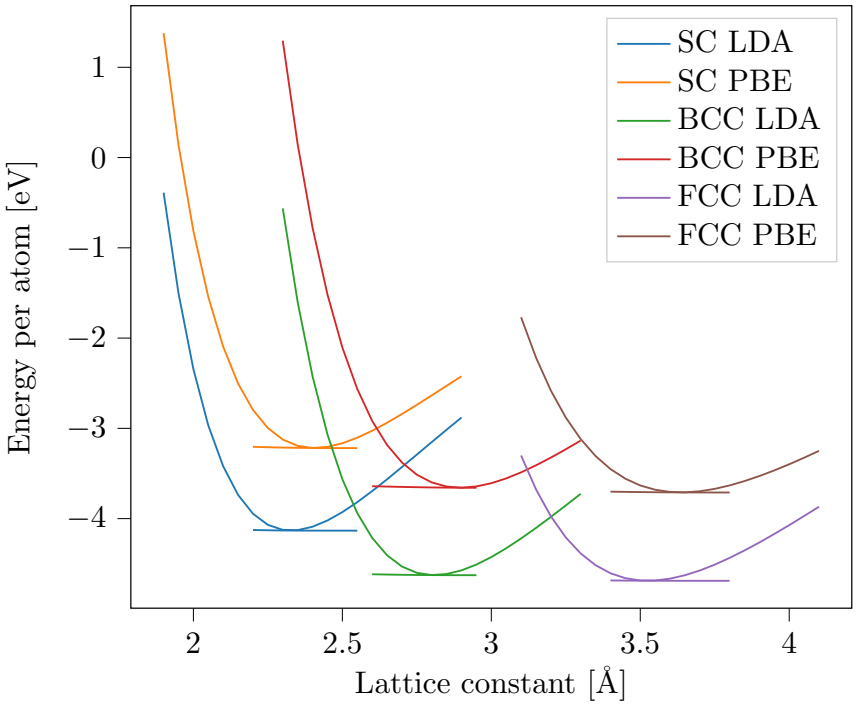

Figure 5.2: Energy per atom depending on the lattice constant used during VASP calculations of 32 Cu atoms using LDA or PBE. Each curve is accompanied by a flat-looking line which is obtained from a structure with the given lattice constant but was allowed to move to the structure with the lowest energy by changing the shape and size of the simulation box.

Table 5.1: Lattice constants which result in minimal energy in different structures using an LDA or PBE functional. All values constants are given in Å.

	FCC LDA	FCC PBE	BCC LDA	BCC PBE	SC LDA	SC PBE
Al	3.99	4.04	3.19	3.24	2.69	2.73
Cu	3.52	3.64	2.81	2.90	2.33	2.40
Al, large	4.03	4.04	-	-	-	-
Cu, large	3.63	3.64	-	-	-	-

of n_s atoms E_bulk. Then, the cohesive energy per atom is given by

$$E_\mathrm{coh} = \frac{E_\mathrm{bulk} - n_\mathrm{s} E_\mathrm{s}}{n_\mathrm{s}}. \tag{5.1}$$

In the case of the single-atom calculations, the spin polarization of the atom has to be taken into account. Technically, spin polarization could be included in all calculations but it is known that in bulk, spin polarization doesn't occur and can therefore be neglected. Furthermore, it has to be ensured that the system is large enough so that the atom doesn't interact with itself due to PBCs. Therefore, single-atom calculations are performed for different system sizes. The resulting energies depending on the system size for aluminium and copper calculated with LDA and PBE are shown in figure 5.3

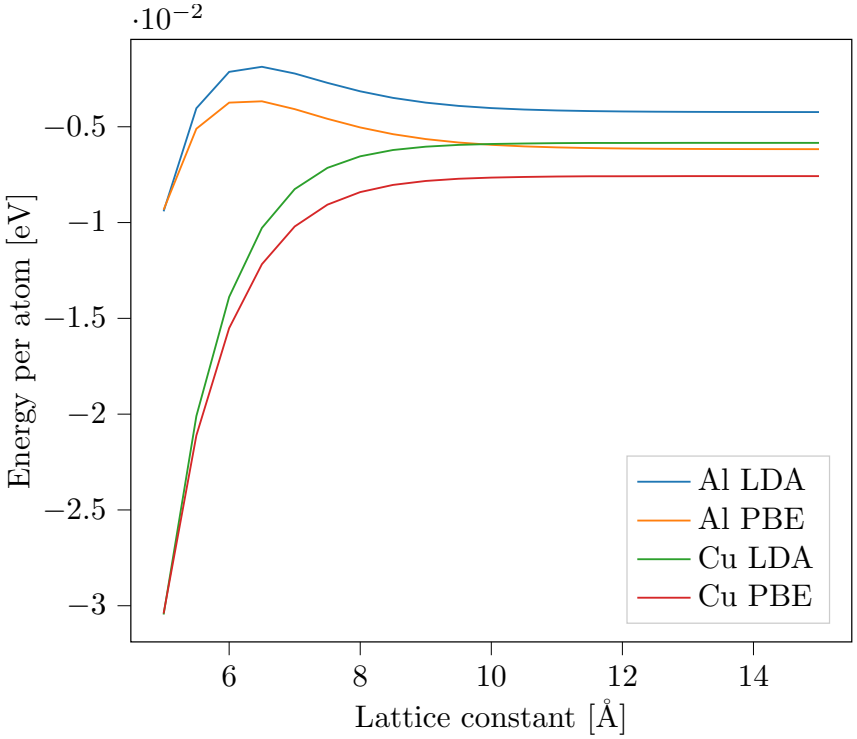

Figure 5.3: Single-atom energies of aluminium and copper calculated with LDA and PBE depending on the system size.

As can be seen in figure 5.3, the single-atom energy converges nicely. To be save, the value corresponding to the largest system is chosen to calculate the cohesive energy. The single-atom energies and bulk energies of an fcc structure consisting of 108 atom are listed in table 5.2 together with the resulting cohesive energy calculated using (5.1). The experimentally determined cohesive energy of aluminium are also given in table 5.2. Note that in literature, the cohesive energy is often stated as a positive value. However, calculated from (5.1), the cohesive energy is negative for a stable structure. Only looking at the absolute value of the cohesive energy, it can be concluded that the calculations using PBE are very close to the experimental values with deviations of a few percent but the calculations using LDA generally result in cohesive energies that are too large. This behaviour was also observed in other investigations using these functionals [29].

Table 5.2: Single atom energies and bulk energies from fcc structures consisting of 108 atoms using LDA and PBE for aluminium and copper, as well as the resulting cohesive energies.

Material	Functional	E_{s} [eV]	E_{bulk} [eV]	E_{coh} [eV]	$E_{\mathrm{coh}}^{\mathrm{exp}}[eV]$
Al	LDA	-0.135	-405.846	-3.622	3.39 [30]
	PBE	-0.197	-404.383	-3.547	
Cu	LDA	-0.187	-400.922	-3.525	3.49 [30]
	PBE	-0.242	-402.448	-3.484	

5.1.3 Stresses and elastic constants of Al and Cu

In this section, we calculate the elastic constants of pure aluminium and copper using the python module *Elastic* [23, 24]. For each independent direction, we distort the relaxed structure in five steps up to a maximum distortion of 2 %. While we found that the number of distortions per type of transformation barely affects the elastic constants, the size of the distortion is chosen in accordance to usual experimental values.
We perform the elastic constants calculations on systems consisting of 108 atoms of Al and Cu respectively, each in an fcc structure using both LDA and PBE and use the results of these calculations together with the previous results to decide whether we should use LDA or PBE for all following calculations.

In table 5.3, the elastic constants of aluminium and copper are given for both, LDA and PBE. Comparing these values to values that have been obtained experimentally by measuring the velocity of ultrasonic waves in longitudinal and transversal direction that are also listed in table 5.3, we see excellent agreement for copper using PBE and fairly good agreement for aluminium using PBE; the calculations using LDA seem closer to the experimental values for aluminium but greatly differ for copper.
Still it should be noted that the experimental values for both metals were obtained from experiments performed at temperatures around 4 K.

Table 5.3: Elastic constants C_{11} and C_{12} obtained from VASP calculations using an LDA and PBE functional applied to aluminium and copper.

Material	Functional	C_{11} [GPa]	C_{12} [GPa]	C_{44} [GPa]
Al	LDA	133.671	42.646	50.540
	PBE	136.331	47.475	55.145
	Experiment ([31])	116.3	64.8	30.9
Cu	LDA	145.353	115.182	58.763
	PBE	175.263	119.485	79.408
	Experiment ([32])	176.99	124.97	81.45

5.2 Properties of non-excited Al-Cu alloys

Aluminium and copper form a multitude of alloys depending on the fraction of either metal, as well as conditions like temperature. This can clearly be seen in the alloy phase diagram displayed in figure 5.4. For the applications this thesis is aimed at, the phases with low copper percentage, namely the θ and θ' phase, as well as the Guinier-Preston (GP) phase are the most important structures.
The GPI phase describes disk-like layers with a thickness of one atom and a radius of a few nanometres. In Al-Cu alloys, the copper atoms lie in the (100)-plane of the aluminium crystal. Here, the GPI phase is modelled by a monolayer of copper between 11 layers of aluminium. While this doesn't capture the full extent of this phase, it does accurately reproduce the correct copper percentage and has successfully been used previously [33].
The GPII zone, sometimes referred to as θ'' phase consists of two or more layers of (100) layers of copper separated by three layers of aluminium. In our case, two layers of copper between three layers of aluminium will be used as was in a previous DFT investigation [34].
The θ' phase is the most important phase for precipitation hardening of Al-Cu alloys. It is built up by a tetragonally distorted cubic fluorite structure when embedded in aluminium. Finally, the θ structure is incoherent to both the aluminium and the copper crystal. At lower copper percentages in the entire system, the θ structure is embedded into the surrounding aluminium lattice. If the copper percentage of the entire system is sufficiently high, the structure can form globally. The latter can only happen at $T \neq 0$ since this structure is entropically stabilised as was shown in [35].
The crystal structure of all four structures that will be considered in this work are shown in figure 5.5.

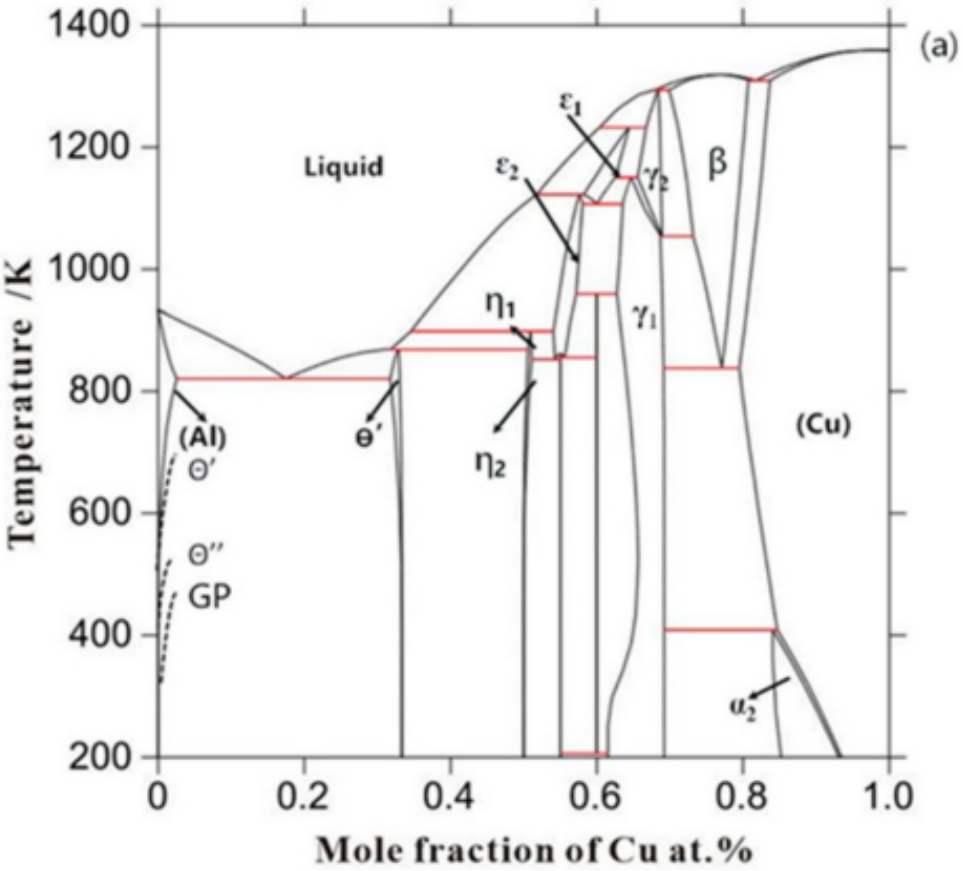

Figure 5.4: Phase diagram of Al-Cu alloys. Taken from [36].

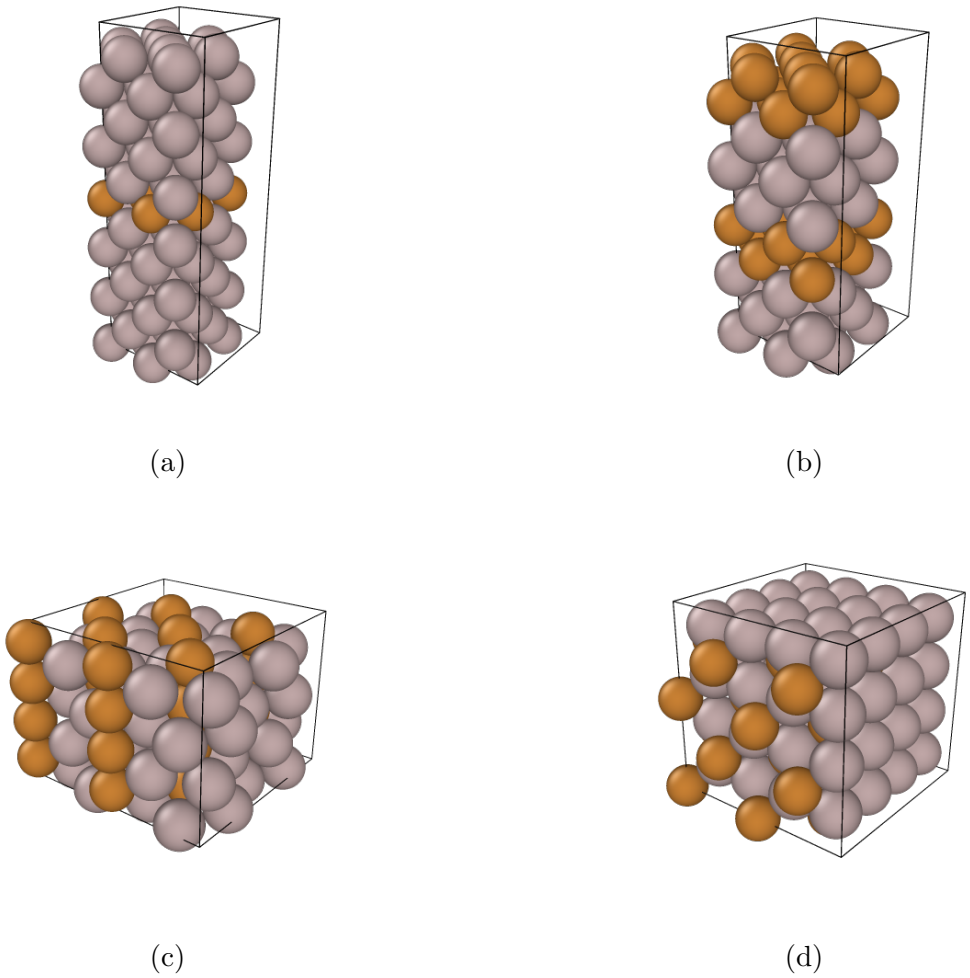

(a) (b)

(c) (d)

Figure 5.5: Al-Cu structures that will be considered in this work. (a) shows the structure that represents the GPI zone, (b) the GPII zone, (c) the θ' structure and (d) the θ structure.

5.2.1 Formation energies of non-excited Al-Cu alloys

Similar to (5.1), the formation energy of an alloy consisting of n_{Al} aluminium atoms and n_{Cu} copper atoms can be calculated via

$$E_{\mathrm{Form}} = \frac{E_{\mathrm{bulk}}^{\mathrm{alloy}} - n_{\mathrm{Al}} E_{\mathrm{bulk}}^{\mathrm{Al}} - n_{\mathrm{Cu}} E_{\mathrm{bulk}}^{\mathrm{Cu}}}{n_{\mathrm{Al}} + n_{\mathrm{Cu}}}. \tag{5.2}$$

Here, $E_{\mathrm{bulk}}^{\mathrm{alloy}}$, $E_{\mathrm{bulk}}^{\mathrm{Al}}$ and $E_{\mathrm{bulk}}^{\mathrm{Cu}}$ are the bulk energies per atom of the alloy, or pure aluminium and copper respectively. To calculate the formation energies of the four alloys that we want to focus on in this work, we use a θ (I4-mcm) structure consisting of 64 Al atoms and 32 Cu atoms, a θ' structure (I4-mmm) also consisting of 64 Al atoms and 32 Cu atoms, a GPI structure consisting of 88 Al atoms and 8 Cu atoms and a GPII structure consisting of 48 Al atoms and 32 Cu atoms. The resulting formation energies are given in

table 5.4. It turns out that the calculated formation energies of the θ and θ' structure are in line with previous investigations [34, 35]. As before, LDA delivers formation energies that are lower than the ones obtained from PBE. Still, both functionals reproduce the fact that the θ' structure has a lower energy than the θ structure at zero-temperature, as first noted by [35]. Since the θ structure is known to be entropically stabilised at temperatures far above room temperature, it can be expected that this will change at some point once electronically excited materials will be considered.

Since the formation energies are almost identical using both exchange-correlation functionals, we finally decide that PBE will be used in all further calculations, especially since the elastic constants of copper are greatly underestimated using LDA. LDA might yield slightly better results for aluminium but we want to keep all calculations consistent and since the error introduced by using LDA for copper is much greater than the error introduced by using PBE for aluminium here and in the previous section, we choose PBE for all further calculations.

Table 5.4: Bulk energies of a GPI structure consisting of 96 atoms, a GPII structure consisting of 80 atoms, a θ' structure consisting of 96 atoms and a θ structure consisting of 96 atoms using LDA and PBE, as well as the resulting formation energies of each structure.

Structure	Functional	$E_{\text{bulk}}^{\text{alloy}}$ [eV]	E_{Form} [eV]
GPI	LDA	-363.123	-0.028
	PBE	-362.051	0.029
GPII	LDA	-305.300	-0.077
	PBE	-305.103	-0.077
θ'	LDA	-375.634	-0.170
	PBE	-375.329	-0.172
θ	LDA	-374.059	-0.154
	PBE	-373.752	0.155

5.3 Properties of excited Al and Cu

In this chapter, we want to extend the previous calculations to excited aluminium, copper and their alloys. Even though, we originally weren't interested in it, we also extend many calculations in this chapter to silicon since we have more reference data for it and expect effects like bond-softening due to the excitation that is in contrast to the bond-hardening that has previously been observed in several metals.
We start by determining the relaxed structures at different electron temperatures and calculate thermodynamic properties like the internal energy, free energy in the excited and unexcited structures. Based on these calculations, we then calculate elastic constants at various degrees of excitement. Next, we want to get more insight into the structural stability which influences the melting behaviour during laser treatment by calculating the phonon spectra and make an attempt to compare our findings to an analytical approach using the DOS of each material.

5.3.1 Thermodynamic properties of excited Al and Cu

We start this part by calculating the structures in which the excited systems are relaxed. To do so, we perform a structure relaxation using the CG method mentioned previously. Doing so also gives us some insight in the free energy and the internal energy, i.e. the free energy calculated by VASP without entropy. As shown in figure 5.6, the system expands if the electron temperature is increased in aluminium and copper. We suspect that this is due to the increase in degeneracy pressure. Later, we will go into more detail as to how we get to this conclusion. Furthermore, we can see in figure 5.7 that the free energy per atom decreases for both systems. This comes to no surprise since the entropic contribution $-T_c S_\mathrm{e}$ to the free energy decreases with the electron temperature T_c. On the other hand, as can be seen in figure 5.8, the internal energy increases. In a simple perception of bond strength, this would indicate bond weakening as can be observed in silicon [37]. It is very important to note that the concept of a lattice constant is not valid anymore if the internal energy is larger than zero since this indicates a purely repulsive bonding behaviour. The DFT calculations most likely only converge since, at these very high electron temperatures, the atoms have such a large distance due to the increase in pressure in the simulation box that they barely interact with each other. Within the convergence criterion, the forces at the end of a self-consistent loop and before the next MD step during the DFT calculation are small enough for convergence to be achieved.

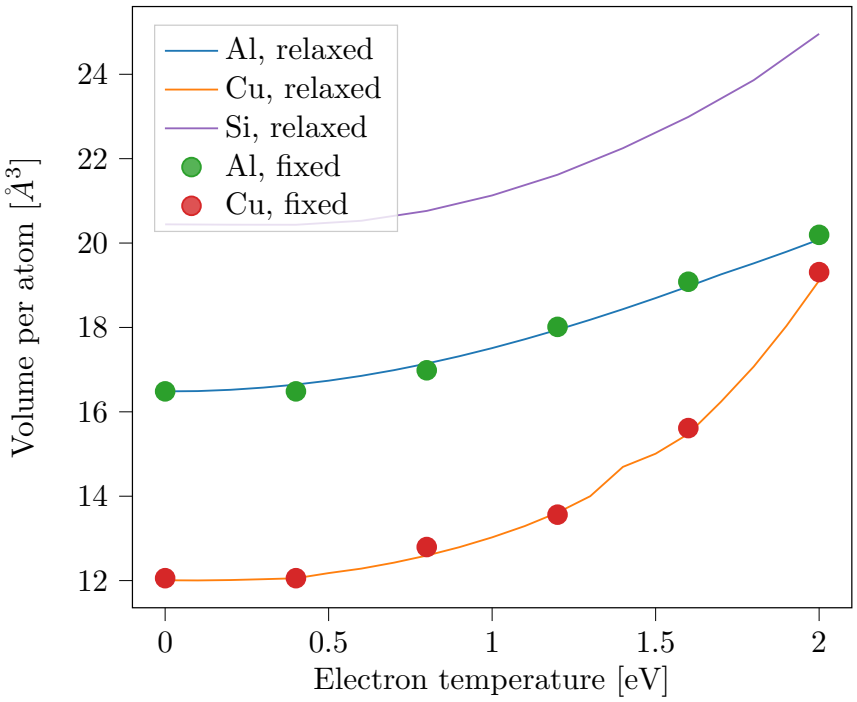

Figure 5.6: Volume per atom in Al, Cu and Si at different electron temperatures.

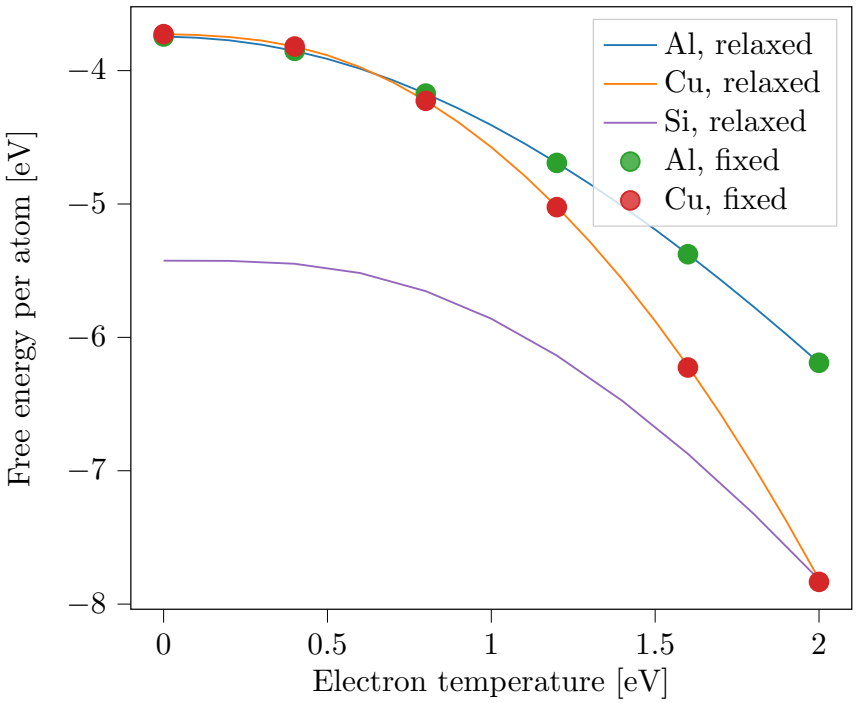

Figure 5.7: Free energy per atom in Al, Cu and Si at different electron temperatures.

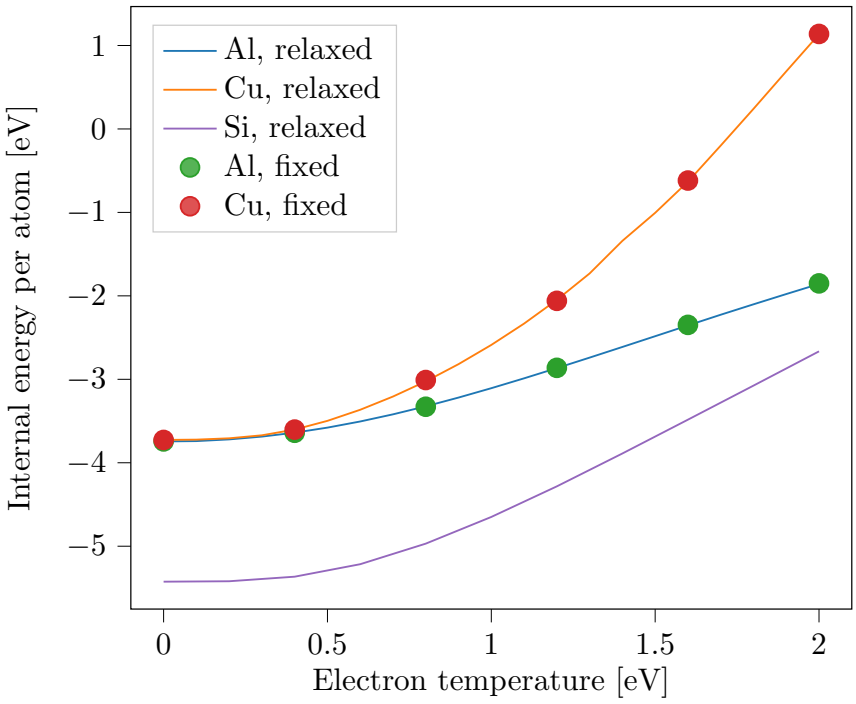

Figure 5.8: Internal energy per atom in Al, Cu and Si at different electron temperatures.

In these previous plots, we also include silicon as a comparison. The results for silicon are qualitatively very much in line with what was presented in [1]. Quantitative differences most likely only stem from the fact that in [1], LDA calculations were performed there and PBE is used here.

Since we initially didn't expect to see this expansion and increase in internal energy in metals like Al and Cu as we did in silicon, we next check whether the parameters used in our DFT calculation are appropriate for high-T_c calculations. For that, we repeat several calculations with a more strict convergence criterion, a denser k-space grid, a higher energy cutoff and number of bands considered in the calculation, as well as taking spin-polarization into account. We also test the exchange-correlation function for its validity in excited materials and limit the symmetries that VASP uses in order to accelerate the calculations. To not interrupt the reading flow too much and to avoid redundancy, we collected all the plots in appendix E. In summary, we found the parameters previously used to still be appropriate at higher T_c. Deviations between the calculations exist but are negligible since they only affect the accuracy of the calculations slightly but not their general trend. Here, it is important to note that some calculations are not repeated for the entire range of electron temperature due to the computational expense of these calculations.
As a last test, we want to avoid any simulation cell relaxation-related issues and perform a series of static relaxations in a broad range of volumes. Repeating this for several different electron temperatures yields the free energy curves shown in figure 5.9 for aluminium and in figure 5.10 for copper. Plotting the minima of the free energy curves again results in the

minimum free energy volume per atom shown in figure 5.6. Since these volumes per atom nicely match those of the complete relaxation with variable cell shape and size, we can now safely assume that no problems arise during the complete relaxation and that the volume per atom of the relaxed structure does indeed increase with the electron temperature.

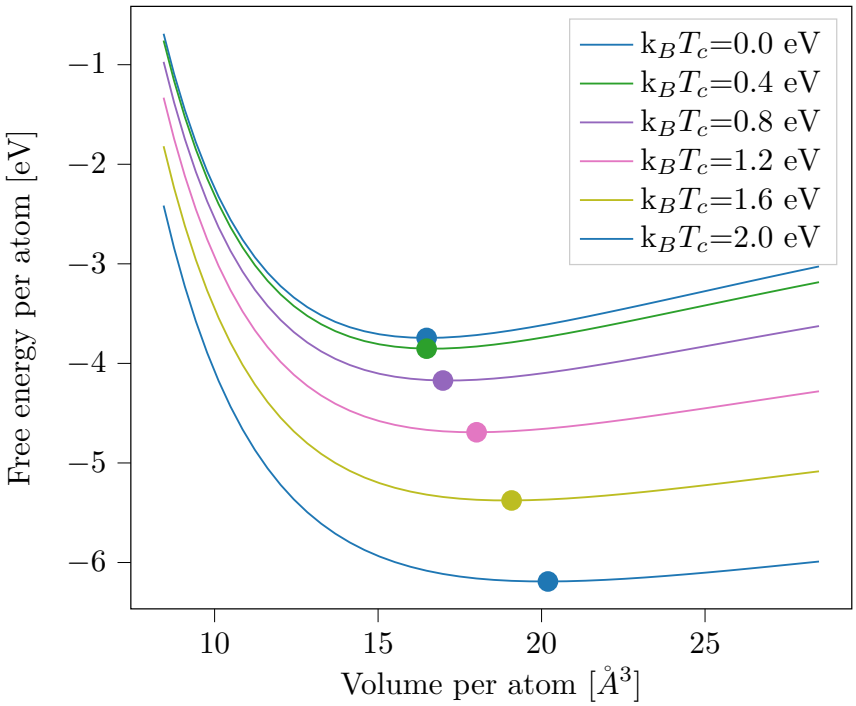

Figure 5.9: Free energy curves depending on the volume per atom for aluminium at different electron temperatures. The dots indicate the minimum of the free energy.

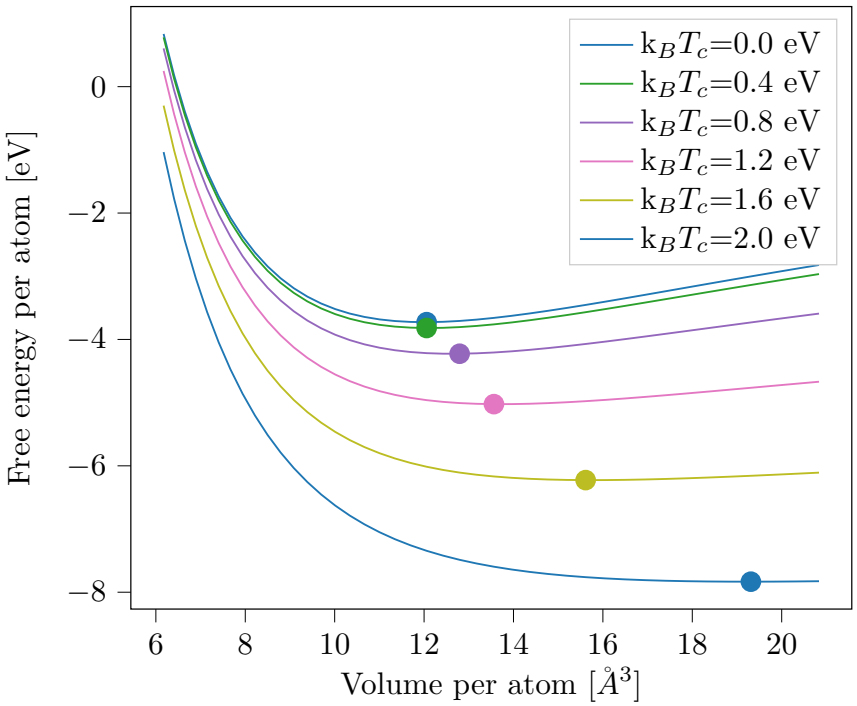

Figure 5.10: Free energy curves depending on the volume per atom for copper at different electron temperatures. The dots indicate the minimum of the free energy.

We can get more information about the expansion of our systems upon electronic excitation by performing an electronic optimization for the fixed structure at different electron temperatures. We therefore show the pressure depending on the electron temperature in Al, Cu and Si after an electronic relaxation in the ground state unexcited structures respectively. Similarly to the minima of the free energy curves at different volumes shown in figure 5.6, the pressure increases with the electron temperature for Al, Cu and Si as is shown in figure 5.11. Extrapolating the pressure in silicon to $T_c = 6\,\text{eV}$, we end up with a pressure that comes close to the 200 GPa stated in [38]. Again, an exact quantitative comparison is meaningless since in [38], LDA calculations were performed.
As indicated earlier, we also want to get more insight in the pressure arising upon electronic excitation by considering the free energy depending on the volume as was done in [39] for magnesium. For that, we use the definition of the degeneracy pressure that is described in more detail in appendix B in a simulation box with the volume V_i and approximate it using the midpoint rule

$$p_i = -\frac{\partial F}{\partial V}\bigg|_{N,T,V_i} \approx -\frac{F(V_{i+1}) - F(V_{i-1})}{V_{i+1} - V_{i-1}}. \tag{5.3}$$

We thus calculate the numerical derivative of the free energy at the ground state volume. Doing so for aluminium, copper and silicon yields the values shown in figure 5.11. The pressure obtained with this method are almost exactly the same pressures as directly

given by VASP in the ground state structure. This finally allows us to call the pressure we observed degeneracy pressure. We want to go ahead and try to compare the final expression of the expansion pressure given in (B.33) to the numerically obtained pressures.

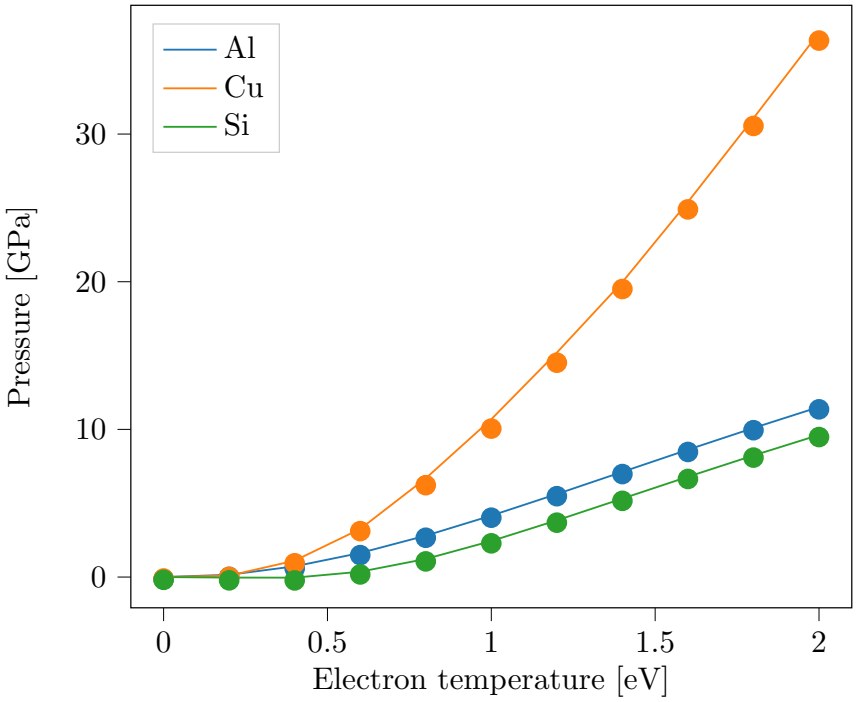

Figure 5.11: Pressure in the $T_c = 0$ structure depending on the electron temperatures in aluminium, copper and silicon. The line represents the direct output by VASP after an electronic relaxation and the dots represent the pressure from a numerical derivative of the free energy with respect to the volume from figure 5.9 and figure 5.10.

At this point, we are very certain that the results from the calculations at $T_c > 0$ are correct within the accuracy of the chosen parameters and approximations. In the next sections, we will look at other properties that sets silicon apart from the metals.
Since we're interested in ultrafast processes during laser treatment of materials, we now have to look at two kinds of systems separately: The system in which the atomic structure is unchanged while the electrons are highly excited and the completely relaxed but excited systems. This distinction will become clearer in the following section.
To get more insights in the bonding behaviour and to further validate the findings so far, we calculated both the band structure and the phonon spectra for Al, Cu and Si at different T_c. This should also allow us to compare our calculations with a wider variety of other DFT calculations.

5.3.2 Elastic constants of excited Al and Cu

We now turn to the elastic constants of pure aluminium, copper and silicon. We include silicon in these calculations since we can compare our calculations to the ones shown in [1]. Also, silicon is well-known to show bond-weakening during laser irradiation and even non-thermal melting [37, 40]. Since we expect some kind of bond-hardening in metals, we hope to differentiate between the metals and the semiconductor already from the elastic constants.

We calculate the elastic constants C_{11}, C_{12} and C_{44}, as well as the bulk modulus K in systems with their unexcited structures and the completely relaxed structures and first look at the elastic constants based on the relaxed structures at different electron temperatures. Please note again that one has to be careful with these results since they don't represent the reality of ultrafast processes where the atoms reside in the unexcited structure.

In figure 5.12, figure 5.13 and figure 5.14, the calculated elastic constants based on the relaxed structures at several given electron temperatures are shown for Al, Cu and Si respectively. Compared to the dissertation of Alexander Kiselev [1] where the elastic constants of silicon were already calculated in the same way, there is only a small deviation the elastic constants of silicon that, as before, most likely stems from the different exchange-correlation functionals. The elastic constants in figure 5.12 all decrease monotonously except for a jump in the beginning. We checked again whether this initial jump was due to a faulty calculation but this doesn't seem to be the case. The elastic constants of copper shown in figure 5.13 on the other hand show a non-monotonous behaviour.

We can apply Born's criteria (2.18) for lattice stability here. Since all three elastic constants of aluminium and silicon decrease, we expect the lattice to be unstable at electron temperatures slightly above $\mathrm{k_B}T_c = 2\,\mathrm{eV}$ in both materials. Due to the non-monotonous behaviour of the elastic constants of copper, we can't make a clear prediction of the lattice stability. This behaviour will become more obvious for all three materials when calculating the elastic constants based on the unexcited structures.

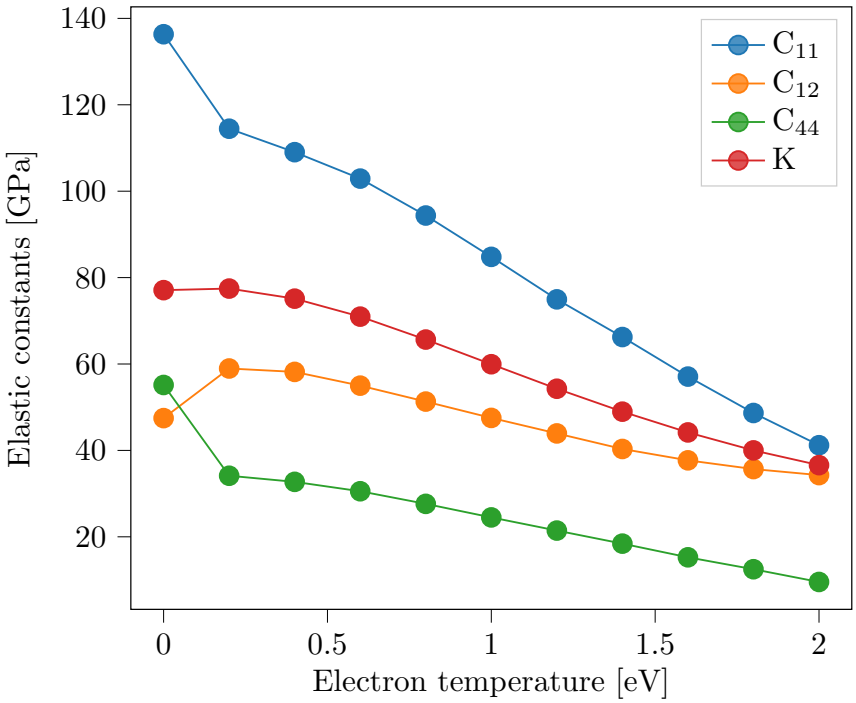

Figure 5.12: Elastic constants and bulk modulus K of Al depending on the electron temperature based on the relaxed structure at the respective electron temperature.

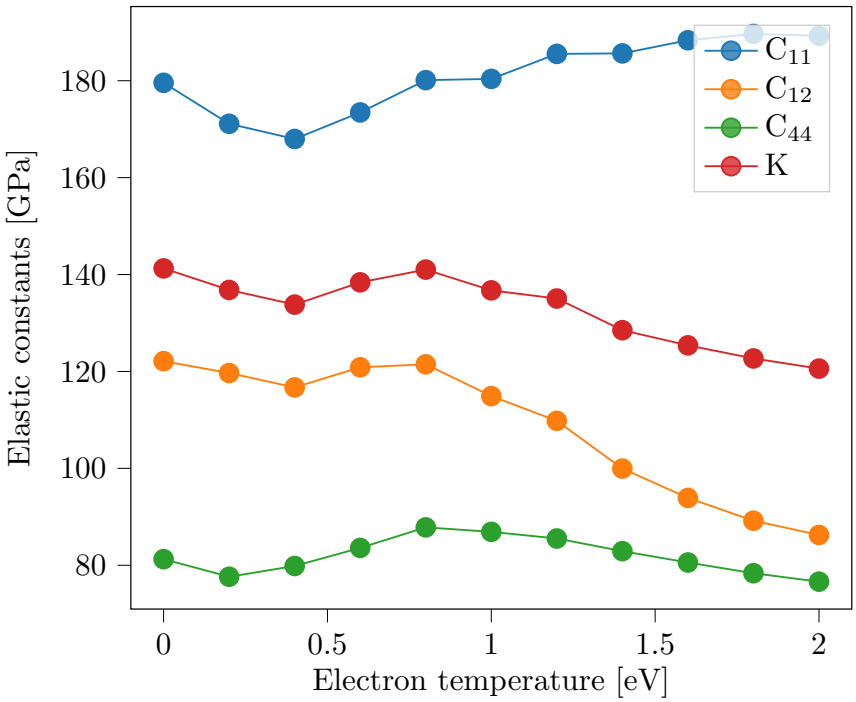

Figure 5.13: Elastic constants and bulk modulus K of Cu depending on the electron temperature based on the relaxed structure at the respective electron temperature.

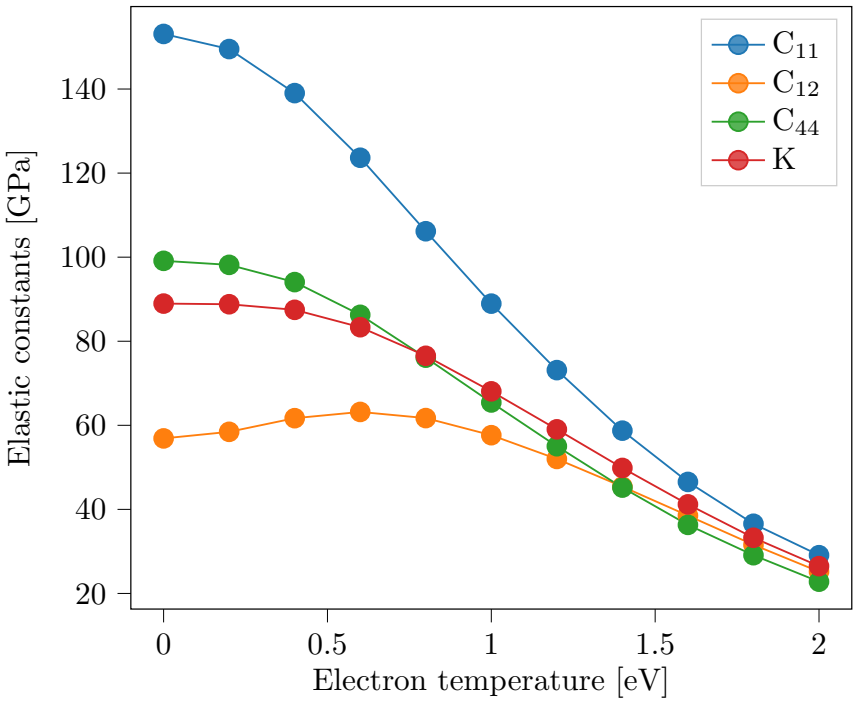

Figure 5.14: Elastic constants and bulk modulus K of Si depending on the electron temperature based on the relaxed structure at the respective electron temperature.

In figure 5.15, figure 5.16 and figure 5.17, the elastic constants are shown for Al, Cu and Si based on the relaxed structure at $T_c = 0$.
In silicon, we expect the second of Born's stability criteria to be broken at temperatures not far above $k_B T_c = 2\,\text{eV}$ from previous investigations [41, 1]. As shown in figure 5.17, C_{11} and C_{44} show a similar behaviour to when the structure is free to relax. C_{12} on the other hand increases monotonously. Especially since C_{11} and C_{12} approach each other at higher electron temperatures, we expect the lattice to become completely unstable just above $k_B T_c = 2\,\text{eV}$.
The elastic constants of aluminium, shown in figure 5.15, on the other hand shows a non-monotonous behaviour. Both C_{11} and C_{44} initially decrease, then slowly increase. C_{44} has a somewhat inverted behaviour, increasing quickly at first, then staying mostly flat. Due to the inverse behaviour of C_{11} and C_{12}, the bulk modulus stays mostly constants with a small increase at higher electron temperatures. Applying Born's stability criteria (2.18) again, we expect the stability to increase slightly since $C_{11} - C_{12}$ increases slightly and C_{44} increases after the initial decrease.
The elastic constants of copper, shown in figure 5.13, again behave differently to the other materials. C_{11} and C_{44} first decrease, then increase noticeably, while C_{12} stays more or less constant. Due to the much stronger increase of C_{11} compared to the decrease of C_{12}, the bulk modulus increase after a small dip at around $k_B T_c = 0.4\,\text{eV}$.

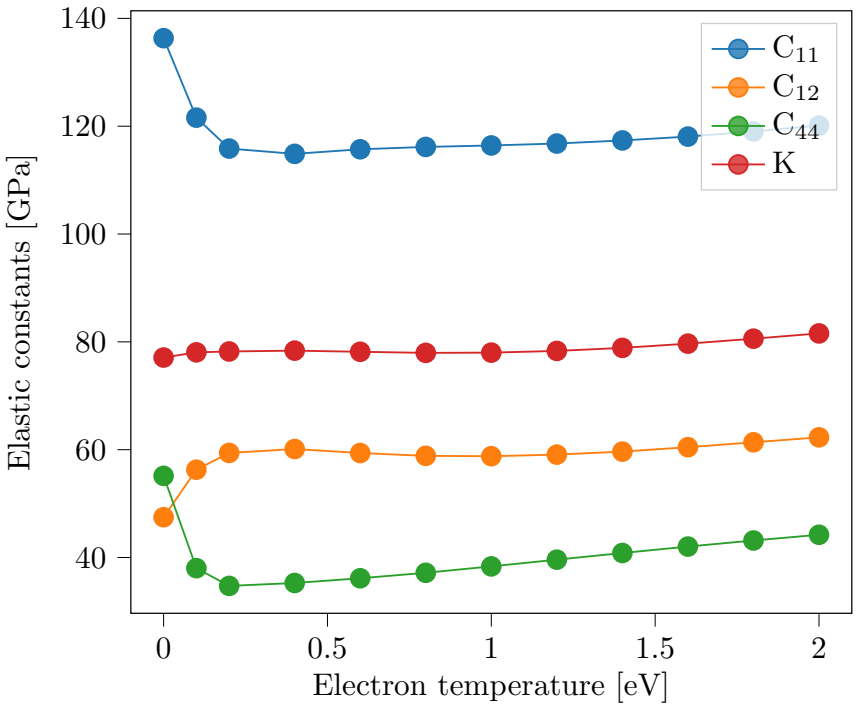

Figure 5.15: Elastic constants and bulk modulus K of Al depending on the electron temperature based on the unexcited structure.

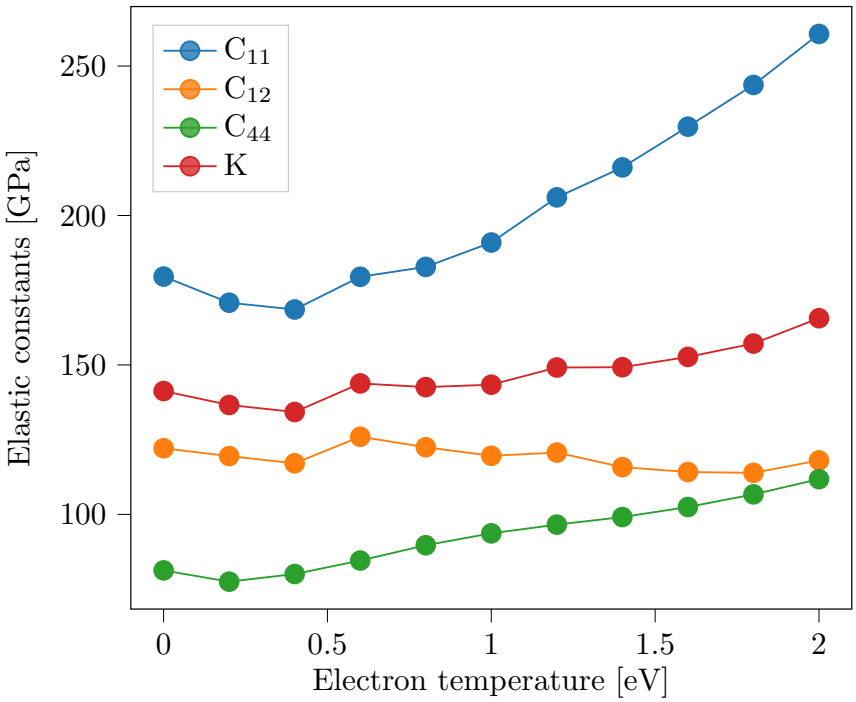

Figure 5.16: Elastic constants and bulk modulus K of Cu depending on the electron temperature based on the unexcited structure.

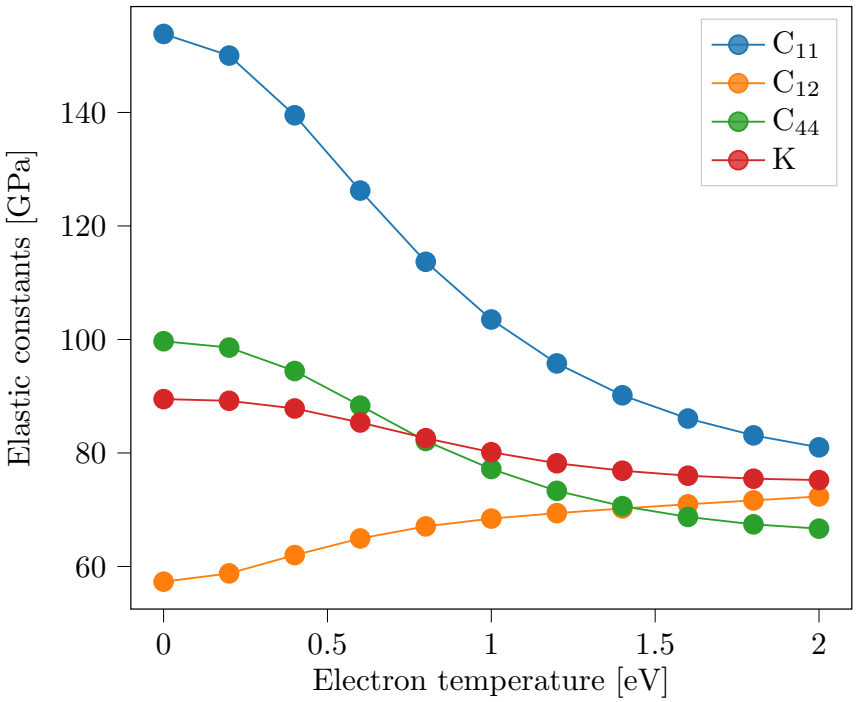

Figure 5.17: Elastic constants and bulk modulus K of Si depending on the electron temperature based on the unexcited structure.

5.3.3 Phonon spectra of excited Al and Cu

Next, in order to confirm the stability changes under excitation and to get a prediction of the melting dynamics under laser irradiation, we calculate phonon spectra of aluminium and copper and compare them to the semiconductor silicon. For these calculations we increased the accuracy by using a 9x9x9 k space grid and a cutoff energy of $1 \cdot 10^{-6}$ eV since these calculations rely on small energy differences and we found the previously used parameters to yield incorrect results.
The calculated phonon spectra are shown in figure 5.18 for aluminium, in figure 5.19 for copper and in figure 5.20 for silicon. In the phonon spectra of aluminium and copper, we can see the three acoustical and no optical modes that we expected since the primitive cell of the fcc structure only contains one atom. In the phonon spectrum of silicon, on the other hand, we can see the three acoustical modes again and also three optical mode since the unit cell of the diamond structure in silicon contains two atoms.
Furthermore, all phonon spectra are qualitatively and quantitatively very well in line with other DFT calculations and experimental investigations [42, 43, 38].

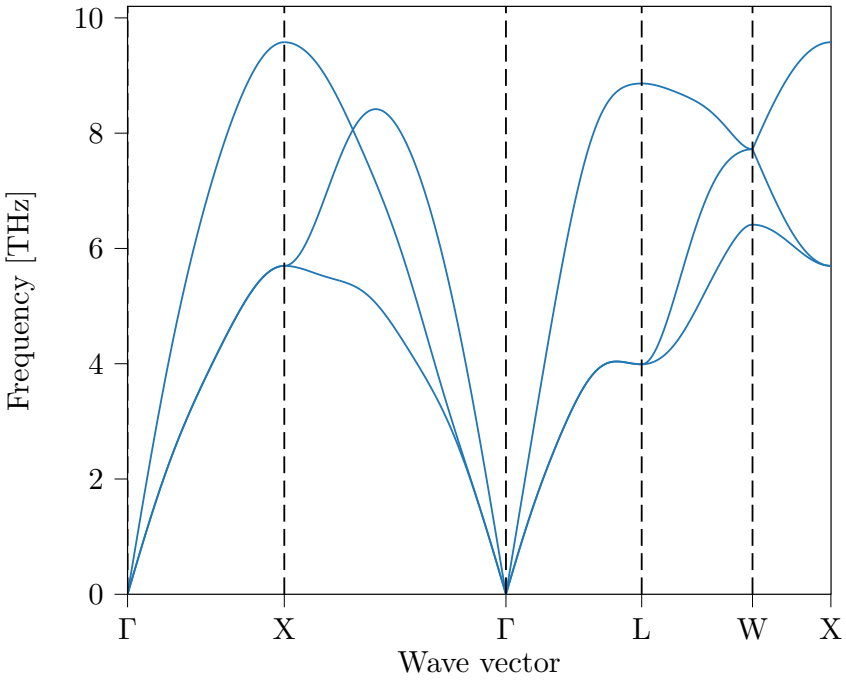

Figure 5.18: Calculated phonon spectrum of non-excited aluminium.

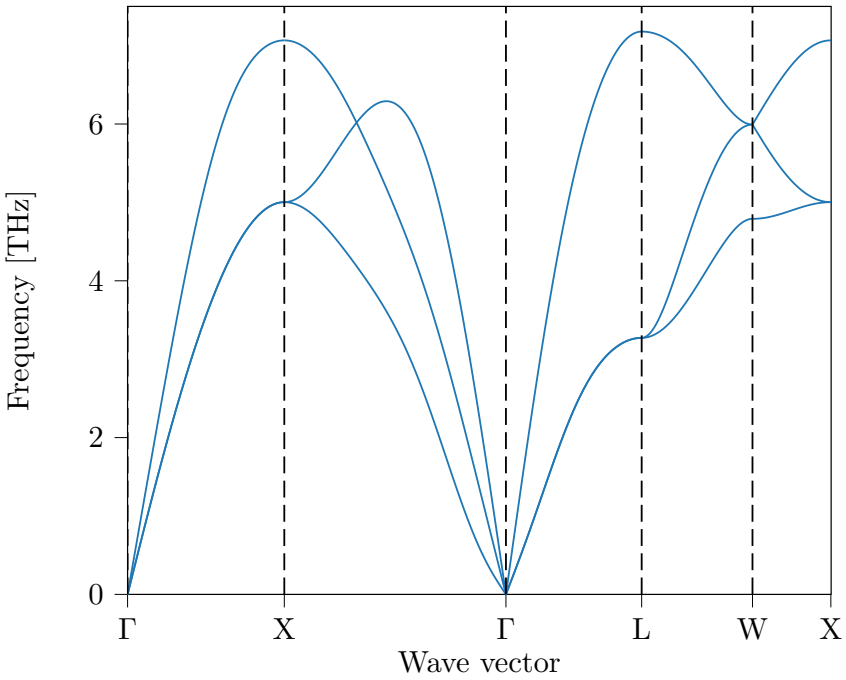

Figure 5.19: Calculated phonon spectrum of non-excited copper.

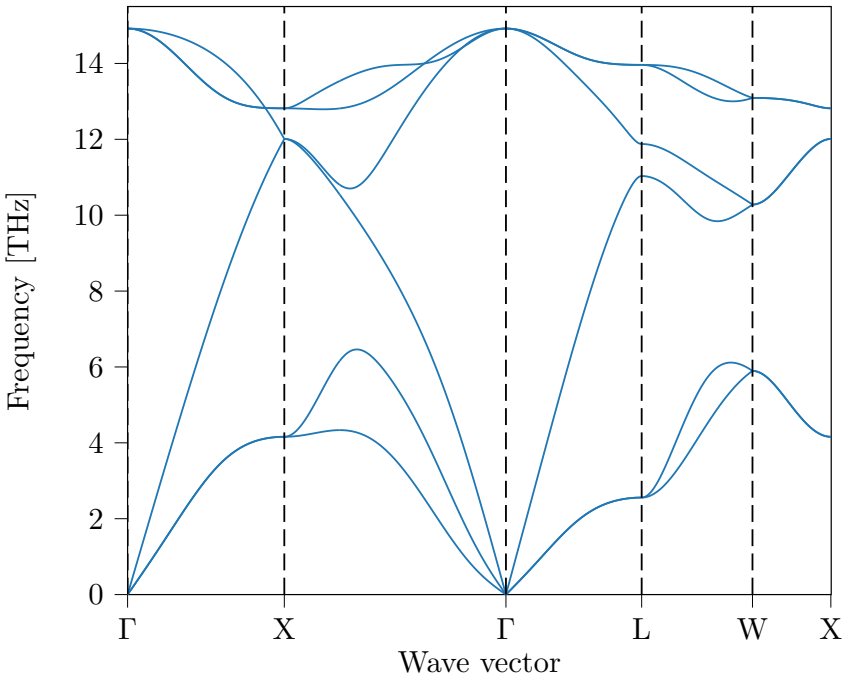

Figure 5.20: Calculated phonon spectrum of non-excited silicon.

Next, we calculate the phonon spectra at different degrees of excitation to investigate the changes in the bond strength in different materials. From the calculation of the elastic constants, we learned that the structure these calculations are based on have a big impact on the results and only the results from the relaxed structure at $T_c = 0$ are truly meaningful in the context of ultrafast laser ablation. We therefore focus on the results from the $T_c = 0$ structures and only quickly comment on the results from the relaxed structures at each electron temperature afterwards.
The phonon spectra of Al, Cu and Si at different electron temperatures in the unexcited structures are shown in figure 5.21, figure 5.22 and figure 5.23. A clear difference between the metal and semiconductor phonon spectra becomes obvious. While the frequencies in aluminium stay more or less unchanged during excitation, the frequencies in copper are shifted towards higher values upon increase in electron temperature, indicating what is generally referred to as bond-hardening, that has already been observed in similar DFT calculations concerned with magnesium and gold [39, 38, 44]. In particular, we can reproduce a very similar change in the different modes in copper as was previously only seen in gold. In the semiconductor that is silicon, we see a completely different picture. Here, the frequencies are shifted to lower values with increasing electron temperature, even reaching negative, sometimes called imaginary, values. This indicates the lattice instability that is also found during laser irradiation experimentally.
We choose the modes with the highest frequencies at the symmetry points L and X and plot these frequencies over the electron temperature in figure 5.24 for aluminium, in figure 5.25 for copper and in figure 5.26 respectively for silicon. Note that the change in

bond strength can be seen in the highest frequency at X in an fcc structure and at L in a diamond structure.

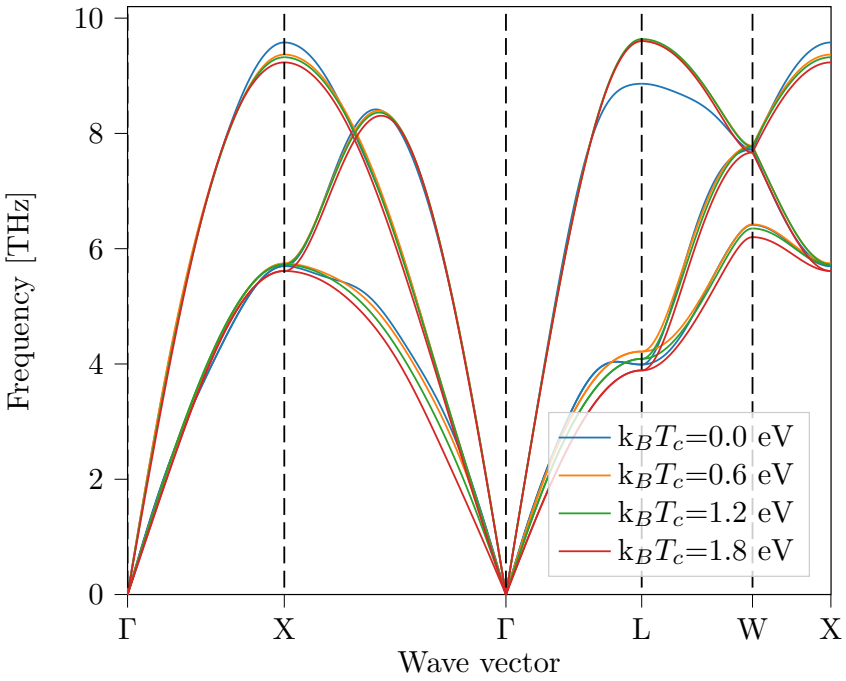

Figure 5.21: Calculated phonon spectrum of aluminium at different electron temperatures T_c in the relaxed $T_c = 0$ structure.

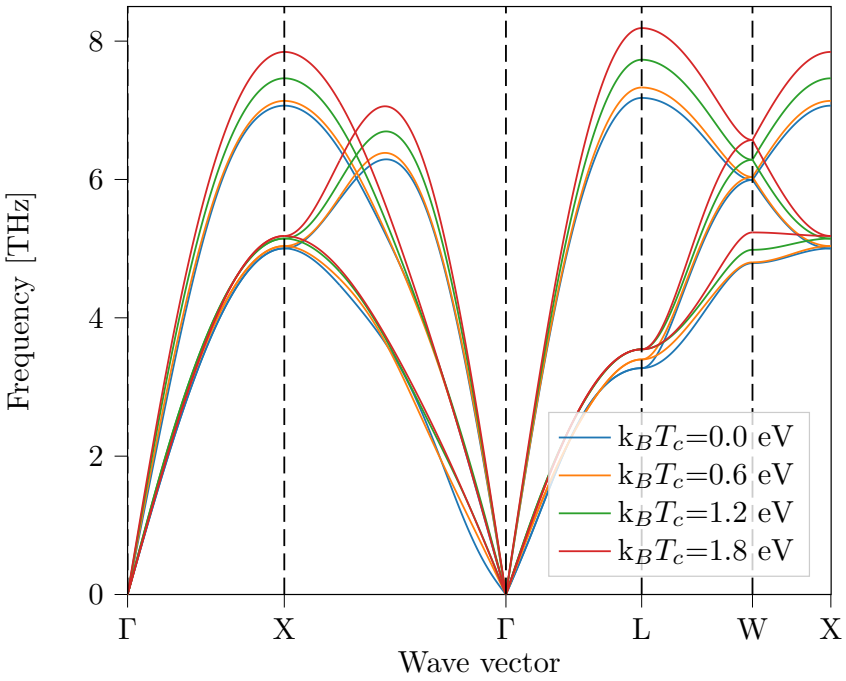

Figure 5.22: Calculated phonon spectrum of copper at different electron temperatures T_c in the relaxed $T_c = 0$ structure.

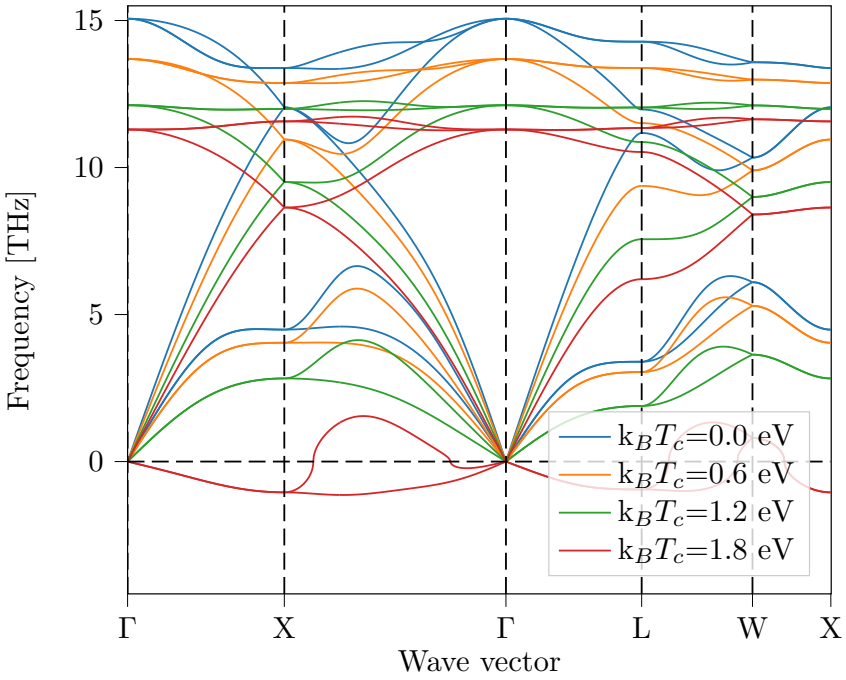

Figure 5.23: Calculated phonon spectrum of silicon at different electron temperatures T_c in the relaxed $T_c = 0$ structure.

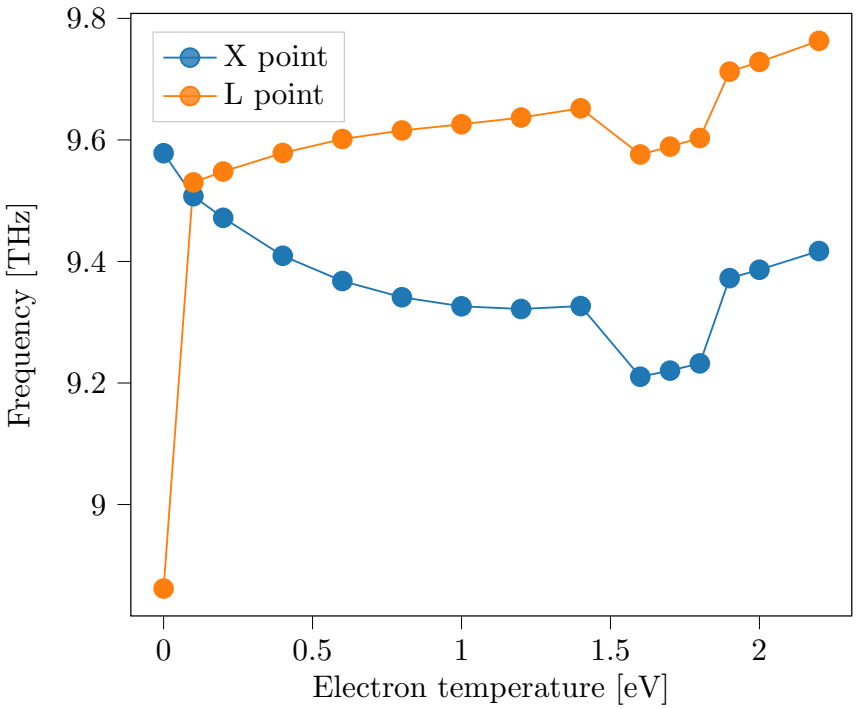

Figure 5.24: Phonon frequency of the mode at X and L depending on the electron temperature in aluminium in the relaxed in the relaxed $T_c = 0$ structure.

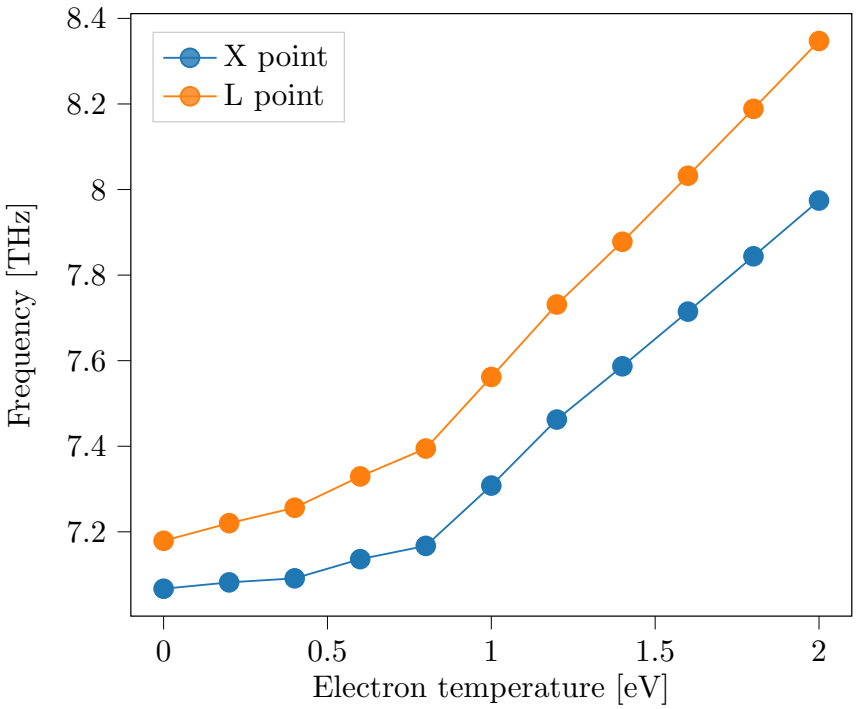

Figure 5.25: Phonon frequency of the mode at X and L depending on the electron temperature in copper in the relaxed $T_c = 0$ structure.

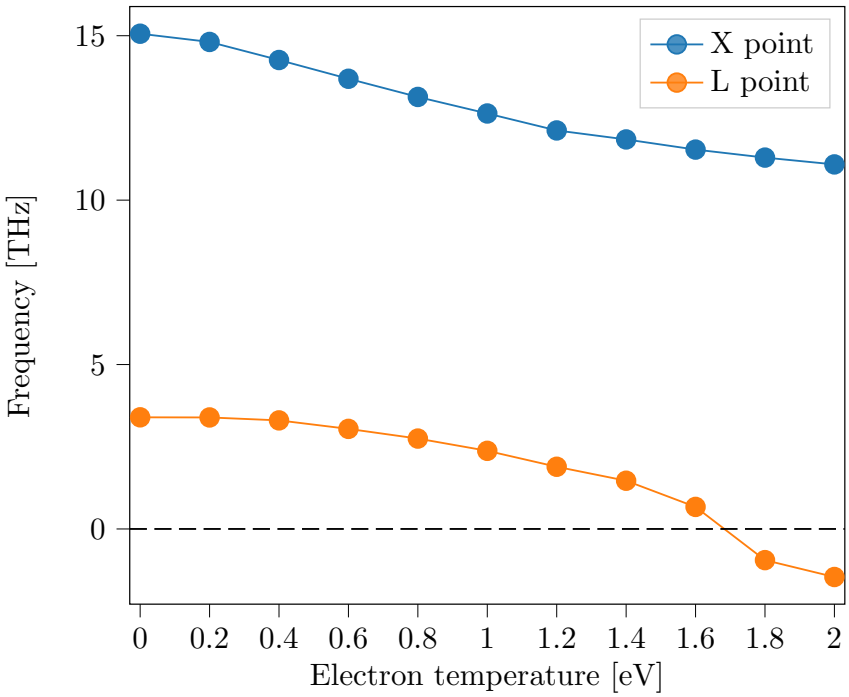

Figure 5.26: Phonon frequency of the mode at X and L depending on the electron temperature in silicon in the relaxed $T_c = 0$ structure.

Very similar to the elastic constants, the high-temperature behaviour of the phonon spectra is very different in the relaxed structure at each electron temperature. As did the elastic constants in aluminium, copper and silicon, the frequencies both at X and L decrease with the temperature due to the expansion and the vanishing pressure in the simulation box. The bond-softening in silicon is thus still present but far less prominent than in the case of the fixed box size. Now, we encounter no negative frequencies and thus no complete lattice instability. This means that silicon is more stable during strong excitations in its relaxed structure than it is in the unexcited structure. On the other hand, aluminium and copper are less stable in the relaxed structures than they are in the unexcited structures.

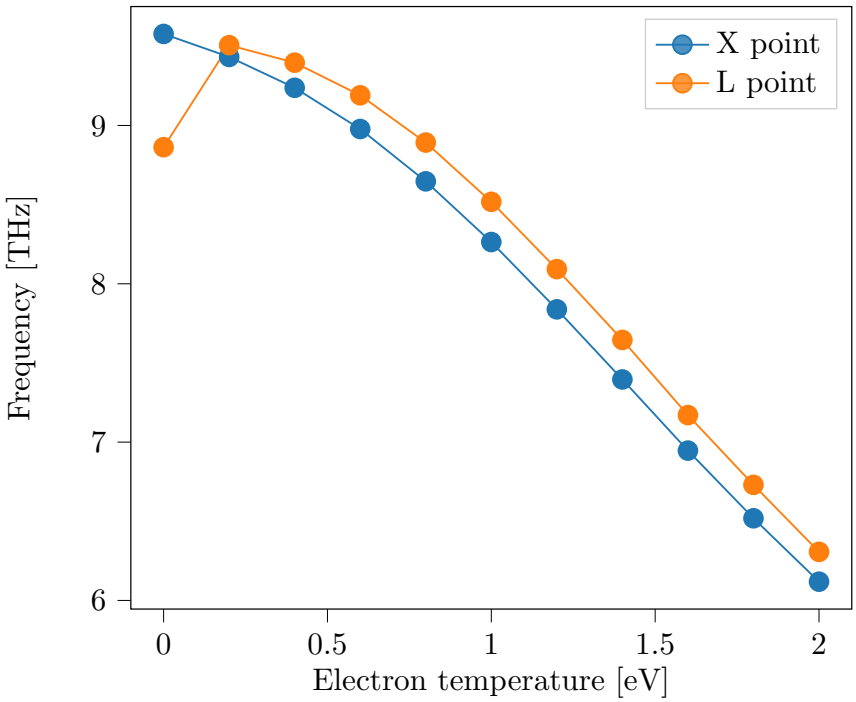

Figure 5.27: Phonon frequency of the mode at X and L depending on the electron temperature in aluminium in the relaxed structure of each electron temperature.

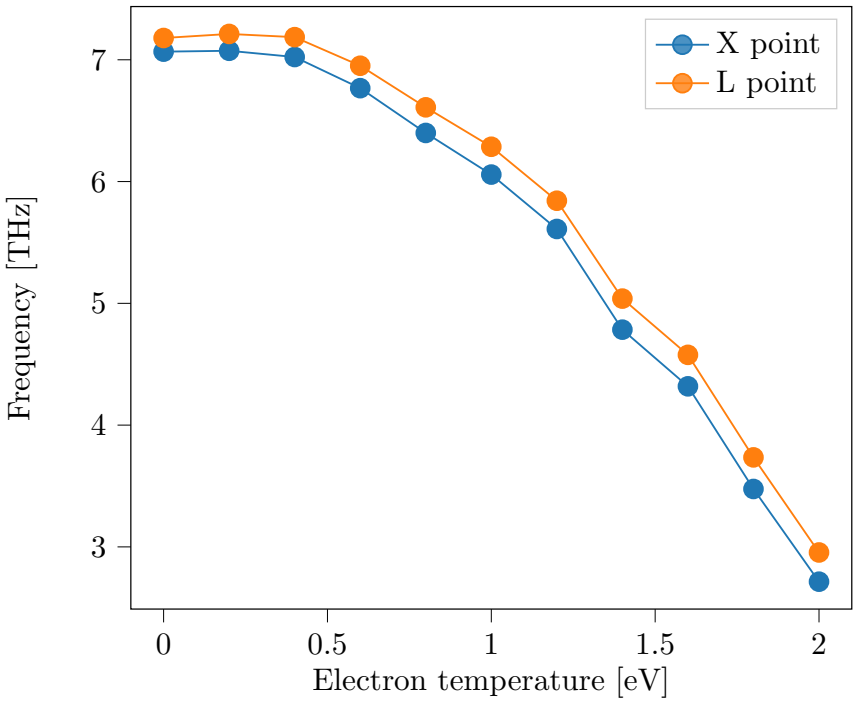

Figure 5.28: Phonon frequency of the mode at X and L depending on the electron temperature in copper in the relaxed structure of each electron temperature.

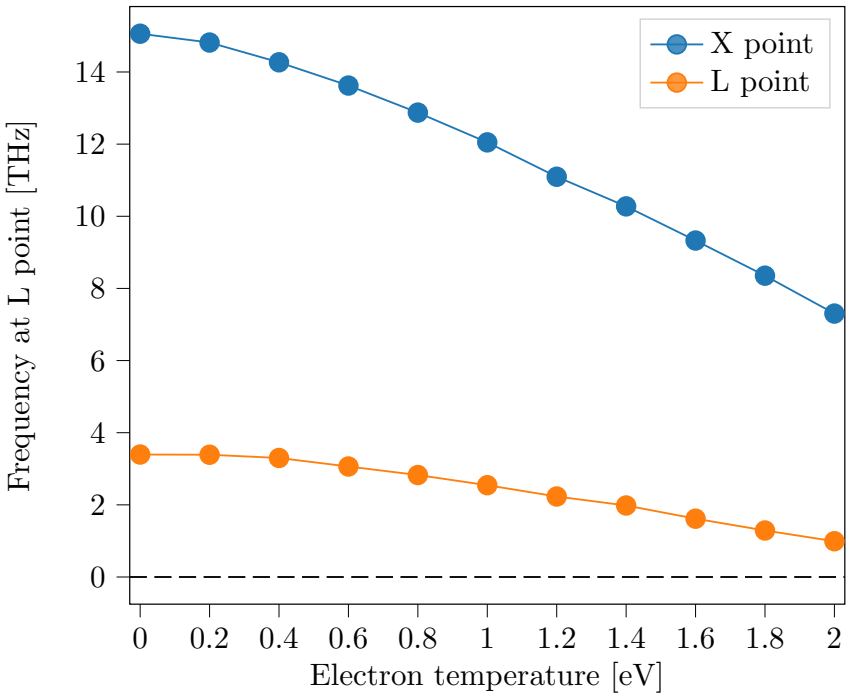

Figure 5.29: Phonon frequency of the mode at X and L depending on the electron temperature in silicon in the relaxed structure of each electron temperature.

5.3.4 Density of states of excited Al and Cu

We begin this section by displaying the DOS of non-excited aluminium and copper. It is important to note here that VASP doesn't write a usable DOS for electron temperatures below a certain temperature. We don't know the reason for this behaviour since the integrated DOS

$$N(E) = \int_{-\infty}^{E} D(\tilde{E})\,\mathrm{d}\tilde{E} \tag{5.4}$$

is output without any problems. We tried reproducing the DOS from the integrated DOS but due to the limited decimal places of the DOS output which - as far as we know - cannot be adjusted without access to the source code, the DOS was not usable for further calculations. We also don't know the limit for this phenomenon but found $k_B T_c = 0.01\,\mathrm{eV}$ to work fine. This issue doesn't appear again at higher electron temperatures. Since $k_B T_c = 0.01\,\mathrm{eV}$ is still very low compared to the next larger value, we assume that the DOS and properties calculated with it are not effected by this. Furthermore, we should also note that we again increased the accuracy of the calculations. We use the convergence criterion $\Delta E_{\mathrm{conv}} = 1 \cdot 10^{-4}\,\mathrm{eV}$ and a k-space grid of 31x31x31 points. Sampling the k-space grid accurately is very important for these kinds of calculations since non-physical fluctuations decrease with increasing density of the k-space grid. For all DOS calculations, we also use smaller systems only consisting of only two unit cells.

We start by calculating the DOS of unexcited aluminium which is an attractive starting point since we can compare it to the one of a free electron gas. Details on the theoretical DOS can be found in appendix B. As derived there, the DOS $D(E)$ at energy E of a free electron gas in the volume Ω is given by

$$D(E) = \frac{\Omega}{2\pi^2}\left(\frac{2m}{\hbar^2}\right)^{3/2}\sqrt{E}. \tag{5.5}$$

As shown in figure 5.30, the DOS of aluminium obtained using VASP is in great accordance to the square root-like DOS of a free electron gas which is expected to be a valid approximation for aluminium. On the other hand, the DOS of copper shown in figure 5.31 cannot be compared to the free electron gas. This is due to the d-electrons that aluminium doesn't have.
The DOS of both aluminium and copper directly from the VASP output contained unphysical fluctuations. In order to handle these fluctuations while making the physically relevant details visible, we average the data. Originally written with 3001 DOS data points, we average 51 in aluminium and only 9 in copper. There's a difference between the number of data points that are averaged since we saw stronger fluctuations in aluminium than in copper and we couldn't average over more data points in copper due to its narrower peaks in the DOS. The standard deviations arising from the averaging are also shown in the DOS plots of non-excited aluminium figure 5.30 and copper figure 5.31.

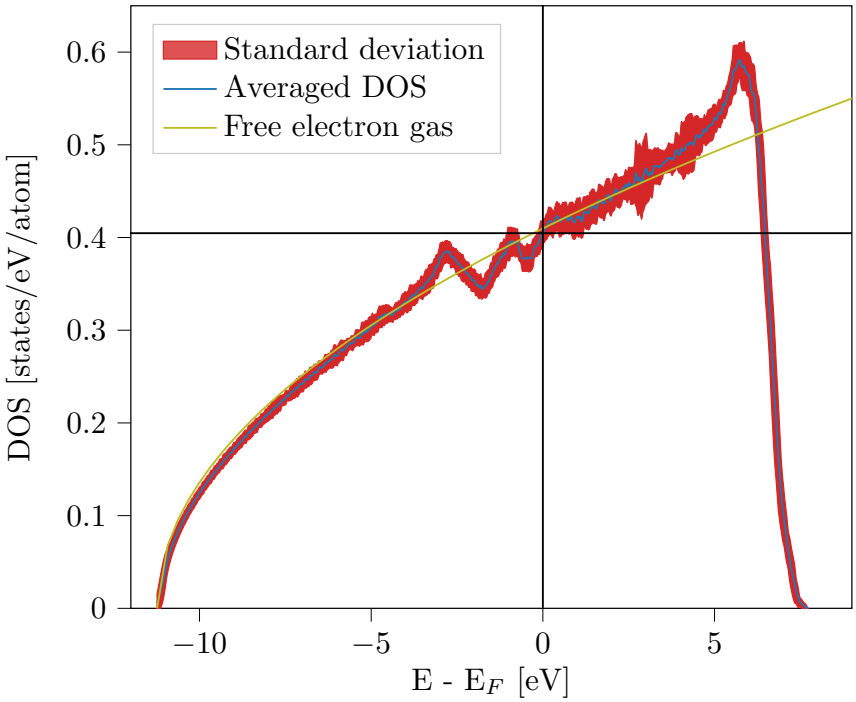

Figure 5.30: Calculated density of states and its standard deviation of non-excited aluminium with a fit to the free electron gas (5.5).

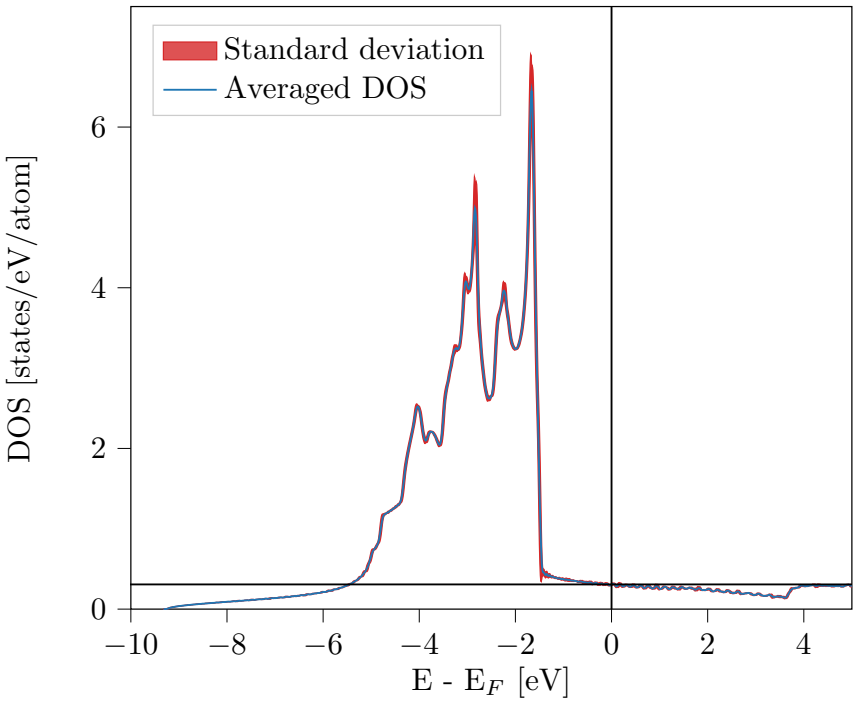

Figure 5.31: Calculated density of states and its standard deviation of non-excited copper.

The Fermi energy and the DOS at the Fermi energy are indicated in figure 5.30 and figure 5.31 by black lines. These values are given in table 5.5. Even though both DOS look similar to other DFT investigations [45], we clearly lack a lot of detail but couldn't find a set of parameters that resulted in a more detailed DOS. Averaging our data clearly has an impact on the level of detail we can achieve. Without it, however, we have clearly unphysical oscillations in our DOS that are distinctly different to those from the DFT calculations presented in [45].
According to the Sommerfeld model, the degeneracy pressure is proportional to the DOS at the Fermi energy, to be exact

$$p = \frac{2}{5}\frac{N}{\Omega}E_\mathrm{F} + \frac{\pi^2}{18}(\mathrm{k_B}T_c)^2 D(E_\mathrm{F}). \tag{5.6}$$

This expression was derived in appendix B. Revisiting the pressure in the unexcited structures shown in figure 5.11, we unfortunately cannot exactly reproduce this behaviour. While at low temperatures, where the Sommerfeld model is more accurate, the pressure follows a more or less quadratic curve, the pressure becomes rather linear with electron temperature at higher electron temperatures. This discrepancy could potentially stem from higher-order contributions to the Sommerfeld expansion that we left out. However, what's most different between the Sommerfeld model and our calculations is the fact that copper shows higher pressures in the unexcited structure compared to aluminium even though aluminium has a higher DOS at the Fermi energy than copper. Since we aren't completely satisfied with our DOS, it might be the cause of the DOS at the Fermi energy and thus

the pressures according to the Sommerfeld model to show a different behaviour than what we expected.

Together with the electron temperature-dependent DOS of aluminium in figure 5.32 and of copper in figure 5.33, these values will be used to calculate the temperature-dependence of the chemical potential. Note again that the derivation of the chemical potential and other thermodynamic properties are given in appendix B. To no surprise, the electron temperature-dependent DOS become smoother at very low and very high energies due to the smearing of the states. Also, as a consequence of the partial occupancies from the smearing, we loose a lot of detail in the electronic structure. This is the main reason why we can't calculate thermodynamic properties besides the chemical potential with great accuracy and will leave them out here. Since the number of electrons still has to remain the same at higher temperatures, the chemical potential can still be obtained with good accuracy.

Table 5.5: Fermi energy and DOS at the Fermi energy in non-excited aluminium and copper.

System	E_F [eV]	$D(E_F)$ [states/eV/atom]
Al	8.021	0.402
Cu	7.394	0.307

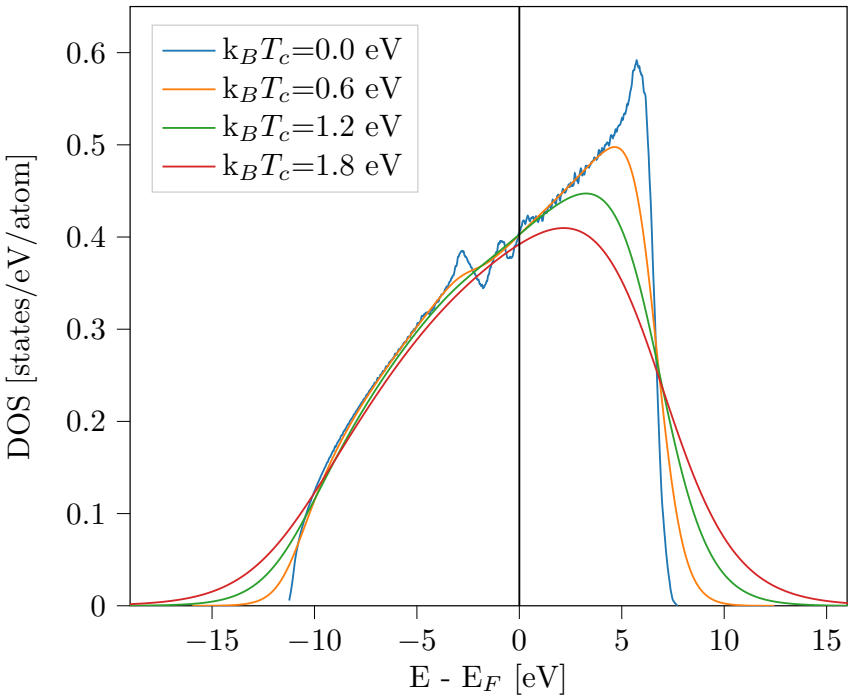

Figure 5.32: Calculated DOS of aluminium at different electron temperatures.

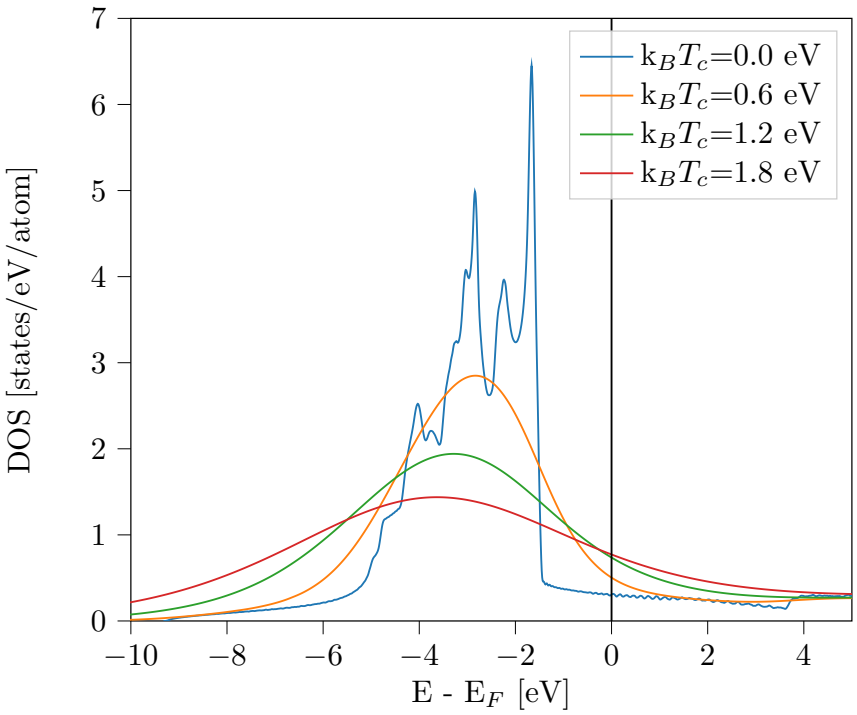

Figure 5.33: Calculated DOS of copper at different electron temperatures.

The chemical potential within the Sommerfeld expansion is given by

$$\mu = E_{\mathrm{F}}\left[1 - \frac{\pi^2}{12}\left(\frac{\mathrm{k_B}T_c}{E_{\mathrm{F}}}\right)^2\right] \tag{5.7}$$

and is automatically calculated by VASP from the conservation of electrons. Results from the Sommerfeld expansion and our VASP calculations are shown in figure 5.34 for aluminium and in figure 5.35 for copper. To no surprise, the Sommerfeld model predicts the change in chemical potential of aluminium very well at lower temperatures and with small deviations at high temperatures. Since the Sommerfeld model in our case only takes terms up to the second order in $\mathrm{k_B}T_c$ into account and is therefore a low-temperature approximation, this deviation seems reasonable. In fact, the DOS at $T_c = 0$ has been used in other DFT investigations [45] with different Fermi smearings without the need of high-temperature DFT calculations and found the same electron temperature-dependence of the chemical potential.
In copper we see a different behaviour. While the Sommerfeld model might make correct predictions at very low temperatures, it completely fails above $\mathrm{k_B}T_c = 0.2\,\mathrm{eV}$ since the chemical potential increases with T_c.

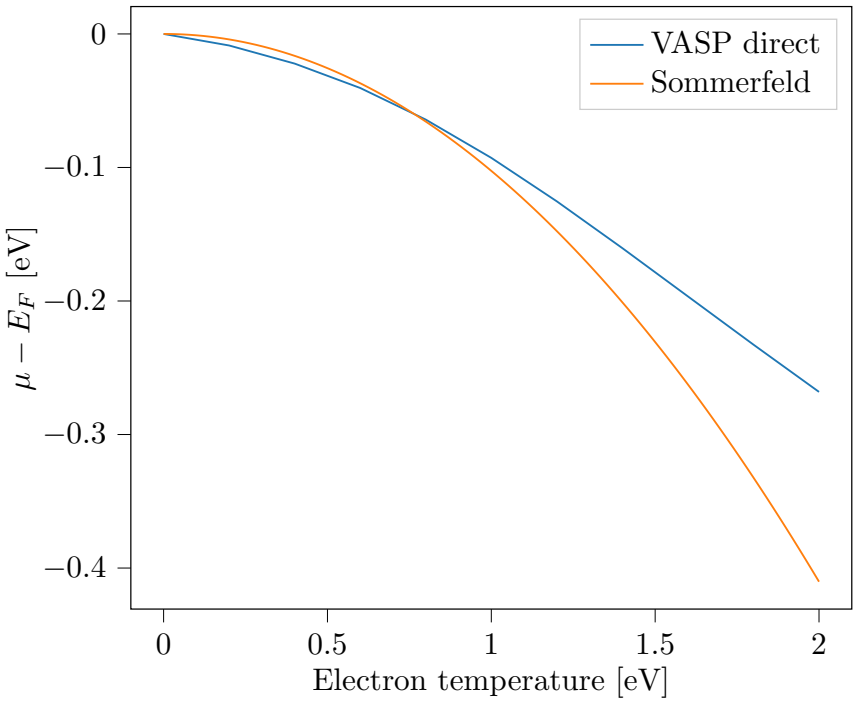

Figure 5.34: Chemical potential of aluminium depending on the electron temperature calculated directly from the conservation of electrons with a comparison to the Sommerfeld model prediction.

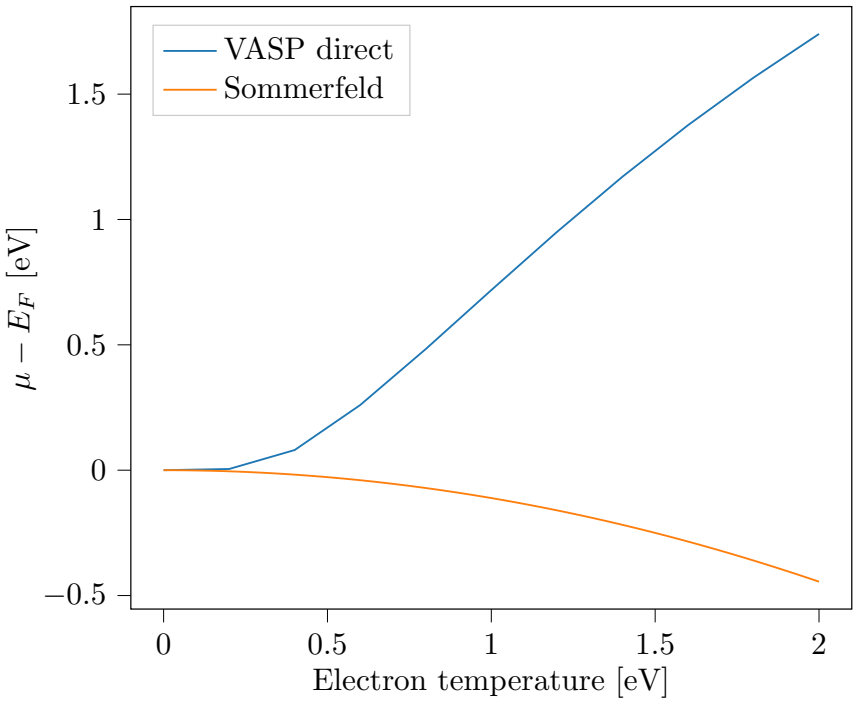

Figure 5.35: Chemical potential of aluminium depending on the electron temperature calculated directly from the conservation of electrons with a comparison to the Sommerfeld model prediction.

We can understand both changes in the chemical potential remembering the conservation of electrons. In aluminium, the DOS increases monotonously. Therefore, with increasing temperature, the Fermi smearing allows for occupation of higher energy regions with a higher DOS. To keep the number of electrons constant, the chemical potential then has to be shifted towards lower energies. In copper on the other hand, the d-electrons below the Fermi energy have a very high DOS. With increasing smearing, more d-electrons are excited to energy regions with lower DOS. To keep the number of electrons constant in this case, the chemical potential has to be shifted towards higher energies.

We tried calculating other properties like the internal energy. However, we found the quality of our electron temperature-dependent DOS insufficient for these properties and need more time to investigate the issues that arose. Since we could reproduce the behaviour of the chemical potential that was also shown in the only work we found addressing the electron temperature-dependence of thermodynamic properties from the DOS [45] without the need for actual temperature-dependent DOS, this might not even be worth looking into.

5.4 Properties of excited Al-Cu alloys

In this chapter, we extend our analysis to Al-Cu alloys and perform analogous calculations to the ones we did for pure aluminium and copper. Similarly to the pure metals, we start by looking at the thermodynamic properties of the alloys, calculating the relaxed structure at different electron temperatures and the respective internal and free energies, as well as the pressure in the ground state structure. Then, we calculate the elastic constants and phonon spectra and conclude this chapter with the DOS. While we calculate the thermodynamic properties in all four alloy structures we introduced earlier, that being GPI, GPII, θ and θ', we only consider the θ' structure when calculating the elastic constants, phonon spectra and DOS. The reason for this is that GPI and GPII aren't truly stable structures that we only took into account in this work since they are in the range of copper percentage we're interested in and because of their importance in the formation of more stable Al-Cu alloy structures. The θ structure on the other hand is not taken into account for the latter three types of calculations since it's entropically stabilised at temperatures far above room temperature. In [35], it is stated that the θ structure is only stable at temperatures of 150 °C to 200 °C. In the context of ultrafast laser excitation, we assume that the lattice is heated fast enough so that the phase transition from one solid structure to the other does not occur and instead the lattice melts due to the electron-phonon coupling.

5.4.1 Thermodynamic properties of excited Al-Cu alloys

We start the investigation of the Al-Cu alloys with thermodynamic properties. We calculate the relaxed structures and their internal and free energy. In figure 5.36, the volume per atom is depicted depending on the temperature. As can be seen there, all three structures expand very similarly to the pure metals. This expansion is greater in the more stable θ and θ' structures than in the GPI and GPII structure. Next, the internal energy per atom depending on the electron temperature is displayed in figure 5.37. The absolute value of the internal energy decreases due to the increasing distance between the atoms and therefore decreasing binding energy.

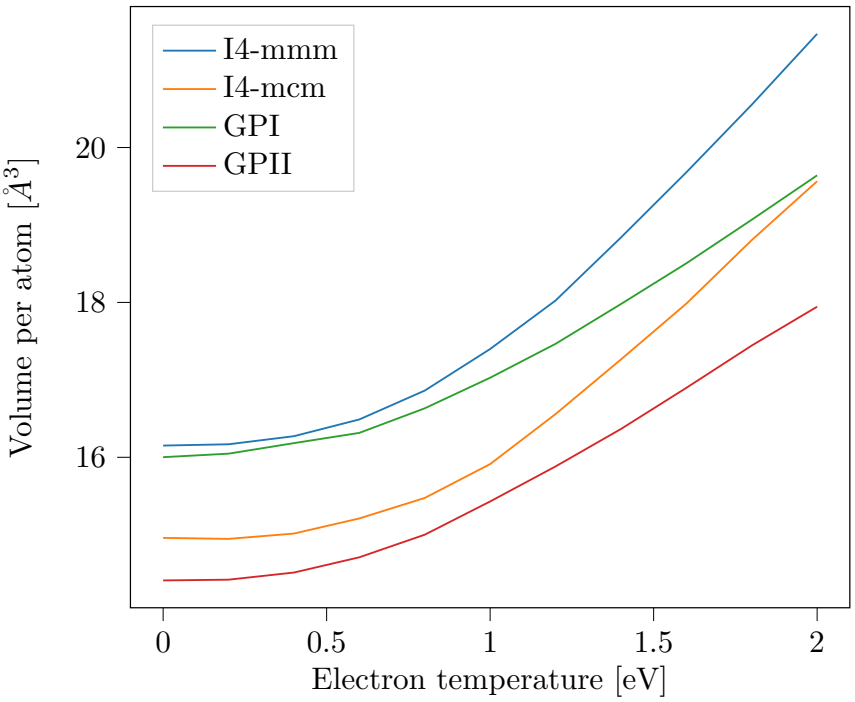

Figure 5.36: Volume per atom of different Al-Cu alloy structures depending on the electron temperature.

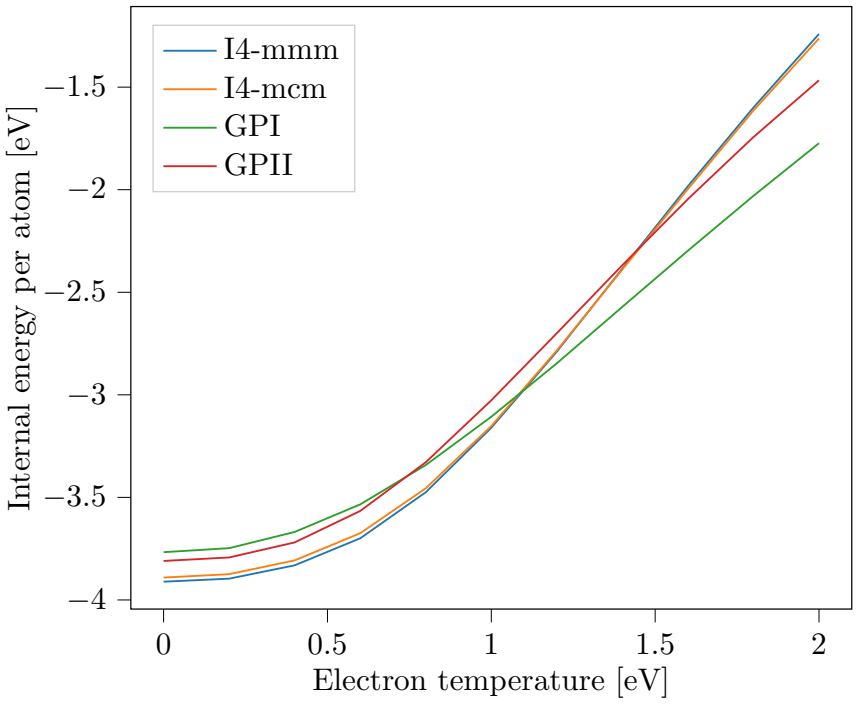

Figure 5.37: Internal energy per atom of different Al-Cu alloy structures depending on the electron temperature.

Finally, the free energy per atom of all four structures depending on the electron temperature is shown in figure 5.38. As for the pure metals, the free energy decreases due to the increasing contribution of the electronic entropy to the free energy. We can also see that for electron temperatures above $k_B T_c = 0.6\,\text{eV}$, the θ structure has a lower free energy than the θ' structure. This confirms the assumption about the entropic stabilization of the θ structure that we made earlier. In a proper laser ablation simulation, we will however most likely not see a phase transition from the θ structure to the θ' structure since the heating due to the electron-phonon coupling will probably lead to melting of the structure before such a solid-to-solid phase transition could take place.

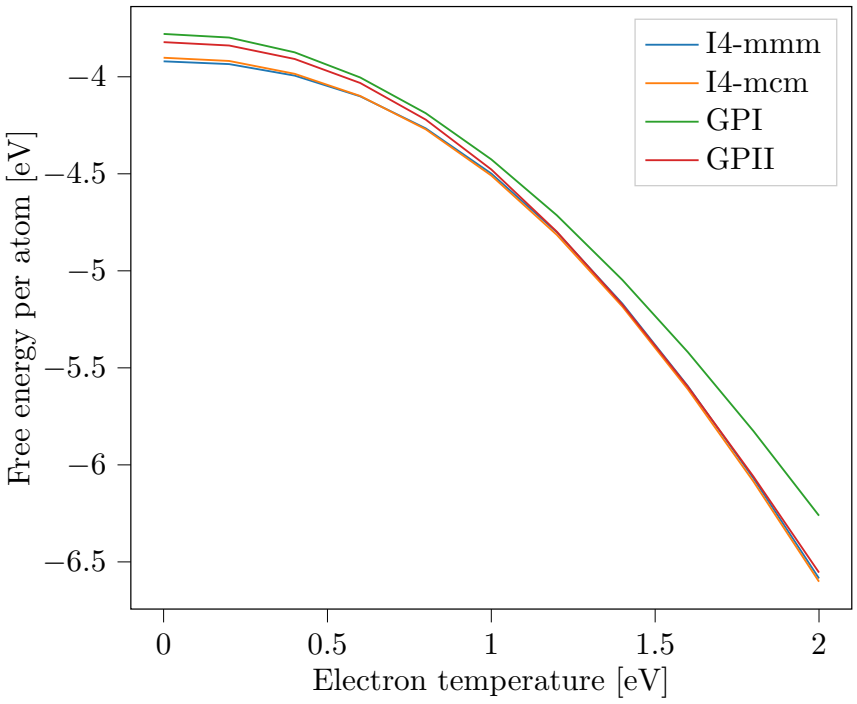

Figure 5.38: Internal energy per atom of different Al-Cu alloy structures depending on the electron temperature.

In figure 5.39, the pressure in the unexcited structure is shown depending on the electron temperature. The pressures increase with the electron temperature in all three structures which will eventually lead to the expansion of the structure if it is allowed to do so. The only exception to this is the GPII structure which exhibits a small dip a low temperatures. Interestingly, this dip can't be seen in the volume of the structure. One cause of this could be the convergence criterion for the atoms. In that case, the ionic convergence criterion is reached even though the net force within the simulation box is not zero. Another explanation could be a non-uniform expansion of the structure since it's non-cubic. This can be investigated for both the GPI and GPII structure since both are non-cubic. We therefore calculate the relative 1D-expansion, shown in figure 5.40. It becomes obvious that both the GPI and GPII structure expand in x- and y-direction and contract in z-direction with increasing electron temperature. This effect is much more prominent in the GPII structure which leads to the negative pressure in the unexcited structure. In the GPI structure, however, the expansion in x- and y-direction compensate the contraction in z-direction so that the pressure increases monotonously with electron temperature.

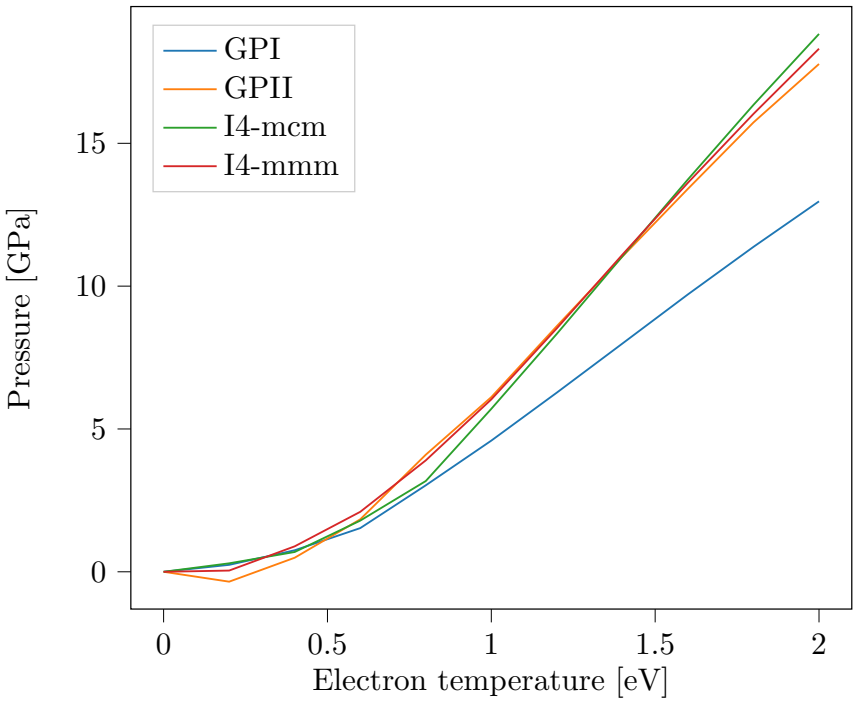

Figure 5.39: Pressure in the unexcited structure at depending on the electron temperature in the four Al-Cu alloys structures.

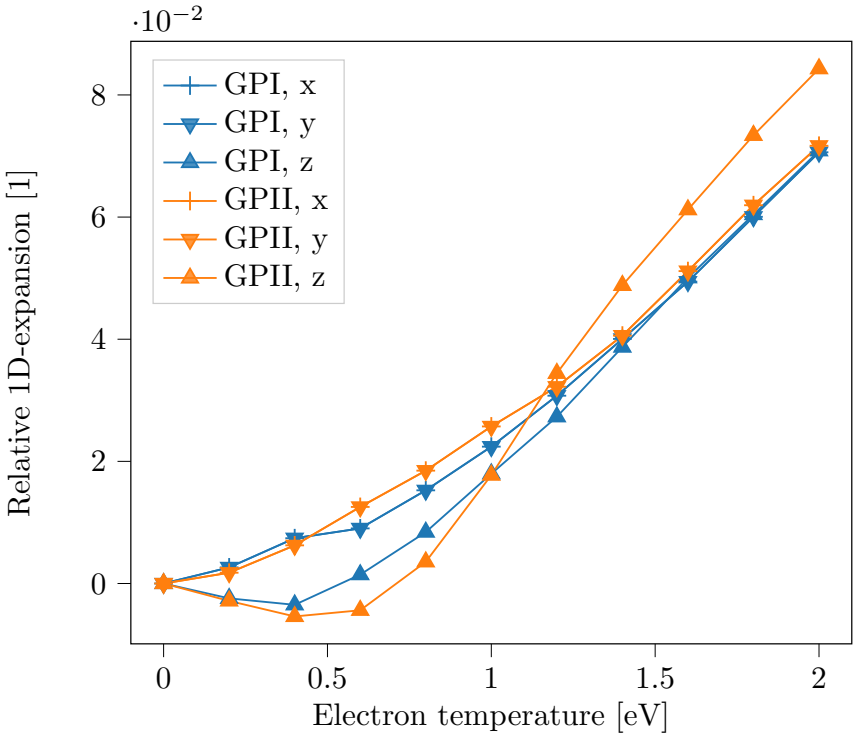

Figure 5.40: Relative expansion of the GPI and GPII structure of the Al-Cu alloys in x-, y- and z-direction depending on the electron temperature

5.4.2 Elastic constants of excited Al-Cu alloys

We now calculate the elastic constants and bulk modulus of the θ' structure of the Al-Cu alloys. The elastic constants and the bulk modulus are displayed in figure 5.41 depending on the electron temperature and based on the unexcited structure. Except for the values between $k_B T_c = 0.2\,eV$ and $k_B T_c = 0.8\,eV$, we have a similar behaviour as copper. At first, C_{11} and C_{12} decrease while C_{44} almost decreases monotonously. Since C_{11} and C_{12} behave very similarly, the bulk modulus K behaves just the same. Applying Born's stability criteria (2.18) here, it is rather difficult to make a concrete prediction on the stability of the θ' structure. While both C_{11} and C_{12} increase at higher electron temperatures, C_{11} always is larger than C_{12}, indicating stability, C_{44} decreases indicating that the third criterion might be violated at even higher electron temperatures leading to a lattice instability. Since the θ' structure isn't the most stable structure at high electron temperatures, repeating the calculations of the elastic constants but with the θ structure might confirm the stabilisation of the θ structure by electronic entropy.

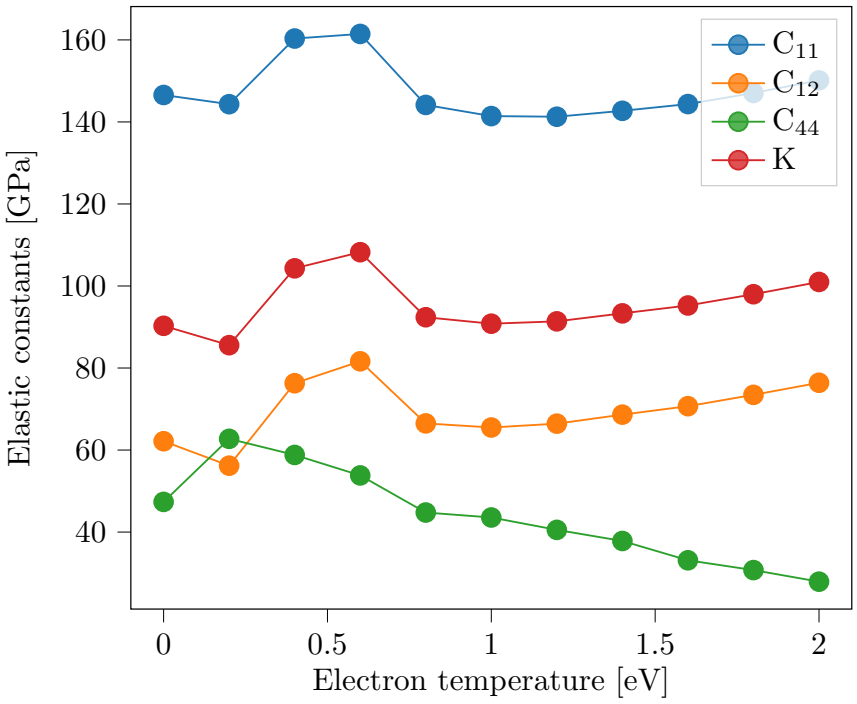

Figure 5.41: Elastic constants and bulk modulus of the θ' structure of the Al-Cu alloys based on the unexcited structure.

5.4.3 Phonon spectra of excited Al-Cu alloys

In this chapter, we will present the phonon spectra of the θ' structure of the Al-Cu alloys to further analyse their bond strength. We only show these spectra in the unexcited structure at different electron temperatures due to the reasons discussed when we calculated the phonon spectra in pure metals in section 5.3.
In figure 5.42, the phonon spectrum of the alloys is shown at $T_c = 0$. To no surprise, we can see three acoustical branches and six optical branches since the primitive cell contains three atoms. We also show the phonon spectrum at four different electron temperatures in figure 5.43. Due to the greater amount of modes, it is rather difficult to see all differences. We therefore also show the frequencies of the mode with the highest frequency at X and L in figure 5.44. As can be seen there, the frequencies at both X and L increase almost completely monotonously indicating bond-hardening. The bond-hardening is determined by the highest frequency at X.

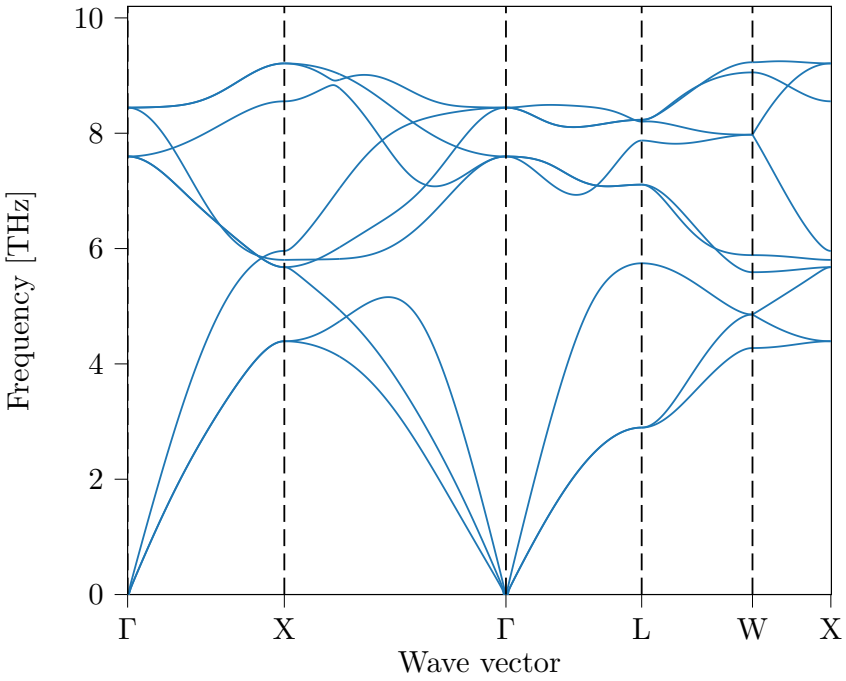

Figure 5.42: Calculated phonon spectrum of the unexcited θ' structure of the Al-Cu alloys.

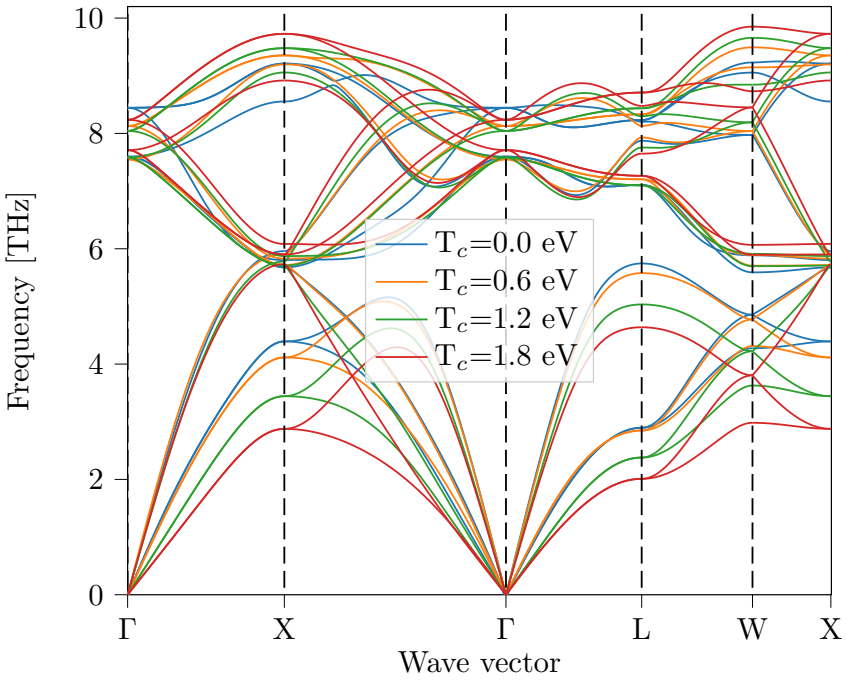

Figure 5.43: Calculated phonon spectrum of the unexcited θ' structure of the Al-Cu alloys at different electron temperatures.

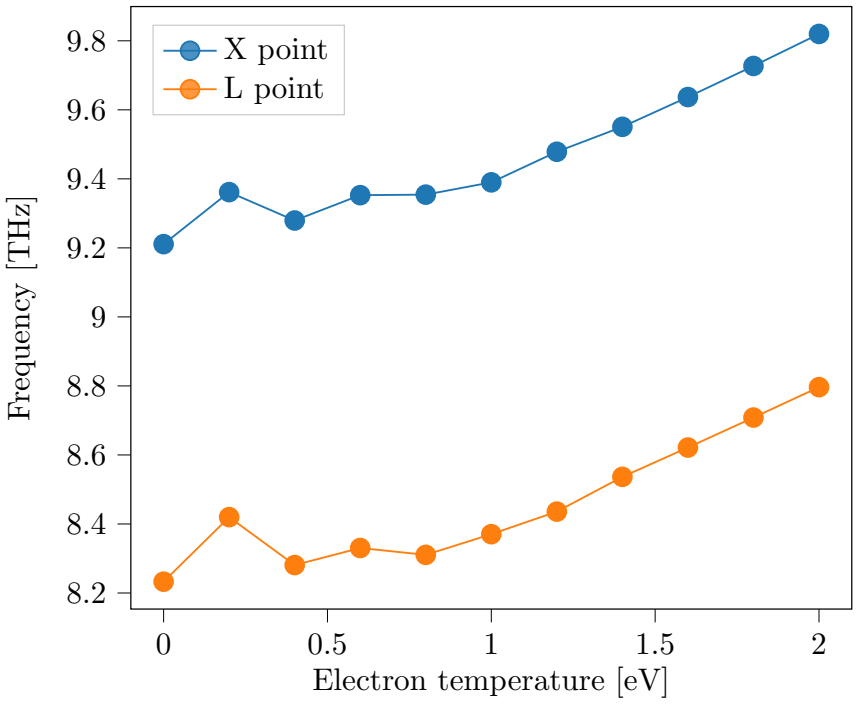

Figure 5.44: Frequencies at X and L of the unexcited θ' structure of the Al-Cu alloys depending on the electron temperature.

5.4.4 Density of states of excited Al-Cu alloys

For this chapter, we calculate the DOS of a single unit cell of the θ' structure of the Al-Cu alloys. The ground state DOS is shown in figure 5.45. We again use the convergence criterion $\Delta E_{\text{conv}} = 1.0 \cdot 10^{-4}\,\text{eV}$ and a k-space grid of 31x31x31 points. Since this DOS again contains unphysical oscillations, we average every 9 data point out of the 3001 data points output by VASP. As for the pure metals, we planned to expand our investigations by calculating the temperature-dependent DOS but ran into the same problems as with the pure metals. We still calculate the DOS at various electron temperatures as shown in figure 5.46, hoping that we can at least extract the change of the chemical potential with electron temperature which is shown in figure 5.47. Since the DOS below the Fermi energy is higher than at and above the Fermi energy, the chemical potential is shifted towards higher energies at higher electron temperatures.

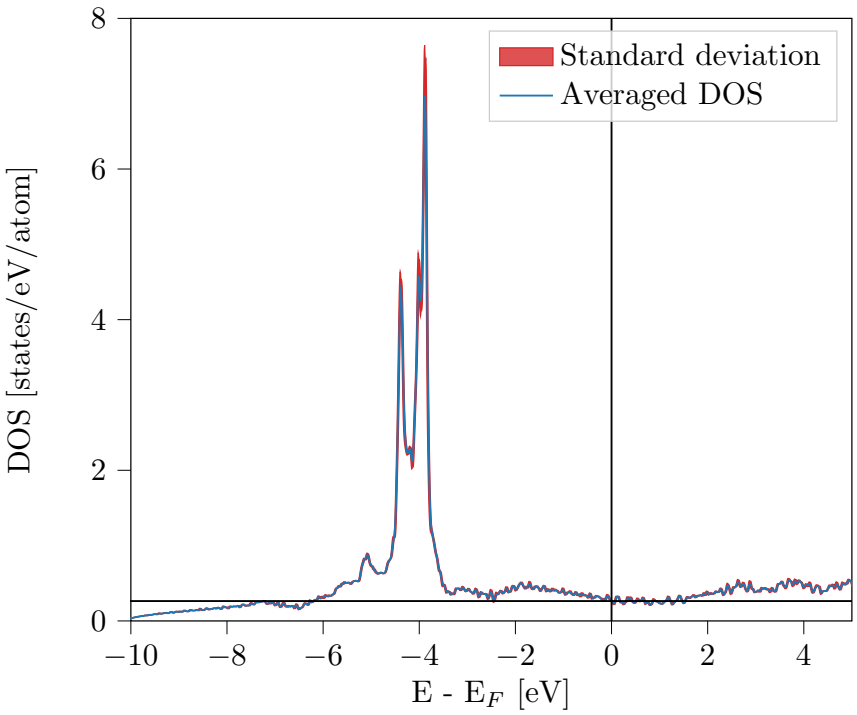

Figure 5.45: Calculated density of states of the unexcited θ' structure of the Al-Cu alloys.

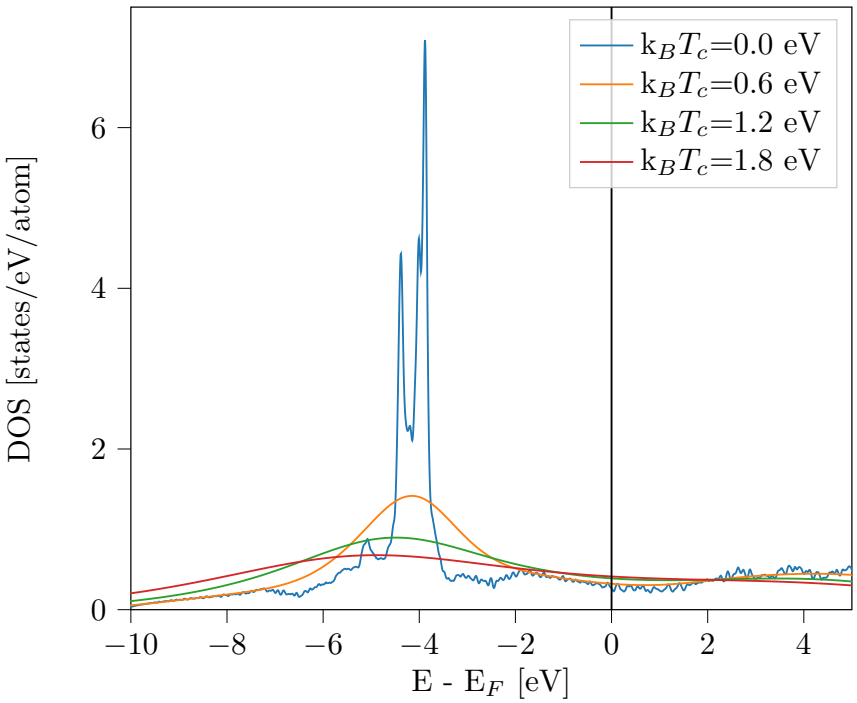

Figure 5.46: Calculated density of states of the θ' structure of the Al-Cu alloys at different electron temperatures T_c.

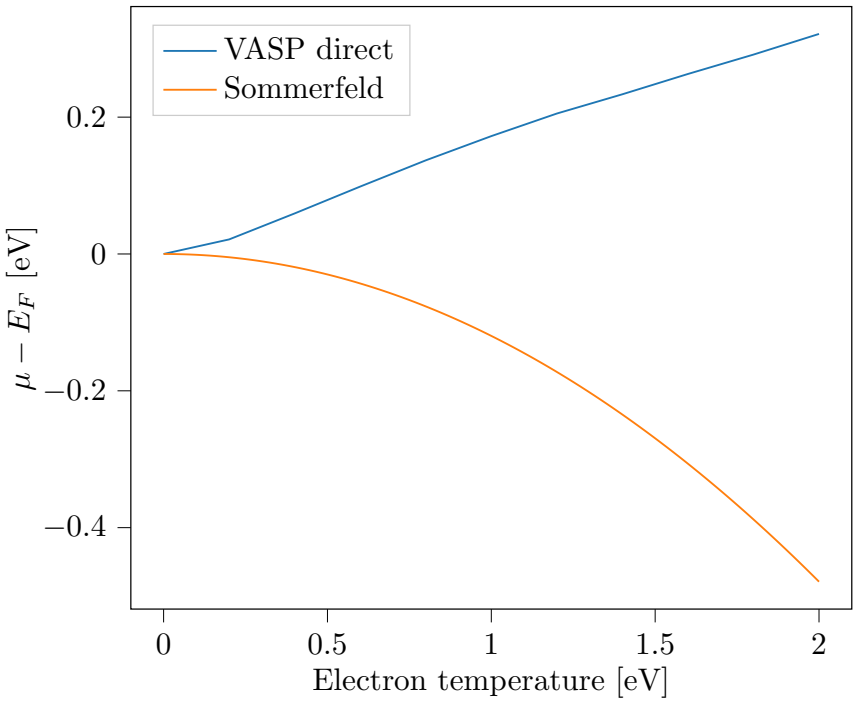

Figure 5.47: Electron temperature-dependent chemical potential of the non-excited θ' structure of the Al-Cu alloys compared to the Sommerfeld model.

Chapter 6

Summary and outlook

In this work, we investigated the excitation-induced effects in pure aluminium and copper, as well as in several Al-Cu alloys. We started by investigating the structures in which each system relaxes if it is allowed to do so. Doing so, we found that all of them expand due to the increasing degeneracy pressure of the electrons.
Now that we knew that we could expect some kind of non-thermal effects as a consquence of the excitation in our metallic systems, we mainly focused on the unexcited structure with the electrons being in different degrees of excitation. We did this since during ultrafast laser-excitations, the electrons are excited almost immediately while the atoms take a comparably long time to relax into a new equilibrium structure. In these unexcited structures, we first calculated the elastic constants and found a non-monotonous behaviour in both pure aluminium and copper. Analysing Born's stability criteria, we found the stability of aluminium and copper to be increasing with the electron temperature. This is opposed to silicon in which we found an increasing instability at least at higher electron temperatures. Al-Cu alloys are different than metals and semiconductors in this regard and we unfortunately couldn't make a clear prediction of the lattice stability of the alloys based on the elastic constants alone.
This motivated us further to calculate the phonon spectra of all our systems of interest. Doing so, we found bond-weakening at low temperatures and bond-hardening at high temperatures in aluminium, bond-hardening in copper, as well as bond-hardening in the Al-Cu alloys.
Finally, attempts were made to calculate the electron temperature-dependent density of states of the materials of interest to confirm thermodynamic properties beyond the Sommerfeld expansion. This part of the work, however, wasn't fruitful but could be revisited in a separate work in the future. Also, we found that the pressure plays an important role in the bond strength. Therefore, it could be worth calculating phonon spectra and elastic constants under different pressures to see the influence of pressure waves arising during laser treatment of a solid. Next, one could of course repeat the calculations performed in this work with different materials to build up a database of excitation-induced effects. Lastly, coming back to the original purpose of this work, a logical step is to develop interatomic potentials that can be used for molecular dynamics simulations. From what we've learned

in this work, we can assume that in MD-simulations with only an interaction potential for $T_c = 0$, the melting temperature following laser irradiation would be underestimating the more accurate melting temperature obtained from a T_c-dependent interatomic potential. In the case of laser ablation simulations, this would mean that the ablation threshold would also be underestimated. It is difficult to make predictions on how the material dynamics differ when using a T_c-dependent or a T_c-independent potential since more properties than just the interaction strength play a role in the material dynamics, such as the heat capacity, electron-phonon coupling constants. With a T_c-dependent interaction potential, one could investigate how the non-thermal effects affect the laser ablation processes in detail. From similar works on silicon [2], we know that this could allow for completely new insights into the melting and ablation dynamics. Work in this direction has already started but due to the complicacy of developing electron temperature-dependent interatomic potentials is not finished yet.

Appendices

Appendix A

Proof of the first Hohenberg-Kohn theorem

The fact that the external field contribution to the energy functional is a unique functional of the electron density is the first Hohenberg-Kohn theorem. It can be shown by assuming

$$E = \langle \Psi | \, H \, | \Psi \rangle < E' = \langle \Psi' | \, H' \, | \Psi' \rangle \, . \tag{A.1}$$

We can rewrite this inequality as

$$\begin{aligned} E \overset{(*)}{<} \langle \Psi' | \, H \, | \Psi' \rangle &= \langle \Psi' | \, H + H' - H' \, | \Psi' \rangle = \langle \Psi' | \, H' \, | \Psi' \rangle + \langle \Psi' | \, H - H' \, | \Psi' \rangle \\ &= E' + \langle \Psi' | \, H - H' \, | \Psi' \rangle \, . \end{aligned} \tag{A.2}$$

Analoguously, we find

$$\begin{aligned} E' \overset{(*)}{<} \langle \Psi | \, H \, | \Psi \rangle &= \langle \Psi | \, H + H' - H' \, | \Psi \rangle = \langle \Psi' | \, H' \, | \Psi \rangle + \langle \Psi | \, H - H' \, | \Psi \rangle \\ &= E' + \langle \Psi | \, H - H' \, | \Psi \rangle \, . \end{aligned} \tag{A.3}$$

In $(*)$, we used the Rayleigh-Ritz principle which states that varying an eigenvector of an operator will always lead to a higher eigenvalue [4, 46].
Also asuming that the two energy functionals $E[n(\vec{r})]$, $E'[n'(\vec{r})]$ can be written as

$$E[n(\vec{r})] = T[n(\vec{r})] + U[n(\vec{r})] + \int \mathrm{d}\vec{r}\, v(\vec{r}) n(\vec{r}) \tag{A.4}$$

and

$$E'[n'(\vec{r})] = T'[n'(\vec{r})] + U'[n'(\vec{r})] + \int \mathrm{d}\vec{r}\, v'(\vec{r}) n'(\vec{r}), \tag{A.5}$$

we find

$$E < E' + \int \mathrm{d}\vec{r} [v(\vec{r}) - v'(\vec{r})] n'(\vec{r}) \tag{A.6}$$

and

$$E' < E + \int \mathrm{d}\vec{r} [v'(\vec{r}) - v(\vec{r})] n(\vec{r}). \tag{A.7}$$

Adding both expressions yields

$$E + E' < E + E' + \int \mathrm{d}\vec{r}\,[v(\vec{r}) - v'(\vec{r})]n'(\vec{r}) + \int \mathrm{d}\vec{r}\,[v'(\vec{r}) - v(\vec{r})]n(\vec{r}). \tag{A.8}$$

If we now also assume

$$n(\vec{r}) = n'(\vec{r}), \tag{A.9}$$

we find the contradicting expression

$$E + E' < E + E'. \tag{A.10}$$

Therefore, the assumption (A.1) doesn't hold; the energy functional is indeed a unique functional of the electron density and also, the electron density is unique given an external potential.

Appendix B

Sommerfeld expansion

The Sommerfeld expansion [47, 48] is a low-temperature approximation for some integral of the form

$$\langle H \rangle := \int_{-\infty}^{\infty} H(E) f(E,T)\,\mathrm{d}E \tag{B.1}$$

with the Fermi-Dirac distribution

$$f(E,T) = \frac{1}{\exp\left(\frac{E-\mu}{\mathrm{k_B}T}\right)+1} \tag{B.2}$$

and some function $H(E)$ which we assume only depends on the single-particle energy E. Note that even though the temperature that is of interest here is the electron temperature. Still, we will write T instead of T_c here. We define

$$H(E) = \frac{\partial K(E)}{\partial E} \Rightarrow K(E) = \int_{-\infty}^{E} H(E')\,\mathrm{d}E' \tag{B.3}$$

Therefore, we can write

$$\begin{aligned}\langle H \rangle &= \int_{-\infty}^{\infty} \frac{\partial K(E)}{\partial E} f(E,T)\,\mathrm{d}e \overset{P.I.}{=} [K(E)f(E,T)]_{-\infty}^{\infty} - \int_{-\infty}^{\infty} K(E)\frac{\partial f(E,T)}{\partial E}\,\mathrm{d}E \\ &= \lim_{E\to\infty} K(E)f(E,T) - \lim_{E\to-\infty} - \int_{-\infty}^{\infty} K(E)\frac{\partial f(E,T)}{\partial E}\,\mathrm{d}E \\ &= - \int_{-\infty}^{\infty} K(E)\frac{\partial f(E,T)}{\partial E]}\,\mathrm{d}E\,. \end{aligned} \tag{B.4}$$

The first contribution in the second line vanishes since

$$\lim_{E\to\infty} f(E,T) = 0 \tag{B.5}$$

and the second contribution vanishes due to the assumption

$$\lim_{E\to\infty} K(E) = 0 \tag{B.6}$$

which is justified from the original definition of $K(E)$ in (B.3). Expanding $K(E)$ in a Taylor series around μ yields

$$K(E) = K(\mu) + \frac{\partial K(E)}{\partial E}\bigg|_{\mu}(E-\mu) + \frac{\partial^2 K(E)}{\partial E^2}\bigg|_{\mu}\frac{(E-\mu)^2}{2} + \mathcal{O}\big((E-\mu)^2\big) \tag{B.7}$$

and thus

$$\begin{aligned}\langle H\rangle &\approx \int_{-\infty}^{\infty}\left[K(\mu) + \frac{\partial K(E)}{\partial E}\bigg|_{\mu}(E-\mu) + \frac{\partial^2 K(E)}{\partial E^2}\bigg|_{\mu}\frac{(E-\mu)^2}{2}\right]\frac{\partial}{\partial f(E,T)}\,\mathrm{d}E \\ &= -\int_{-\infty}^{\infty} K(\mu)\frac{\partial f(E,T)}{\partial E}\,\mathrm{d}E - \int_{-\infty}^{\infty}\frac{\partial K(E)}{\partial E}\bigg|_{\mu}(E-\mu)\frac{\partial f(E,T)}{\partial E}\,\mathrm{d}E \qquad \text{(B.8)} \\ &\quad + \int_{-\infty}^{\infty}\frac{\partial^2 K(E)}{\partial E^2}\bigg|_{\mu}\frac{(E-\mu)^2}{2}\frac{\partial f(E,T)}{\partial E}\,\mathrm{d}E\,. \qquad \text{(B.9)}\end{aligned}$$

In order to avoid lenghty expression, we split this expression up into the three contributions. The first one reduces to

$$\begin{aligned}-\int_{-\infty}^{\infty} K(\mu)\frac{\partial f(E,T)}{\partial E}\,\mathrm{d}E =& K(\mu)[f(E,T)]_{-\infty}^{\infty} = -K(\mu)[f(\infty) - f(-\infty)] \\ =& K(\mu) \overset{!}{=} \int_{-\infty}^{\mu} H(E)\,\mathrm{d}E\end{aligned} \tag{B.10}$$

To obtain this, we used $\lim_{E\to\infty} f(E,T) = 0$ and $\lim_{E\to-\infty} f(E,T) = 1$, as well as the definition (B.3). The second contribution to (B.9) reads

$$\begin{aligned}&\int_{-\infty}^{\infty}\frac{\partial K(E)}{\partial E}\bigg|_{\mu}(E-\mu)\frac{\partial f(E,T)}{\partial E}\,\mathrm{d}E \\ =& -\frac{\partial K(E)}{\partial E}\bigg|_{\mu}\int_{-\infty}^{\infty}(E-\mu)\frac{\partial}{\partial E}\left[\frac{1}{\exp\left(\frac{E-\mu}{\mathrm{k_B}T}\right)+1}\right] \\ =& \frac{\partial K(E)}{\partial E}\bigg|_{\mu}\int_{-\infty}^{\infty}(E-\mu)\frac{\frac{1}{\mathrm{k_B}T}\exp\left(\frac{E-\mu}{\mathrm{k_B}T}\right)}{\left[\exp\left(\frac{E-\mu}{\mathrm{k_B}}\right)+1\right]^2} = 0\end{aligned} \tag{B.11}$$

since the integrand is asymmetric in E. The third contribution to (B.9) is

$$\begin{aligned}
&-\int_{-\infty}^{\infty}\frac{\partial^2 K(E)}{\partial E^2}\bigg|_{\mu}\frac{(E-\mu)}{2}\frac{\partial f(E,T)}{\partial E}\,\mathrm{d}E\\
=&\int_{-\infty}^{\infty}\frac{\partial^2 K(E)}{\partial E^2}\bigg|_{\mu}\frac{(E-\mu)}{2}\frac{\frac{1}{\mathrm{k_B}T}\exp\left(\frac{E-\mu}{\mathrm{k_B}T}\right)}{\left[\exp\left(\frac{E-\mu}{\mathrm{k_B}T}\right)+1\right]^2}\,\mathrm{d}E\\
=&\frac{1}{2}\frac{\partial^2 K(E)}{\partial E^2}\bigg|_{\mu}\mathrm{k_B}T\int_{-\infty}^{\infty}\left(\frac{E-\mu}{\mathrm{k_B}T}\right)^2\frac{\exp\left(\frac{E-\mu}{\mathrm{k_B}T}\right)}{\left[\exp\left(\frac{E-\mu}{\mathrm{k_B}T}\right)+1\right]^2}\,\mathrm{d}E\\
=&\frac{(\mathrm{k_B}T)^2}{2}\frac{\partial^2 K(E)}{\partial E^2}\bigg|_{\mu}\underbrace{\int_{-\infty}^{\infty}\frac{x^2\exp(x)}{[\exp(x)+1]^2}\,\mathrm{d}x}_{=\frac{\pi^2}{3}}=\frac{\pi^2}{6}(\mathrm{k_B}T)^2\frac{\partial^2 K(E)}{\partial E^2}\bigg|_{\mu}
\end{aligned}\tag{B.12}$$

where we used the transformation $x := \frac{E-\mu}{\mathrm{k_B}T}$. Putting everything together, we find

$$\begin{aligned}
\langle H\rangle &\approx \int_{-\infty}^{\mu}H(E)\,\mathrm{d}E+\frac{\pi^2}{6}(\mathrm{k_B}T)^2\frac{\partial^2 K(E)}{\partial E^2}\bigg|_{\mu}\\
&=\int_{-\infty}^{\mu}H(E)\,\mathrm{d}E+\frac{\pi^2}{6}(\mathrm{k_B}T)^2\frac{\partial H(E)}{\partial E}\bigg|_{\mu}
\end{aligned}\tag{B.13}$$

This expression can now be used to approximate several thermodynamic properties. In the following, we will derive expressions for the chemical potential, the internal energy, the heat capacity, the entropy, the Helmholtz free energy and the pressure.

Chemical potential:

The chemical potential is defined indirectly by the number of electrons which - within the Sommerfeld expansion up to second order in $\mathrm{k_B}T$ - can be approximated as

$$N=\int_{-\infty}^{\infty}f(E,T)D(E)\,\mathrm{d}E\approx\int_{-\infty}^{\mu}D(E)\,\mathrm{d}E+\frac{\pi^2}{6}(\mathrm{k_B})^2\frac{\partial D(E)}{\partial E}\bigg|_{\mu}.\tag{B.14}$$

Using the DOS of a free electron gas from (2.33), we can write

$$\begin{aligned}
N \approx & \frac{\Omega}{2\pi^2}\left(\frac{2m}{\hbar^2}\right)^{3/2}\int_{-\infty}^{\mu}\sqrt{E}\,\mathrm{d}E + \frac{\pi^2}{6}(\mathrm{k_B}T)^2\frac{\partial D(E)}{\partial E}\bigg|_{\mu} \\
= & \frac{\Omega}{2\pi^2}\left(\frac{2m}{\hbar^2}\right)^{3/2}\left\{\int_{-\infty}^{E_\mathrm{F}}\sqrt{E}\,\mathrm{d}E + \int_{E_\mathrm{F}}^{\mu}\sqrt{E}\,\mathrm{d}E\right\} + \frac{\pi^2}{6}(\mathrm{k_B}T)^2\frac{\partial D(E)}{\partial E}\bigg|_{\mu} \\
\approx & \frac{\Omega}{2\pi^2}\left(\frac{2m}{\hbar^2}\right)^{3/2}\int_{-\infty}^{E_\mathrm{F}}\sqrt{E}\,\mathrm{d}E + \frac{\Omega}{2\pi^2}\left(\frac{2m}{\hbar^2}\right)^{3/2}\sqrt{E_\mathrm{F}}(\mu - E_\mathrm{F}) \\
& + \frac{\pi^2}{6}(\mathrm{k_B}T)^2\frac{\partial D(E)}{\partial E}\bigg|_{\mu} \\
= & N + D(E_\mathrm{F})(\mu - E_\mathrm{F}) + \frac{\pi^2}{6}(\mathrm{k_B}T)^2\frac{\partial D(E)}{\partial E}\bigg|_{\mu}
\end{aligned} \tag{B.15}$$

Here, we used the definition of the number of electrons at zero-temperature

$$N = \frac{\Omega}{2\pi^2}\left(\frac{2m}{\hbar^2}\right)^{3/2}\int_{-\infty}^{E_\mathrm{F}}\sqrt{E}\,\mathrm{d}E\,. \tag{B.16}$$

Rewriting this, immediately yields

$$D(E_\mathrm{F})(\mu - E_\mathrm{F}) = -\frac{\pi^2}{6}\frac{\partial D(E)}{\partial E}\bigg|_{E_\mathrm{F}}(\mathrm{k_B}T)^2 \tag{B.17}$$

and finally

$$\mu = E_\mathrm{F} - \frac{\pi^2}{6}\frac{\partial_E D(E)\big|_{E_\mathrm{F}}}{D(E_\mathrm{F})}(\mathrm{k_B}T)^2 = E_\mathrm{F}\left[1 - \frac{\pi^2}{12}\left(\frac{\mathrm{k_B}T}{E_\mathrm{F}}\right)^2\right] \tag{B.18}$$

where we used the fact that $D(E) \propto \sqrt{E}$.

Internal energy:
The internal energy - again using the Sommerfeld expansion up to second order in $\mathrm{k_B}T$ is

$$\begin{aligned}
U = & \int_{-\infty}^{\infty} ED(E)f(E,T)\,\mathrm{d}E \approx \int_{-\infty}^{\mu} ED(E)\,\mathrm{d}E + \frac{\pi^2}{6}(\mathrm{k_B}T)^2\frac{\partial ED(E)}{\partial E}\bigg|_{\mu} \\
= & \int_{-\infty}^{E_\mathrm{F}} ED(E)\,\mathrm{d}E + \int_{E_\mathrm{F}}^{\mu} ED(E)\,\mathrm{d}E + \frac{\pi^2}{6}(\mathrm{k_B}T)^2\frac{\partial ED(E)}{\partial E}\bigg|_{\mu}
\end{aligned} \tag{B.19}$$

As before, we split this expression into its three constituents. The first one, also referred

to as ground state energy can be written as

$$\begin{aligned}\int_{-\infty}^{E_\mathrm{F}} ED(E)\,\mathrm{d}E =&\frac{\Omega}{2\pi^2}\left(\frac{2m}{\hbar^2}\right)^{3/2}\int_{-\infty}^{E_\mathrm{F}} E\sqrt{E}\,\mathrm{d}E = \frac{\Omega}{2\pi^2}\left(\frac{2m}{\hbar^2}\right)^{3/2}\left[\frac{2}{5}E^{5/2}\right]_{-\infty}^{E_\mathrm{F}}\\ =&\frac{\Omega}{2\pi^2}\left(\frac{2m}{\hbar^2}\right)^{3/2}\left[\frac{2}{5}E^{5/2}\right]_{0}^{E_\mathrm{F}} = \frac{\Omega}{2\pi^2}\left(\frac{2m}{\hbar^2}\right)^{3/2}\frac{2}{5}E_\mathrm{F}^{5/2}\\ =&\frac{2}{5}D(E_\mathrm{F})E_\mathrm{F}^2 =: U_0. \end{aligned} \tag{B.20}$$

From (B.16), we know that

$$\begin{aligned}N =&\frac{\Omega}{2\pi^2}\left(\frac{2m}{\hbar^2}\right)^{3/2}\int_{-\infty}^{E_\mathrm{F}} \sqrt{E}\,\mathrm{d}E = \frac{\Omega}{2\pi^2}\left(\frac{2m}{\hbar^2}\right)^{3/2}\left[\frac{2}{3}E^{3/2}\right]_{-\infty}^{E_\mathrm{F}}\\ =&= \frac{\Omega}{2\pi^2}\left(\frac{2m}{\hbar^2}\right)^{3/2}\left[\frac{2}{3}E^{3/2}\right]_{0}^{E_\mathrm{F}} = \frac{2}{3}D(E_\mathrm{F})E_\mathrm{F}. \end{aligned} \tag{B.21}$$

On the other hand, we know from (B.20) that the ground state energy density is given by

$$u_0 = \frac{U_0}{N} = \frac{2}{5}\frac{D(E_\mathrm{F}E_\mathrm{F}^2}{N} = \frac{3}{5}E_\mathrm{F}. \tag{B.22}$$

This is in contrast to an ideal gas with $\frac{E}{N} = \frac{3}{2}\mathrm{k_B}T$, which for zero-temperature vanishes. For the second contribution, we use (B.17) to write

$$\begin{aligned}\int_{E_\mathrm{F}}^{\mu} ED(E)\,\mathrm{d}E \approx&D(E_\mathrm{F})(\mu - E_\mathrm{F})E_\mathrm{F} = -\frac{\pi^2}{6}\frac{\partial D(E)}{\partial E}\bigg|_{E_\mathrm{F}}(\mathrm{k_B}T)^2E_\mathrm{F}\\ =&-\frac{\pi^2}{6}(\mathrm{k_B}T)^2E_\mathrm{F}\frac{\Omega}{2\pi^2}\left(\frac{2m}{\hbar^2}\right)^{3/2}\frac{\partial\sqrt{E}}{\partial E}\bigg|_{E_\mathrm{F}}\\ =&-\frac{\pi^2}{6}(\mathrm{k_B}T)^2E_\mathrm{F}\frac{\Omega}{2\pi^2}\left(\frac{2m}{\hbar^2}\right)^{3/2}\frac{1}{2\sqrt{E_\mathrm{F}}}\\ =&-\frac{\pi^2}{12}(\mathrm{k_B}T)^2\frac{\Omega}{2\pi^2}\left(\frac{2m}{\hbar^2}\right)^{3/2}\sqrt{E_\mathrm{F}} = -\frac{\pi^2}{12}(\mathrm{k_B}T)^2D(E_\mathrm{F}). \end{aligned} \tag{B.23}$$

The third contribution reads

$$\begin{aligned}\frac{\pi^2}{6}(\mathrm{k_B}T)^2\frac{\partial ED(E)}{\partial E}\bigg|_{\mu} =&\frac{\pi^2}{6}(\mathrm{k_B}T)^2\left[D(E)\bigg|_{\mu} + E\frac{\partial D(E)}{\partial E}\bigg|_{\mu}\right]\\ \approx&\frac{\pi^2}{6}(\mathrm{k_B}T)^2\left[D(E_\mathrm{F}) + E\frac{\Omega}{2\pi^2}\left(\frac{2m}{\hbar^2}\right)^{3/2}\frac{\partial\sqrt{E}}{\partial E}\bigg|_{\mu}\right]\\ =&\frac{\pi^2}{6}(\mathrm{k_B}T)^2\left[D(E_\mathrm{F}) + \frac{\Omega}{2\pi^2}\left(\frac{2m}{\hbar^2}\right)^{3/2}\frac{E}{2\sqrt{E}}\bigg|_{\mu}\right]\\ \approx&\frac{\pi^2}{6}(\mathrm{k_B}T)^2\left[D(E_\mathrm{F}) + \frac{1}{2}D(E_\mathrm{F})\right] = \frac{3\pi^2}{12}(\mathrm{k_B}T)^2D(E_\mathrm{F}) \end{aligned} \tag{B.24}$$

Plugging these three parts together, we end up with

$$\begin{aligned} U =& U_0 - \frac{\pi^2}{12}(\mathrm{k_B}T)^2 D(E_\mathrm{F}) + \frac{3\pi^2}{12}(\mathrm{k_B}T)^2 D(E_\mathrm{F}) \\ =& U_0 + \frac{\pi^2}{6}(\mathrm{k_B}T)^2 D(E_\mathrm{F}). \end{aligned} \tag{B.25}$$

Heat capacity:
The heat capacity at constant volume C_V is given by

$$C_V = \frac{\partial U}{\partial T} = \frac{\partial}{\partial T}\left[U_0 + \frac{\pi^2}{6}(\mathrm{k_B}T)^2 D(E_\mathrm{F})\right] = \frac{2\pi^2}{6}\mathrm{k_B^2}TD(E_\mathrm{F}) = \frac{\pi^2}{3}\mathrm{k_B^2}TD(E_\mathrm{F}). \tag{B.26}$$

Entropy:
From the heat capacity, the entropy directly follows

$$S = \int \frac{C_V}{T}\,\mathrm{d}T = \int \frac{\pi^2}{3}\mathrm{k_B^2}D(E_\mathrm{F})\,\mathrm{d}T = \frac{\pi^2}{3}\mathrm{k_B^2}TD(E_\mathrm{F}). \tag{B.27}$$

Helmholtz free energy:
Using the usual definition of the Helmholtz free energy, it can be written as

$$\begin{aligned} F =& U - TS = U_0 + \frac{\pi^2}{6}(\mathrm{k_B}T)^2 D(E_\mathrm{F}) - \frac{\pi^2}{3}(\mathrm{k_B}T)^2 D(E_\mathrm{F}) \\ =& U_0 + \left(\frac{1}{6} - \frac{2}{6}\right)\pi^2(\mathrm{k_B}T)^2 D(E_\mathrm{F}) = U_0 - \frac{\pi^2}{6}(\mathrm{k_B}T)^2 D(E_\mathrm{F}). \end{aligned} \tag{B.28}$$

Pressure:
From the Helmholtz free energy, as well as the definition of the ground state energy (B.20) and (B.22), the pressure can be calculated

$$\begin{aligned} p =& -\left.\frac{\partial F}{\partial \Omega}\right|_{N,T} = -\frac{\partial}{\partial \Omega}\left[\frac{3}{5}NE_\mathrm{F} - \frac{\pi^2}{6}(\mathrm{k_B}T)^2 D(E_\mathrm{F})\right] \\ =& -\frac{3}{5}N\frac{\partial E_\mathrm{F}}{\partial \Omega} - \frac{\pi^2}{6}(\mathrm{k_B}T)^2\frac{\Omega}{2\pi^2}\left(\frac{2m}{\hbar^2}\right)^{3/2}\frac{\partial\sqrt{E_\mathrm{F}}}{\partial \Omega}. \end{aligned} \tag{B.29}$$

Here, it is important to notice that the Fermi energy depends on the volume Ω. Rewriting (B.21), we find

$$E_{\mathrm{F}} = \left[\frac{3}{2}\frac{N}{\frac{\Omega}{2\pi^2}\left(\frac{2m}{\hbar^2}\right)^{3/2}}\right]^{2/3} = \left[\frac{3}{2}\frac{N}{\frac{1}{2\pi^2}\left(\frac{2m}{\hbar^2}\right)^{3/2}}\right]^{2/3}\Omega^{-2/3}. \tag{B.30}$$

Taking the derivative of this expression with respect to the volume Ω, we arrive at

$$\begin{aligned}\frac{\partial E_{\mathrm{F}}}{\partial \Omega} =& \left[\frac{3}{2}\frac{N}{\frac{1}{2\pi^2}\left(\frac{2m}{\hbar^2}\right)^{3/2}}\right]^{2/3}\left(-\frac{2}{3}\right)\Omega^{-5/3} = \left[\frac{3}{2}\frac{N}{\frac{\Omega}{2\pi^2}\left(\frac{2m}{\hbar^2}\right)^{3/2}}\right]^{2/3}\left(-\frac{2}{3}\right)\frac{1}{\Omega} \\ =& -\frac{2}{3}\frac{E_{\mathrm{F}}}{\Omega}\end{aligned} \tag{B.31}$$

and similarly

$$\begin{aligned}\frac{\partial \sqrt{E_{\mathrm{F}}}}{\partial \Omega} =& \left\{\left[\frac{3}{2}\frac{N}{\frac{\Omega}{2\pi^2}\left(\frac{2m}{\hbar^2}\right)^{3/2}}\right]^{2/3}\left(-\frac{2}{3}\right)\frac{1}{\Omega}\right\}^{1/2}\frac{\partial}{\partial \Omega}\left(\Omega^{-2/3}\right)^{1/2} \\ =& \left\{\left[\frac{3}{2}\frac{N}{\frac{\Omega}{2\pi^2}\left(\frac{2m}{\hbar^2}\right)^{3/2}}\right]^{2/3}\left(-\frac{2}{3}\right)\frac{1}{\Omega}\right\}^{1/2}\frac{\partial}{\partial \Omega}\left(\Omega^{-1/3}\right) \\ =& \left\{\left[\frac{3}{2}\frac{N}{\frac{\Omega}{2\pi^2}\left(\frac{2m}{\hbar^2}\right)^{3/2}}\right]^{2/3}\left(-\frac{2}{3}\right)\frac{1}{\Omega}\right\}^{1/2}\left(-\frac{1}{3}\right)\Omega^{-4/3} = -\frac{1}{3\Omega}\sqrt{E_{\mathrm{F}}}\end{aligned} \tag{B.32}$$

Plugging these findings into the definition of the pressure, we end up with

$$\begin{aligned}p =& -\frac{3}{5}N\left(-\frac{2}{3}\frac{E_{\mathrm{F}}}{\Omega}\right) - \frac{\pi^2}{6}\left(\mathrm{k_B}T\right)^2\frac{\Omega}{2\pi^2}\left(\frac{2m}{\hbar^2}\right)^{3/2}\left(-\frac{1}{3\Omega}\sqrt{E_{\mathrm{F}}}\right) \\ =& \frac{2}{5}\frac{N}{\Omega}E_{\mathrm{F}} + \frac{\pi^2}{18}\left(\mathrm{k_B}T\right)^2 D(E_{\mathrm{F}}).\end{aligned} \tag{B.33}$$

We want to point out that the ground state contribution to the pressure can be found in literature. We could however not find any source stating the pressure's temperature-dependence. Furthermore, we want to point out that as can already be seen by only considering the ground state pressure at zero-temperature, the free electron gas experiences a pressure. This pressure emerges from the Pauli exclusion principle and would not be seen in an ideal gas at zero-temperature.

Appendix C

DFPT

Let

$$H_{SCF}\left|\psi_n\right\rangle = \epsilon_n \left|\psi_n\right\rangle \tag{C.1}$$

be the unperturbed Schrödinger equation. From first-order perturbation theory, we obtain

$$\begin{aligned}
\left(H_{SCF} + \Delta V_{SCF}\right)\left|\psi_n + \Delta\psi_n\right\rangle =& H_{SCF}\left|\psi_n\right\rangle + H_{SCF}\left|\Delta\psi_n\right\rangle + \Delta V_{SCF}\left|\psi_n\right\rangle \\
&+ \Delta V_{SCF}\left|\Delta\psi_n\right\rangle \\
=& \epsilon_n\left|\psi_n\right\rangle + H_{SCF}\left|\Delta\psi_n\right\rangle + \Delta V_{SCF}\left|\psi_n\right\rangle \\
&+ \Delta\epsilon_n\left|\Delta\psi_n\right\rangle \\
\overset{!}{=}& \left(\epsilon_n + \Delta\epsilon_n\right)\left|\psi_n + \Delta\psi_n\right\rangle \\
=& \epsilon_n\left|\psi_n\right\rangle + \epsilon_n\left|\Delta\psi_n\right\rangle + \Delta\epsilon_n\left|\psi_n\right\rangle + \Delta\epsilon\left|\Delta\psi_n\right\rangle
\end{aligned}$$

$$\Leftrightarrow \qquad \left(H_{SCF} - \epsilon_n\right)\left|\Delta\psi_n\right\rangle = -\left(\Delta V_{SCF} - \Delta\epsilon_n\right)\left|\psi_n\right\rangle \tag{C.2}$$

with the first-order energy correction

$$\Delta\epsilon_n = \left\langle\psi_n\right| \Delta V \left|\psi_n\right\rangle \tag{C.3}$$

and the perturbation ΔV which contains changes in the external field contribution to the energy, as well as the Coulomb interaction and exchange-correlation effects due to their dependence on the electron density (2.2). We find that we can solve the system analogously to the unperturbed Kohn-Sham equations (2.5).

Appendix D

FT-DFT

Following [49], we can find an expression for the change in the energy in the case of finite-temperature DFT calculations due to the smearing of the electron occupations with the Fermi-Dirac distribution

$$f_i := f(E_i, T) = \frac{1}{\exp(\beta(E_i - \mu)) + 1} \tag{D.1}$$

where $\beta = \frac{1}{\mathrm{k_B}T}$ is the inverse electron temperature. In order to take partial occupancies into account, we have to add

$$\Delta E = \sum_i \int \mathrm{d}f_i \, E_i(f_i) \tag{D.2}$$

to the energy functional. Here, the values E_i are taken as the inverse function of the Fermi-Dirac distribution

$$E_i = \frac{1}{\beta} \ln\left(\frac{1 - f_i}{f_i}\right) + \mu. \tag{D.3}$$

Inserting this into (D.2) and performing the integration, as well as assuming the conservation of electrons, we end up with

$$\Delta E = \frac{1}{\beta} \sum_i [f_i \ln(f_i) + (1 - f_i) \cdot \ln(1 - f_i)]. \tag{D.4}$$

In units of $\mathrm{k_B}T$, the free energy is thus modified to [50]

$$F = E - \sum_i \sigma S(f_i) \tag{D.5}$$

where σ is the smearing and

$$S(f_i) = -[f_i \ln(f_i) + (1 - f_i) \cdot \ln(1 - f_i)] \tag{D.6}$$

the entropy. Similar expressions can be derived for other types of smearing but are irrelevant here.

Appendix E

Plausibility tests of non-thermal effects

Here, we present the results of several plausibility checks to make sure that the effects that we see from finite-temperature DFT calculations are not related to parameters of methods that are inadequate. We start by repeating our calculations with a stricter convergence criterion EDIFF, a denser k-space grid, a higher cutoff energy ENCUT, as well as taking spin-polarisation into account (ISPIN) and using more bands for the calculations (NBANDS). The resulting free energy per atom is shown in figure E.1 for aluminium and in figure E.4 for copper, the internal energy per atom is shown in figure E.2 for aluminium and in figure E.5 for copper and the volume per atom is shown in figure E.3 for aluminium and in figure E.6 for copper. In all plots, it becomes obvious that none of these parameters change the general trend of either of the thermodynamic properties. We also tested whether it makes a difference if we turn off the symmetries that VASP uses to accelerate the calculations with no noticeable difference.
As the next step, it has to be ensured that the exchange correlation functional PBE is still capable of reproducing the correct trend with high T_c. Thus, the free energy, internal energy and lattice constant are calculated using the LDA functional at different T_c. From the free energy shown in figure E.7, the internal energy shown in figure E.8 and the lattice constant shown in figure E.9, it becomes obvious, that DFT calculations with both, LDA and PBE exchange-correlation functionals reproduce the same behaviour.
This finding finally ensures us that the trends of the thermodynamic properties are not influences by the parameters used in our calculations and that they are save to use even at high electron temperatures.

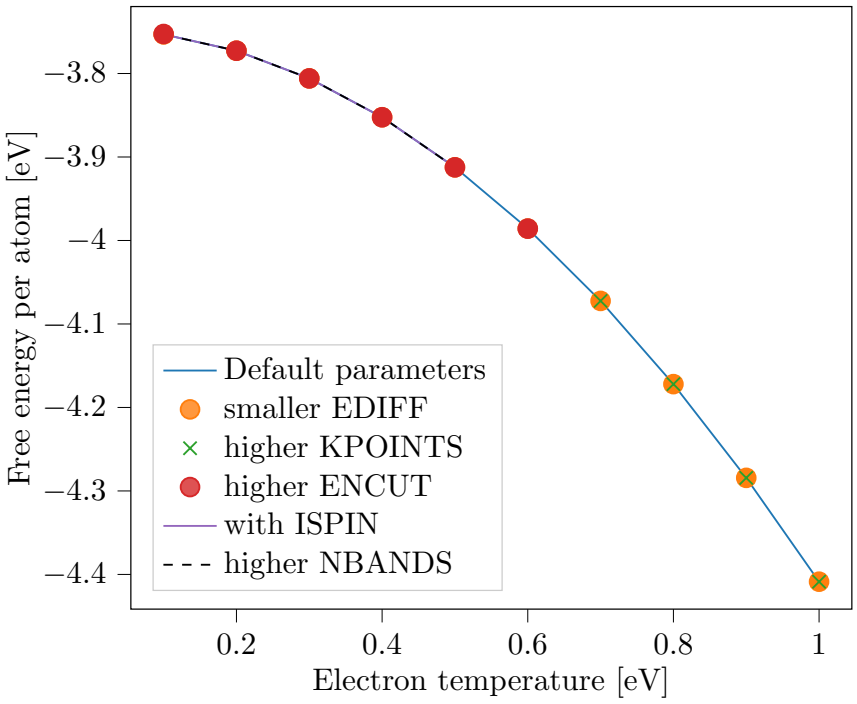

Figure E.1: Free energy per atom in Al at different electron temperatures using the previously stated parameters, as well as a more strict convergence criterion, a denser k-space grid, a higher energy cutoff and number of bands considered in the calculation, as well as taking spin-polarization into account.

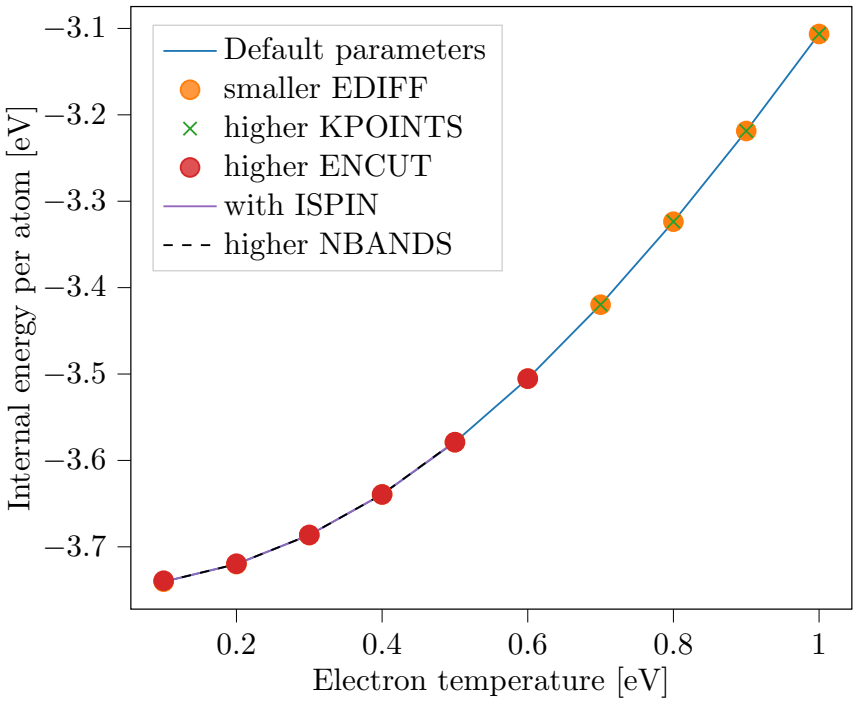

Figure E.2: Internal energy per atom in Al at different electron temperatures using the previously stated parameters, as well as a more strict convergence criterion, a denser k-space grid, a higher energy cutoff and number of bands considered in the calculation, as well as taking spin-polarization into account.

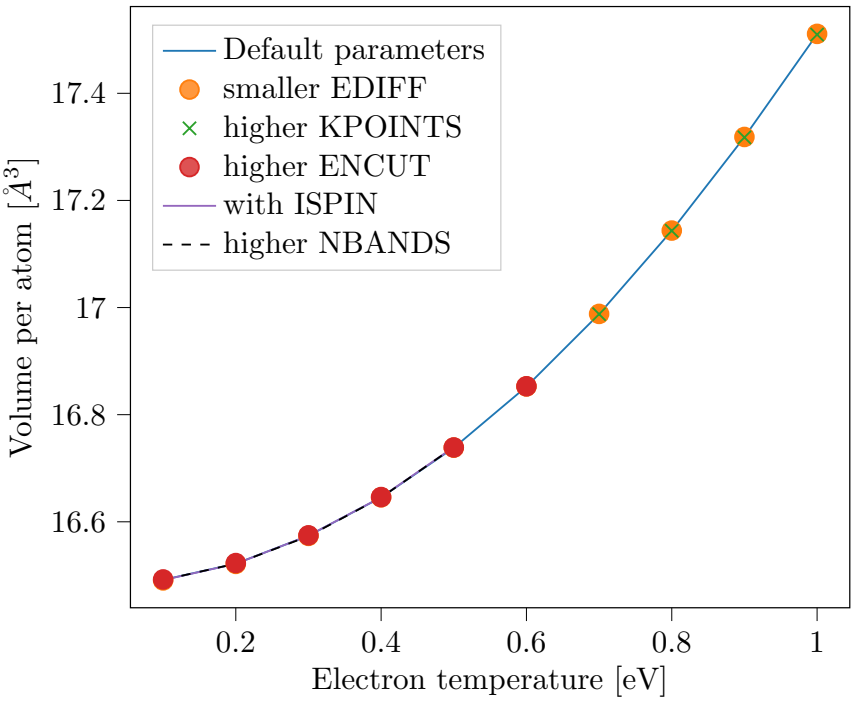

Figure E.3: Lattice constant in Al at different electron temperatures using the previously stated parameters, as well as a more strict convergence criterion, a denser k-space grid, a higher energy cutoff and number of bands considered in the calculation, as well as taking spin-polarization into account.

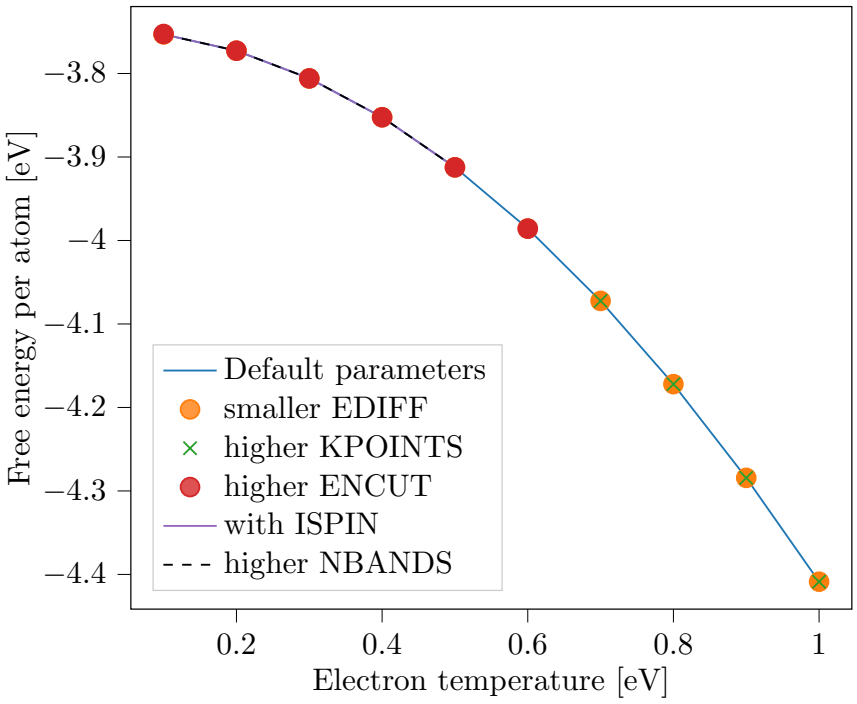

Figure E.4: Free energy per atom in Cu at different electron temperatures using the previously stated parameters, as well as a more strict convergence criterion, a denser k-space grid, a higher energy cutoff and number of bands considered in the calculation, as well as taking spin-polarization into account.

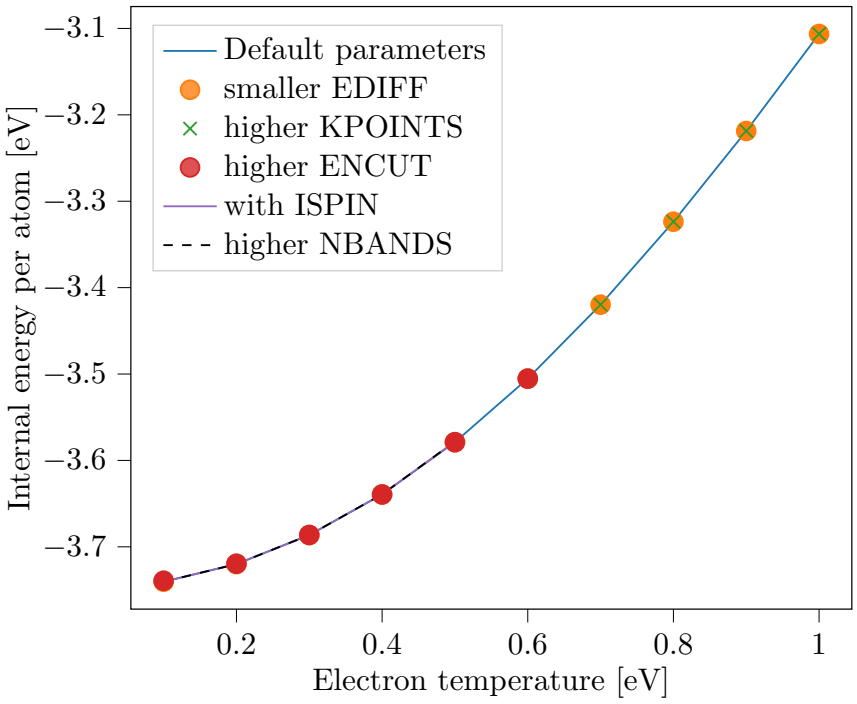

Figure E.5: Internal energy per atom in Cu at different electron temperatures using the previously stated parameters, as well as a more strict convergence criterion, a denser k-space grid, a higher energy cutoff and number of bands considered in the calculation, as well as taking spin-polarization into account.

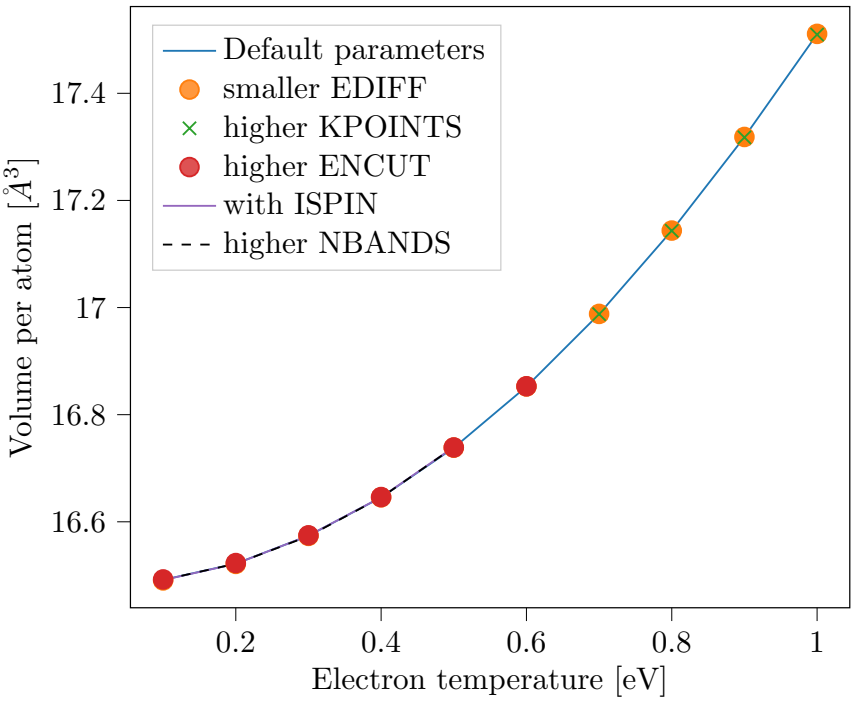

Figure E.6: Lattice constant in Cu at different electron temperatures using the previously stated parameters, as well as a more strict convergence criterion, a denser k-space grid, a higher energy cutoff and number of bands considered in the calculation, as well as taking spin-polarization into account.

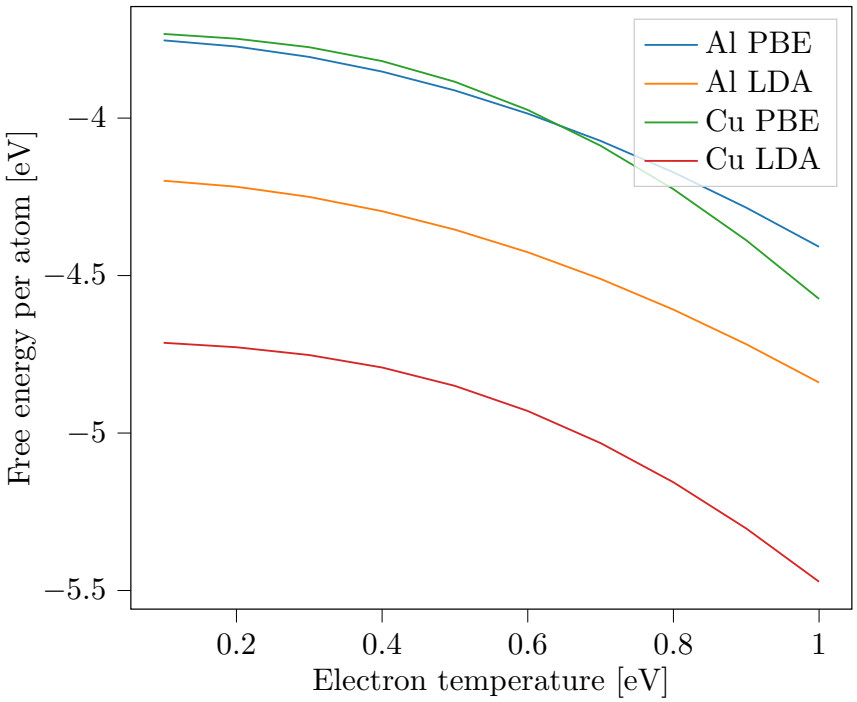

Figure E.7: Free energy per atom in Al and Cu using a LDA and PBE exchange-correlation functional at different electron temperatures.

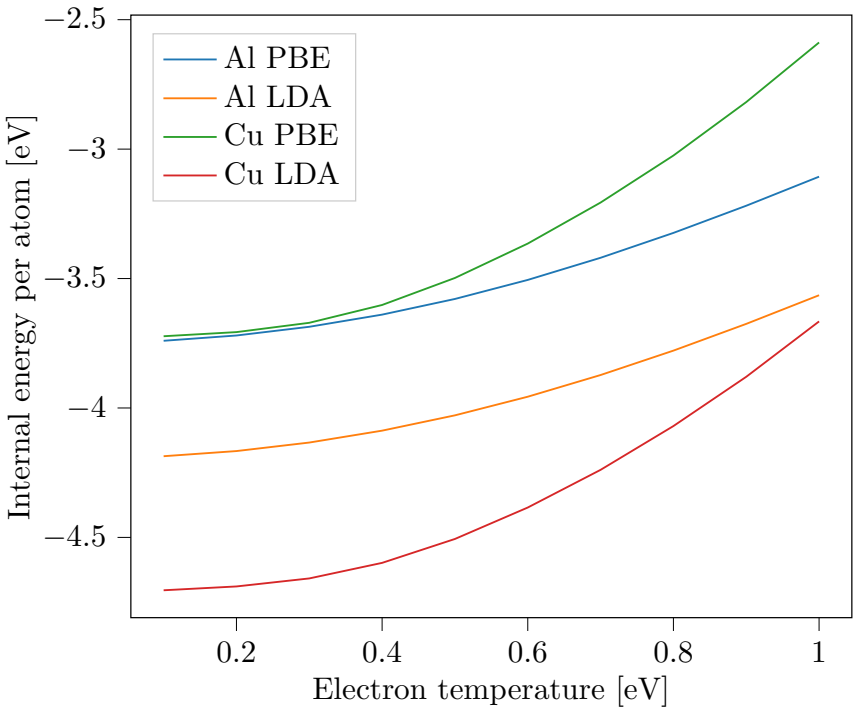

Figure E.8: Internal energy per atom in Al and Cu using a LDA and PBE exchange-correlation functional at different electron temperatures.

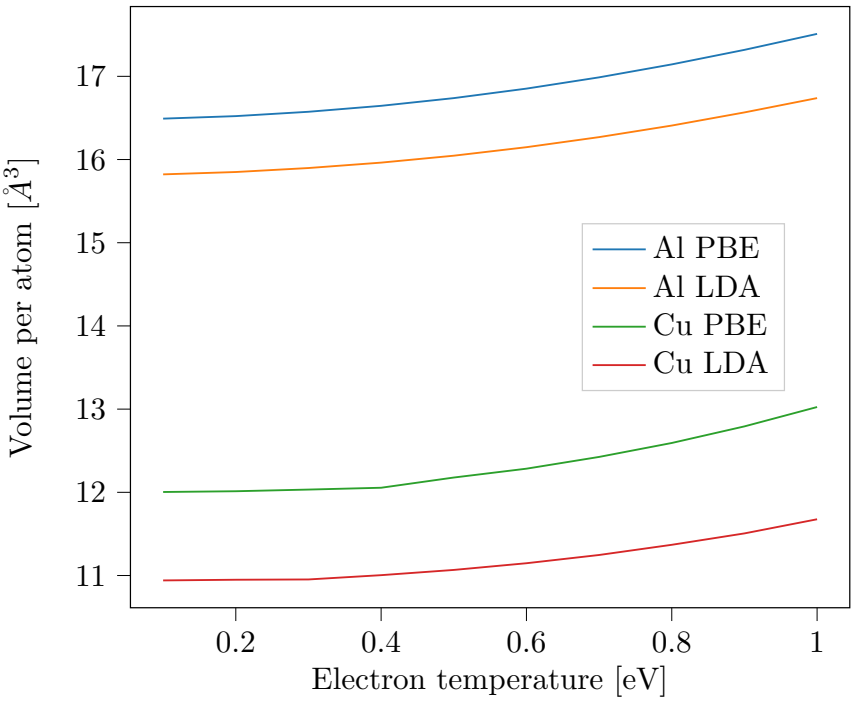

Figure E.9: Lattice constant in Al and Cu using a LDA and PBE exchange-correlation functional at different electron temperatures.

Bibliography

[1] A. Kiselev, "Molecular dynamics simulations of laser ablation in covalent materials," Ph.D. dissertation, 2017. [Online]. Available: https://elib.uni-stuttgart.de/handle/11682/9203

[2] D. Klein, "Laser ablation of covalent materials," Ph.D. dissertation, 2023. [Online]. Available: https://elib.uni-stuttgart.de/handle/11682/13164

[3] P. Hohenberg and W. Kohn, "Inhomogeneous electron gas," *Phys. Rev.*, vol. 136, pp. B864–B871, Nov 1964. [Online]. Available: https://link.aps.org/doi/10.1103/PhysRev.136.B864

[4] J. W. Strutt, *The Theory of Sound*. Macmillan and co., 1877, vol. 1.

[5] W. Kohn and L. J. Sham, "Self-consistent equations including exchange and correlation effects," *Phys. Rev.*, vol. 140, pp. A1133–A1138, Nov 1965. [Online]. Available: https://link.aps.org/doi/10.1103/PhysRev.140.A1133

[6] P. Blaha, K. Schwarz, G. Madsen, D. Kvasnicka, and J. Luitz, "Wien2k: An augmented plane wave plus local orbitals program for calculating crystal properties," *Technische Universität Wien, Wien*, vol. 28, 01 2001.

[7] C. W. Eaker and J. Hinze, "Semiempirical mc [multi-configuration]-scf theory. i. closed shell ground state molecules," *Journal of the American Chemical Society*, vol. 96, no. 13, pp. 4084–4089, 1974. [Online]. Available: https://doi.org/10.1021/ja00820a003

[8] S. Baroni, S. de Gironcoli, A. Dal Corso, and P. Giannozzi, "Phonons and related crystal properties from density-functional perturbation theory," *Rev. Mod. Phys.*, vol. 73, pp. 515–562, Jul 2001. [Online]. Available: https://link.aps.org/doi/10.1103/RevModPhys.73.515

[9] J. Klimeš and A. Michaelides, "Perspective: Advances and challenges in treating van der Waals dispersion forces in density functional theory," *The Journal of Chemical Physics*, vol. 137, no. 12, p. 120901, 09 2012. [Online]. Available: https://doi.org/10.1063/1.4754130

[10] J. P. Perdew, K. Burke, and M. Ernzerhof, "Generalized gradient approximation made simple," *Phys. Rev. Lett.*, vol. 77, pp. 3865–3868, Oct 1996. [Online]. Available: https://link.aps.org/doi/10.1103/PhysRevLett.77.3865

[11] P. Güttinger, "Das verhalten von atomen im magnetischen drehfeld," *Zeitschrift für Physik*, 1932. [Online]. Available: https://doi.org/10.1007/BF01351211

[12] H. Hellmann, "Zur rolle der kinetischen elektronenenergie für die zwischenatomaren kräfte," *Zeitschrift für Physik*, 1933. [Online]. Available: https://doi.org/10.1007/BF01342053

[13] W. Pauli jr, "Über das modell des wasserstoffmolekülions," *Annalen der Physik*, vol. 373, no. 11, pp. 177–240, 1922. [Online]. Available: https://onlinelibrary.wiley.com/doi/abs/10.1002/andp.19223731102

[14] E. Stiefel, "Über einige methoden der relaxationsrechnung," *Zeitschrift für angewandte Mathematik und Physik ZAMP*, 1952.

[15] M. R. Hestenes, "Iterative methods for solving linear equations," *Journal of Optimization Theory and Applications*, 1973.

[16] P. Pulay, "Ab initio calculation of force constants and equilibrium geometries in polyatomic molecules," *Molecular Physics*, vol. 17, no. 2, pp. 197–204, 1969. [Online]. Available: https://doi.org/10.1080/00268976900100941

[17] N. D. Mermin, "Thermal properties of the inhomogeneous electron gas," *Phys. Rev.*, vol. 137, pp. A1441–A1443, Mar 1965. [Online]. Available: https://link.aps.org/doi/10.1103/PhysRev.137.A1441

[18] R. Gross and A. Marx, *Festkörperphysik*. De Gruyter, 2018. [Online]. Available: https://doi.org/10.1515/9783110559187

[19] W. Voigt, *Lehrbuch der Kristallphysik*. B.G. Teubner, 1910.

[20] M. Born, "On the stability of crystal lattices. i," *Mathematical Proceedings of the Cambridge Philosophical Society*, vol. 36, no. 2, p. 160–172, 1940.

[21] F. Mouhat and F. m. c.-X. Coudert, "Necessary and sufficient elastic stability conditions in various crystal systems," *Phys. Rev. B*, vol. 90, p. 224104, Dec 2014. [Online]. Available: https://link.aps.org/doi/10.1103/PhysRevB.90.224104

[22] P. T. Jochym, "Module for calculating elastic tensor of crystals." [Online]. Available: https://github.com/jochym/Elastic/

[23] P. T. Jochym, K. Parlinski, and M. Sternik, "Tic lattice dynamics from ab initio calculations," *The European Physical Journal B - Condensed Matter and Complex Systems*, vol. 10, 1999. [Online]. Available: https://doi.org/10.1007/s100510050823

[24] P. T. Jochym and K. Parlinski, "Ab initio lattice dynamics and elastic constants of zrc," *The European Physical Journal B - Condensed Matter and Complex Systems*, vol. 15, 2000. [Online]. Available: https://doi.org/10.1007/s100510051124

[25] G. Czycholl, *Theoretische Festkörperphysik: Von Den Klassischen Modellen Zu Modernen Forschungsthemen*, ser. Physics and astronomy online library. Springer, 2004. [Online]. Available: https://books.google.de/books?id=P0XOwAEACAAJ

[26] Y. Hinuma, G. Pizzi, Y. Kumagai, F. Oba, and I. Tanaka, "Band structure diagram paths based on crystallography," *Computational Materials Science*, vol. 128, pp. 140–184, 2017. [Online]. Available: https://www.sciencedirect.com/science/article/pii/S0927025616305110

[27] A. Togo and I. Tanaka, "`Spglib`: a software library for crystal symmetry search," 2018.

[28] W. P. Davey, "Precision measurements of the lattice constants of twelve common metals," *Phys. Rev.*, vol. 25, pp. 753–761, Jun 1925. [Online]. Available: https://link.aps.org/doi/10.1103/PhysRev.25.753

[29] G.-X. Zhang, A. M. Reilly, A. Tkatchenko, and M. Scheffler, "Performance of various density-functional approximations for cohesive properties of 64 bulk solids," *New Journal of Physics*, vol. 20, no. 6, p. 063020, jun 2018. [Online]. Available: https://dx.doi.org/10.1088/1367-2630/aac7f0

[30] C. Kittel, *Introduction to Solid State Physics*, 8th ed. Wiley, 2004.

[31] J. Vallin, M. Mongy, K. Salama, and O. Beckman, "Elastic constants of aluminum," *Journal of Applied Physics*, vol. 35, no. 6, pp. 1825–1826, 1964. [Online]. Available: https://doi.org/10.1063/1.1713749

[32] D. Waldorf, "Temperature and composition dependence of the elastic constants of dilute alloys of manganese in copper," *Journal of Physics and Chemistry of Solids*, vol. 16, no. 1, pp. 90–99, 1960. [Online]. Available: https://www.sciencedirect.com/science/article/pii/0022369760900779

[33] Y. Chen, Z. Zhang, Z. Chen, A. Tsalanidis, M. Weyland, S. Findlay, L. J. Allen, J. Li, N. V. Medhekar, and L. Bourgeois, "The enhanced theta-prime (θ') precipitation in an al-cu alloy with trace au additions," *Acta Materialia*, vol. 125, pp. 340–350, 2017. [Online]. Available: https://www.sciencedirect.com/science/article/pii/S135964541630948X

[34] F. Apostol and Y. Mishin, "Interatomic potential for the al-cu system," *Phys. Rev. B*, vol. 83, p. 054116, Feb 2011. [Online]. Available: https://link.aps.org/doi/10.1103/PhysRevB.83.054116

[35] V. Ozolins and C. Wolverton, "Entropically favored ordering: The metallurgy of al2cu revisited," *Physical Review Letters*, vol. 86, 06 2001.

[36] N. Ta, M. U. Bilal, I. Häusler, A. Saxena, Y.-Y. Lin, F. Schleifer, M. Fleck, U. Glatzel, B. Skrotzki, and R. Darvishi Kamachali, "Simulation of the θ' precipitation process with interfacial anisotropy effects in al-cu alloys," *Materials*, vol. 14, no. 5, p. 1280, Mar 2021. [Online]. Available: http://dx.doi.org/10.3390/ma14051280

[37] J. Van Vechten, R. Tsu, and F. Saris, "Nonthermal pulsed laser annealing of si; plasma annealing," *Physics Letters A*, vol. 74, no. 6, pp. 422–426, 1979. [Online]. Available: https://www.sciencedirect.com/science/article/pii/0375960179902421

[38] V. Recoules, J. Clérouin, G. Zérah, P. M. Anglade, and S. Mazevet, "Effect of intense laser irradiation on the lattice stability of semiconductors and metals," *Phys. Rev. Lett.*, vol. 96, p. 055503, Feb 2006. [Online]. Available: https://link.aps.org/doi/10.1103/PhysRevLett.96.055503

[39] S. Khakshouri, D. Alfè, and D. Duffy, "Development of an electron-temperature-dependent interatomic potential for molecular dynamics simulation of tungsten under electronic excitation," *Physical review. B, Condensed matter*, vol. 82, 12 2008.

[40] N. Medvedev, Z. Li, and B. Ziaja, "Thermal and nonthermal melting of silicon under femtosecond x-ray irradiation," *Phys. Rev. B*, vol. 91, p. 054113, Feb 2015. [Online]. Available: https://link.aps.org/doi/10.1103/PhysRevB.91.054113

[41] P. L. Silvestrelli, A. Alavi, M. Parrinello, and D. Frenkel, "Ab initio molecular dynamics simulation of laser melting of silicon," *Phys. Rev. Lett.*, vol. 77, pp. 3149–3152, Oct 1996. [Online]. Available: https://link.aps.org/doi/10.1103/PhysRevLett.77.3149

[42] T. Nagao, Y. Iizuka, T. Shimazaki, and C. Oshima, "Surface phonons of na-induced superstructures on al(111)," *Phys. Rev. B*, vol. 55, pp. 10 064–10 073, Apr 1997. [Online]. Available: https://link.aps.org/doi/10.1103/PhysRevB.55.10064

[43] R. M. Nicklow, G. Gilat, H. G. Smith, L. J. Raubenheimer, and M. K. Wilkinson, "Phonon frequencies in copper at 49 and 298°k," *Phys. Rev.*, vol. 164, pp. 922–928, Dec 1967. [Online]. Available: https://link.aps.org/doi/10.1103/PhysRev.164.922

[44] R. Ernstorfer, M. Harb, C. T. Hebeisen, G. Sciaini, T. Dartigalongue, and R. J. D. Miller, "The formation of warm dense matter: Experimental evidence for electronic bond hardening in gold," *Science*, vol. 323, no. 5917, pp. 1033–1037, 2009. [Online]. Available: https://www.science.org/doi/abs/10.1126/science.1162697

[45] Z. Lin, L. V. Zhigilei, and V. Celli, "Electron-phonon coupling and electron heat capacity of metals under conditions of strong electron-phonon nonequilibrium," *Phys. Rev. B*, vol. 77, p. 075133, Feb 2008. [Online]. Available: https://link.aps.org/doi/10.1103/PhysRevB.77.075133

[46] W. Ritz, "Über eine neue methode zur lösung gewisser variationsprobleme der mathematischen physik." vol. 1909, no. 135, pp. 1–61, 1909. [Online]. Available: https://doi.org/10.1515/crll.1909.135.1

[47] A. Sommerfeld, "Zur elektronentheorie der metalle auf grund der fermischen statistik," *Zeitschrift für Physik*, 1928. [Online]. Available: https://doi.org/10.1007/BF01391052

[48] A. Sommerfeld and H. Bethe, *Elektronentheorie der Metalle*, ser. Heidelberger Taschenbücher. Springer Berlin Heidelberg, 1967. [Online]. Available: https://books.google.de/books?id=EJ8MAQAAIAAJ

[49] M. Weinert and J. W. Davenport, "Fractional occupations and density-functional energies and forces," *Phys. Rev. B*, vol. 45, pp. 13 709–13 712, Jun 1992. [Online]. Available: https://link.aps.org/doi/10.1103/PhysRevB.45.13709

[50] G. Kresse and J. Furthmüller, "Efficiency of ab-initio total energy calculations for metals and semiconductors using a plane-wave basis set," *Computational Materials Science*, vol. 6, no. 1, pp. 15–50, 1996. [Online]. Available: https://www.sciencedirect.com/science/article/pii/0927025696000080

Ausführliche Zusammenfassung in deutscher Sprache

Neue Fertigungstechniken wie die additive Fertigung und insbesondere das 3D-Laserdrucken gehören zu den neuesten Trends, die die Herstellung von Bauteilen in geringen Stückzahlen wesentlich günstiger machen als die subtraktiven Techniken wie das Schneiden, Bohren oder Schleifen. Gleichzeitig erlauben diese Methoden wesentlich komplexere Konstruktionen als die konventionelle Fertigungstechniken. All das scheint lohnenswert für den Flugzeugbau, in dem Aluminium-basierte Legierungen üblich sind. Besonders Aluminium-basierte Legierungen mit geringem Kupferanteil werden bereits seit annähernd einhundert Jahren eingesetzt, möglicherweise die prominenteste ist *Duralumin*. Die Verwendung von Legierungen hat aufgrund der feineren Abstimmung von Härte, Wärmeleitfähigkeit oder Korrosionsbeständigkeit klare Vorteile gegenüber reinen Metallen. Nicht nur die Fertigung von Bauteilen aus Legierungen mit 3D-Laserdruck ist eine verheißungsvolle Methode, auch das Verzögern von Ermüdungserscheinungen in den Bauteilen kann die Lebensdauer der Bauteile wesentlich verlängern.
Um diese Techniken weiterzuentwickeln, müssen wir unser Wissen über das Verhalten von Metallen und deren Legierungen unter Lasereinwirkung erweitern. Computersimulationen erlauben hier Einblicke in die Eigenschaften der Materialien und deren Dynamik, wohingegen rein analytische Modelle nur für einfache und idealisierte Systeme anwendbar sind. Für diese Arbeit wählen wir deshalb die Dichtefunktionaltheorie, da sie uns Einblicke in die quantenmechanischen Prozesse erlaubt und die Ergebnisse dieser Methode in Molekulardynamik-Simulationen verwendet werden können, mit denen Zeit- und Größenskalen erreicht werden können, die mit Experimenten vergleichbar sind. Bisher gab es wenige solcher Untersuchungen, die sich aber zumeist auf Halbleiter, besonders Silizium, konzentrierten. Daher möchten wir mit dieser Arbeit unser Verständnis von durch Laser angeregte Materialien auf Metalle und deren Legierungen erweitern und sie mit dem Halbleiter Silizium vergleichen.

Wir beginnen mit einer theoretischen Einführung in die Dichtefunktionaltheorie und deren Erweiterungen auf nahezu jegliche, auch angeregte, Materialien. Anschließend werden wir die Eigenschaften diskutieren, mit denen wir Festkörper auch im angeregten Zustand charakterisieren können. Weiter beschreiben wir, wie unsere Rechnungen durchgeführt werden und wie Rechenzeit effektiv und effizient verwendet werden kann und suchen nach

angemessenen Parametern, mit denen unsere Rechnungen zuverlässige Daten produzieren. Wir bestätigen unsere Methoden, indem wir durch Experimente oder vergleichbare Rechnungen anderer Gruppen bekannte Größen wie die Gitterstruktur, sowie die elastischen Konstanten, Phononenspektren und Zustandsdichten der Materialien im Grundzustand berechnen und fanden dabei eine exzellente Übereinstimmung.
Wir bestimmen im nächsten Schritt die äquilibrierten Strukturen bei unterschiedlichen Anregungsgraden, beziehungsweise Elektronentemperaturen und finden, dass sich sowohl die Metalle, deren Legierungen, als auch Silizium ausdehnen, da der Entartungsdruck der Elektronen in der Grundzustandsstruktur steigt. Im Kontext der ultraschnellen Prozesse bei der Laserbearbeitung von Werkstoffen konzentrieren wir uns weiter auf die Grundzustandsstruktur und berechnen die elastischen Konstanten bei unterschiedlichen Elektronentemperaturen. Es zeigt sich, dass die elastischen Konstanten von Aluminium nahezu unverändert bleiben, in Silizium steigen und in Silizium sinken. Dies lässt auf eine nahezu unveränderte Gitterstabilität in Aluminium, eine erhöhte Stabilität in Kupfer und eine verminderte Stabilität in Silizium schließen. Die elastischen Konstanten der Al-Cu-Legierungen verhalten sich nicht monoton und machen eine klare Aussage über die Gitterstabilität, die nur auf den elastischen Konstanten basiert, unmöglich.
Als weiterer Test der Stabilität berechnen wir die Phononenspektren und finden ein ähnliches Bild wie in den elastischen Konstanten. Nach einer anfänglichen leichten Abnahme der Stabilität steigt diese in Aluminium, wohingegen die Stabilität in Kupfer monoton steigt und in Silizium monoton sinkt. Erstmals können wir demonstrieren, dass die Stabilität der Al-Cu-Legierungen mit dem Anregungsgrad steigt.

Ehrenwörtliche Erklärung

Gemäß §24 Absatz 7 der Prüfungsordnung vom 31. Juli 2015 versichere ich, dass ich diese Arbeit selbstständig verfasst habe, dass ich keine anderen als die angegebenen Quellen verwendet habe und alle wörtlich oder sinngemäß aus anderen Werken übernommenen Aussagen als solche gekennzeichnet habe, dass die eingereichte Arbeit weder vollständig noch in Teilen Gegenstand eines anderen Prüfungsverfahrens gewesen ist, dass ich diese Arbeit weder vollständig noch in Teilen bereits veröffentlicht habe und dass der Inhalt des elektronischen Exemplars mit dem des Druckexemplars übereinstimmt.

Ebersbach, den 19. Juli 2023 Simon Kümmel